One-dimensional Differential Newtonian Analysis for Applications in Saliva Rheology

by

Louise Lu McCarroll

A dissertation submitted in partial fulfillment
of the requirements for the degree of
Doctor of Philosophy
(Mechanical Engineering)
in The University of Michigan
2017

Doctoral Committee:

Professor William W Schultz, Co-Chair
Professor Michael J Solomon, Co-Chair
Professor Joseph Bull
Dr. Joseph T Murray, Veterans Affairs Hospital
Professor Alan S Wineman

Louise Lu McCarroll

lulz@umich.edu

ORCID iD: 0000-0003-1471-0655

For my parents, Yin and Lin Lin

ACKNOWLEDGEMENTS

I think the best phrase that describes this experience for me is "it takes a village" or in my case it should be "it takes a whole metropolitan area and then some." But I'll stick with the "village" analogy for now.

The chief villagers I'd like to thank are my advisors, Professor William Schultz and Professor Michael Solomon, for their seemingly unlimited supply of patience with me, especially when I was feeling like the village idiot. Thank you for your guidance these past few years, for teaching me to be resourceful, to a construct logical argument and perform novel analyses, for propping me up when my spirits were low, and last but not least, for being so approachable. I have really enjoyed working on this project with you both. Bill - I am still trying to learn how to "embrace chaos." Mike - I appreciate all the structure you have imposed on this process.

I'd also like to extend my gratitude to my committee members, Professor Alan Wineman, Professor Joseph Bull, and Dr. Joseph Murray, for helping me put bounds on this project. It is likely that without the advice of my committee I would have continued to run simulations and agonize over my data instead of writing. I am also grateful for all the time and guidance you have given me and even lab space when it was needed.

I'd also like to thank Professor David Dowling for always being an extra mentor and a cheerleader for me. I have really appreciated all the academic and professional advice he has given me.

Of course I can't forget my wonderful co-hort in the Autolab, at the NCRC, in

the Biotransport Lab, and now scattered all over the world. I wish I could list all the individual names but truth be told, I'd probably just start crying. The friendships I have made during this process have made the last few years of grad school so enjoyable. I looked forward to making the trek to school everyday because of these friendships.

Last but certainly not least, I must thank my family. I am grateful to my parents, Yin and Lin Lin, for encouraging me to study engineering. My parents, especially my dad, taught me what it means to persevere - an indispensible quality that I needed for this work. I also must thank my wonderfully supportive husband, Kellen. I'm not sure how he has managed the seemingly Herculean effort of starting a new job in Pittsburgh, driving back and forth to Ann Arbor to pack and move us out of our house, and looking for a new place for us to live all by himself. But I am grateful that he has taken over all the household duties to let me burrow into a hole and concentrate on writing. I am looking forward to starting in a new place with him and our son (dog), Boston.

TABLE OF CONTENTS

LIST OF FIGURES

Figure

LIST OF APPENDICES

Appendix

ABSTRACT

One-dimensional Differential Newtonian Analysis for Applications in Saliva Rheology

by

Louise Lu McCarroll

Co-Chairs: William W Schultz and Michael J Solomon

Oral and systemic health starts with healthy saliva. Saliva's functionality is affected by its rheology. Thus, alterations in saliva rheology may cause or indicate unhealthy biological function. "Sticky saliva", a subjective pathological description used by health professionals to indicate abnormal saliva mechanics, is linked to oral health issues, like cavities and xerostomia, and may indicate systemic health conditions, such as multiple sclerosis and HIV. Therefore, quantifying saliva's "stickiness" or its non-Newtonian behavior with physical science based metrics (i.e. viscosity, surface tension, elasticity) is critical for understanding the relationship between its mechanics and health outcomes.

Elongational flow is the main kinematic feature that distinguishes the coupling between the oral cavity and saliva mechanics. Therefore, our effort to quantify saliva stickiness pays special attention to its response to elongation. Capillary break-up rheometry (CBR) is a common technique for characterizing extensional flow properties. CBR is ideal for quantifying low-viscosity fluids, like saliva, because it does not require a force measurement. Instead, extensional flow properties are determined by

monitoring the resulting midfilament evolution after an approximate axial step-strain is imposed on a fluid sample. The standard CBR analysis requires several approximations and corrections to maintain a purely kinematic approach. We have re-examined CBR foundations with a differential 1D Newtonian model to eliminate the large correction factors required when only measuring the midfilament thinning rate. Our analysis indicates filament free surface curvature gradients are the key measurement quantities required to accurately determine extensional properties when axial force is not measured. Thus, we present the development of a 1D differential Newtonian analysis that requires measurements of the fluid filament curvature and its gradients to determine the surface tension to viscosity ratio α. We evaluate the performance of our 1D differential analysis with experimental CBR data and numerical data generated by a 1D Newtonian model.

We also explore methods to expand the measurement capabilities of current CBR set-ups with the 1D differential analysis. We simulate viscoelastic filament dynamics with a 1D Oldroyd-B model and evaluate the performance of the 1D differential method during the early viscous phase. We begin with the traditional but unrealistic CBR assumptions of long, unstable filaments with zero initial polymer stresses at the end of stretch (start of CBR measurement). The results suggest the 1D differential approach coupled with the standard viscoelastic CBR analysis can facilitate measurements of multiple rheological parameters from a single sample.

Finally, we investigate the performance of the 1D differential analysis during the stretching process. We first model the filament evolution during the axial step-strain to demonstrate the stretch history must be considered in the CBR analysis for viscoelastic fluids. We also model a stretch history that avoids filament break-up to extend the lower limit of the standard CBR method's viscosity range.

CHAPTER I

Introduction

1.1 Introduction and Motivation

Oral and systemic health start with healthy saliva. It is important for maintaining pH, antibacterial activity, and dentition, lubricating the hard and soft oral tissues, healing, tasting, chewing, and swallowing. The effectiveness of these functions is affected by saliva's rheological properties, such as viscosity, elasticity, and surface tension (Kaplan & Baum 1993; Christersson *et al.* 2000; Stokes & Davies 2007; Zussman *et al.* 2007; Carpenter 2012; Kazakov *et al.* 2009). For example, saliva viscosity affects lubrication between hard and soft surfaces in the oral cavity and can affect the tasting, chewing, and swallowing processes. Saliva also exhibits shear-thinning (decrease in viscosity with increasing strain-rate), enabling proper flow and cleansing action in the oral cavity. Furthermore, salivary elasticity helps form a protective layer on enamel to prevent acid attacks after food and beverage consumption (Carpenter 2013; Preetha & Banerjee 2005). Therefore, alterations in saliva rheology may indicate or cause unhealthy biological function (Haward *et al.* 2011).

"Sticky saliva" is a term used by health professionals to indicate abnormal saliva mechanics. It is linked to many oral health issues including dental carries, oral lesions and infections, gingivitis, dysphagia, aspiration pneumonia, weight loss, and speech difficulties (Akkas *et al.* 2013; Garcia *et al.* 2013; Van Tornout *et al.* 2013; Smith *et al.*

2013; Ogama & Ogama 2013; Mittal *et al.* 2013). Oral health is intimately linked to systemic health and thus sticky saliva is problematic among the malnourished, head and neck cancer patients who have received radiation therapy, medicine-induced xerostomia patients, and those with multiple sclerosis, Myasthenia Gravis, HIV and Parkinson's disease (Langmore *et al.* 1998; Terpenning *et al.* 2001). Saliva substitutes are available to alleviate the discomfort of those with salivary dysfunctions but are unsatisfactory because of their limited duration and unnatural feel. These issues may be addressed by better matching the physical properties of these products to those of healthy saliva (Levine *et al.* 1987).

Saliva's rheological behavior is determined by its constituents and may be useful for non-invasive health diagnostics. Although saliva is more than 99% water, its protein and ion content ($\sim$0.3%) gives rise to its non-Newtonian behavior (Carpenter 2013; Proctor *et al.* 2005). The protein content is comprised of high molecular weight mucins, various enzymes, antibodies, antibacterial proteins, proline-rich proteins, and peptides (Sarkar *et al.* 2009; Humphrey & Williamson 2001). Many of these proteins are biomarkers for oral and systemic diseases (Lima *et al.* 2010; Liu & Duan 2012). The presence of specific proteins may be reflected in saliva's rheological response. For instance, Zussman *et al.* (2007) characterizes the viscoelastic behavior of saliva samples from the three major salivary glands with measurements of polymer relaxation time λ in extension. The polymer relaxation time represents the delay in a non-Newtonian fluid's response to motion and is a common measure of viscoelasticity. In the context of saliva, λ may be considered a measure of "stickiness." Zussman *et al.* (2007) reports that mucin-rich salivas from the sublingual and submandibular glands have larger relaxation times (indicating stronger viscoelasticity or "stickiness") than mucin-free saliva from the parotid gland. Therefore, saliva rheology may be a useful tool for detecting the presence of specific proteins (or biomarkers) associated with pathological function.

The main kinematic feature that distinguishes the coupling between the oral cavity and saliva mechanics is its response in elongational flow, particularly for mastication and breaking down food materials (de Bruijne *et al.* 1993). There are indications that saliva in shear (as between two grinding molars) is an effective lubricant (Bongaerts *et al.* 2007) but this likely involves interaction with biofilms (such as plaque) that is beyond the scope of this work. In fact, saliva in standard shear rheometry behaves similarly to water (figure 1.1). This is unsurprising since saliva is mostly water. However, saliva in extension evolves into a beads-on-a-string (BOAS) morphology (figure 1.2) and has a filament lifetime that is uncharacteristic of a low-viscosity Newtonian fluid (Bhat *et al.* 2010). In particular the viscoelastic bulk flow behavior is attributed to MUC 5B, a gel-forming mucin considered the primary biopolymer in saliva based on its high molecular weight (2-40 MDa) and relatively high concentration ($\sim$30-500 μg/mL in whole human saliva) (Sarkar *et al.* 2009; Haward *et al.* 2011; Schipper *et al.* 2007).

Saliva rheology has been widely characterized in shear as shown by an extensive list in table 1 of Foglio-Bonda *et al.* (2014). However, only a few studies have investigated saliva in extension. Zussman *et al.* (2007) investigated variations in λ of saliva samples from a group of young adults ($\sim$20 years-old) and elderly individuals ($\sim$75 years old) to understand the underlying causes for age-related differences in oral health issues observed between the two age groups. Wagner (2015) measured the temporal change in λ to explain why saliva samples (stored at room temperature) become watery with increasing time since the sampling. Turcanu *et al.* (2015) measured λ for saliva samples produced by mechanical and acidic simulation, a study analogous to the work presented by Stokes & Davies (2007) for saliva shear rheometry. Unlike the other extensional saliva studies, Haward *et al.* (2011) observed the extensional viscosity of centrifuged saliva samples from two healthy individuals grew rapidly with increasing strain-rate but decreased after reaching a maximum at 1200 s^{-1}. Haward *et al.*

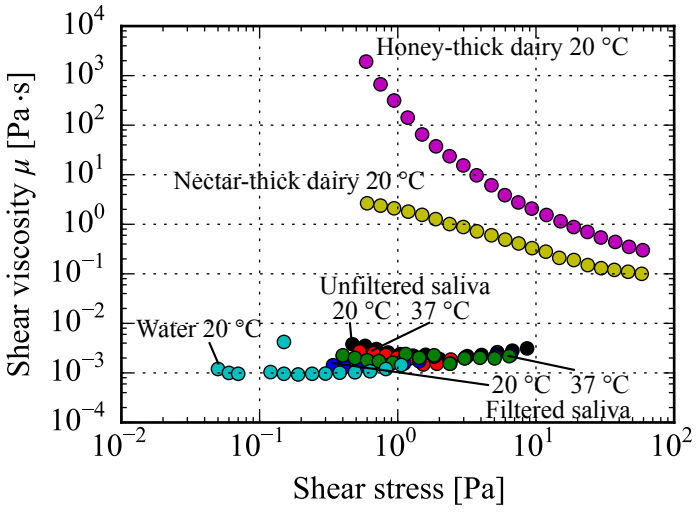

Figure 1.1: Measurements of shear viscosity μ plotted with shear stress for water at 20°C, filtered and unfiltered salivas at 20°C and 37°C (body temperature), and two thickened products commercially available for dysphagia patients also at 20°C. Measurements were performed in a cone-and-plate rheometer. Viscosities of water and saliva are very similar.

(2011) listed inertial effects and breakages in the inter-mucin bonds or mucin chains as potential causes for the sudden drop in the extensional viscosity for strain-rates larger than 1200 s^{-1}. Although these studies have added to the scarce literature on saliva extensional rheology, generally only one extensional flow parameter is quantified in each investigation. However, saliva functionality is linked to multiple rheological properties and thus it is desirable to develop a technique capable of multiple parameter characterizations.

1.2 Extensional Flow Kinematics

Ideally, extensional flow properties should be characterized from pure extensional flows. The defining characteristic of pure extensional (shear-free) flow kinematics is the diagonal velocity gradient tensor $v_{i,j}$ resulting in a diagonal strain-rate tensor $\dot{\gamma}_{ij} = \frac{1}{2}(v_{i,j}+v_{j,i})$, a diagonal extra stress tensor τ_{ij}, and zero vorticity $\omega_{ij} = \frac{1}{2}(v_{j,i}-v_{i,j}) = 0$. Additionally, pure elongational flows are spatially homogeneous when $v_{i,j}$ is only

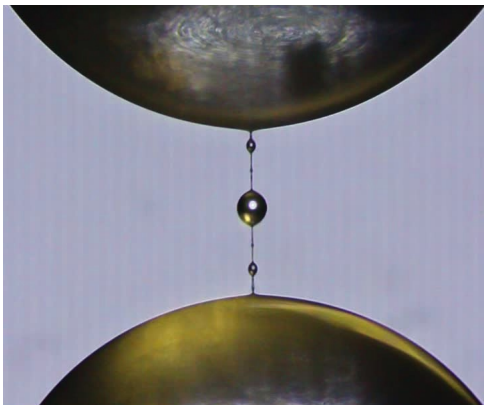

Figure 1.2: An elongated saliva filament after an imposed axial step-strain in a capillary break-up rheometry experiment forms a thin filament with beads-on-a-string.

dependent on time, as in general cases of uniaxial and biaxial stretching, and thus $\dot{\gamma}_{ij}$ and τ_{ij} are also independent of spatial position (Petrie 1979).

1.3 Extensional Rheometry for Low-Viscosity Fluids

Pure extensional flows are difficult to generate, particularly for low-viscosity fluids. However, saliva in extension has been characterized by at least two techniques (Haward *et al.* 2011; Zussman *et al.* 2007; Wagner 2015; Turcanu *et al.* 2015) described in the following sections.

1.3.1 Extensional flow oscillatory rheometer

Haward *et al.* (2011) performed investigations on saliva extensional viscosity using a modified extensional flow oscillatory rheometer EFOR, an opto-microfluidic cross-slot device that creates a strong planar flow with a stagnation point. The device consists of two pairs of opposing channels (each 200 μm wide and 1.2 cm long) all in the same plane. A schematic is shown in figure 1.3. The strain and strain-rate of the flow is controlled by the micro-pumps located at the end of each channel. Pressure transducers are also located at an inlet and outlet of the flow to determine

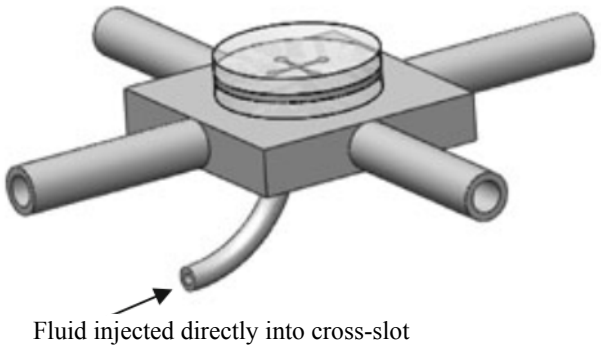

Figure 1.3: Schematic of the extensional flow oscillatory rheometer (EFOR) (Haward *et al.* 2011), a micro-fluidic cross-slot device that generates planar extensional flow to characterize extensional flow properties.

measurements of the apparent extensional viscosity. The stagnation point is produced when the fluid pumped into one pair of opposing channels collides and is pumped out of the other two opposing channels. Although the flow velocity is zero at the stagnation point, the strain-rate is finite and may be large.

One advantage of the EFOR is the ability to impose various deformation histories on the flow, such as oscillatory motion or constant flow rate, by programming the micro-pumps. Additionally, this technique is advantageous for trapping macromolecules at the stagnation point where they can accumulate strain. However, the small size of the EFOR device limits the range of imposed strain-rates, measurable pressure drop, and inertial effects it can resolve. Furthermore, a small amount of shear is introduced into the planar extensional flow especially near the boundaries (Galindo-Rosales *et al.* 2013).

1.3.2 Capillary break-up rheometry

The majority of extensional saliva studies (Zussman *et al.* 2007; Wagner 2015; Turcanu *et al.* 2015) are performed in capillary break-up rheometry (CBR) device, known commercially as the Capillary Breakup Extensional Rheometer (CaBER$^{\text{TM}}$). A CBR device is a type of filament stretching device that imposes an approximate ax-

ial step-strain on a fluid sample. Following the cessation of the imposed deformation, the time evolution of the filament's minimum radius due to capillarity is monitored to determine extensional flow properties. Unlike other filament stretching devices such as the filament stretching extensional rheometer (FiSER^{TM}), imposing a known deformation profile is not necessary in a CBR experiment. Additionally, the tensile force in the filament is not required to determine extensional properties in CBR. This is a particularly advantageous feature for characterizing low-viscosity fluids where small forces are difficult to measure accurately (McKinley & Tripathi 2000; McKinley & Sridhar 2002; Galindo-Rosales *et al.* 2013).

CBR is ideal for investigating saliva rheology. One advantage is that CBR measurements are performed in a two-phase (saliva-air) environment. The oral cavity also contains saliva and air, although air may be in the form of trapped bubbles. Additional phases are also often present, such as a food bolus mixed with and coated in saliva (Brasseur 1987). CBR is also ideal for studying small samples. The measurement volumes of 3 - 150 μL accommodated by our CBR devices (described in chapter II and appendix B) are easily produced by healthly individuals and those with salivary dysfunction (Carpenter 2012). The ability to measure small samples ($< 10\mu$L) is also advantageous for characterizing saliva from specific glands or other oral sampling locations.

A CBR device consists of two parallel plates of radius R_p initially separated by a small gap L_0. The fluid sample is constrained between the plates and forms a squat cylinder with an initial aspect ratio $\Lambda_0 = L_0/R_p < 1$. A nearly uniaxial step-strain is typically imposed on the filament as the plates are rapidly moved apart and come to rest at a final separation length L_f that exceeds the Plateau stability limit (Plateau 1863). The standard CBR measurement begins at the cessation of the stretching pocess. The stretched filament begins to evolve due to capillary, viscous, inertial, elastic, and gravitational forces and the flow far away from the plates is

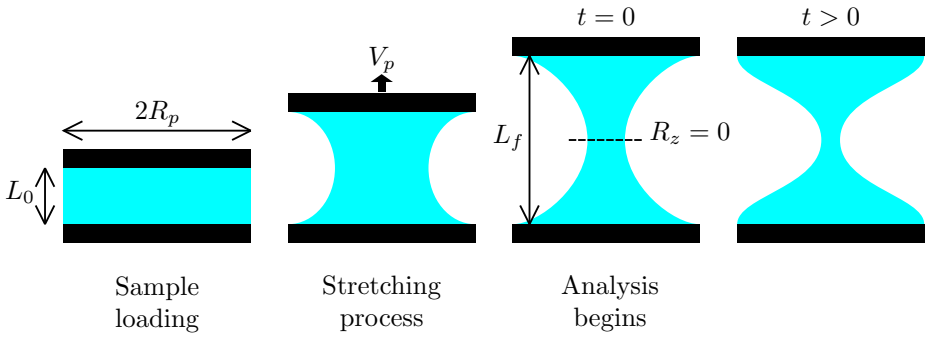

Figure 1.4: Schematic of a capillary break-up rheometry (CBR) device. A small fluid sample is initially constrained between two plates separated by a small gap L_0. The plates are rapidly separated to a final separation length L_f to impose a near uniaxial step-strain. The midfilament evolution is then monitored after the stretching process ceases to determine the extensional properties of the fluid filament.

one-dimensional (1D) and nearly pure extensional flow (Galindo-Rosales *et al.* 2013). The filament's midpoint evolution after the cessation of stretching is monitored by a camera or a laser micrometer. A schematic of a CBR experiment is shown in figure 1.4.

Rodd *et al.* (2005) shows the operating range of CBR is currently limited to characterizing viscosities and polymer relaxation times greater than 70 mPa·s and 1 ms, respectively. These limitations are primarily due to the small but finite time required to move the plates apart for the imposed deformation. In particular, the fluid filament ruptures before the start of the CBR measurement regime if the viscous time scale of a fluid sample is smaller than the time required to impose the deformation history. Thus we consider deformation histories that avoid filament break-up (chapter IV) to expand the measurement regime of traditional CBR.

The CBR analyses are originally developed for Newtonian and non-Newtonian fluids described by the Oldroyd-B constitutive theory (Bazilevsky *et al.* 1990; McKinley & Tripathi 2000). The standard CBR analysis is based on a 1D force balance applied at the filament "waist" where the filament radius R is at its minimum ($R_z = 0$). The analysis neglects gravity and inertia and therefore the axial force F throughout the

filment is constant. The uniform axial force at the filament waist is

$$F = (-p + \tau^{zz})R^2 + 2\pi\sigma R, \text{ where } R_z = 0 \tag{1.1}$$

where p is the pressure, τ^{zz} is the axial component of the extra deviatoric stress, σ is the surface tension coefficient, and R is the filament free surface profile. Although the pressure is unknown, it can be eliminated from (1.1) by the normal free surface boundary condition, $-p + \tau^{rr} = -\sigma\kappa$, to give

$$F = (-\sigma\kappa + \tau^{zz} - \tau^{rr})R^2 + 2\pi\sigma R, \text{ where } R_z = 0, \tag{1.2}$$

where τ^{rr} is the radial component of the extra deviatoric stress and κ is twice the mean curvature of the filament free surface.

For a Newtonian fluid, the extra stress τ_{ij} is linearly related to the strain-rate tensor $\dot{\gamma}_{ij}$. However, for non-Newtonian fluids, the relationship between τ_{ij} and $\dot{\gamma}_{ij}$ is more complicated. As discussed in chapter III, viscoelastic constitutive theories often represent the extra stress as a sum of a Newtonian solvent stress τ^s_{ij} and the polymer stress τ^p_{ij}. Thus a common expression for the non-Newtonian stress difference in (1.1) is $\tau^{zz} - \tau^{rr} = (\tau^{s,zz} - \tau^{s,rr}) + (\tau^{p,zz} - \tau^{p,rr})$.

Bazilevsky *et al.* (1990) makes several simplifying assumptions to develop a purely kinematic measurement from the local midfilament force balance (1.2). First, F is neglected because the filament is connected to quasistatic reservoirs attached to rigid end plates. Additionally, the curvature is approximated as $\kappa = 1/R$ or that of a cylinder. Finally, the second term in (1.1) representing the surface tension acting over the perimeter is not considered. After applying these simplifying assumptions, the original analysis by Bazilevsky *et al.* (1990) predict the midpoint decay rates R_t

for Newtonian and non-Newtonian filaments are

$$R_t = -\sigma/6\mu, \tag{1.3a}$$

$$R_t \sim \exp(-t/3\lambda). \tag{1.3b}$$

Therefore, the original CBR analysis (Bazilevsky *et al.* 1990) indicates material parameters such as μ, σ and λ, three properties related to saliva functionality, may be determined from measurements of the midfilament evolution after an imposed deformation.

Investigations on Newtonian fluids (Liang & Mackley 1994; Kolte & Szabo 1999) show (1.3a) underpredicts the midfilament decay and have therefore prompted re-examinations of the underlying assumptions regarding F and the missing surface tension perimeter term. Corrections to the original theory (1.3) have since been developed for Newtonian and non-Newtonian fluids (McKinley & Tripathi 2000; Clasen *et al.* 2006*a*). In particular, McKinley & Tripathi (2000) suggests an alternate approximation for F to maintain a purely kinematic approach and develops corrections based on similarity solutions for viscous and inviscid Newtonian flows (Papageorgiou 1995; Eggers 1993; Brenner *et al.* 1996). However, in chapter II we develop a kinematic approach based on the differential form of the governing equations for mass and momentum that does not require additional assumptions beyond 1D rectilinear flow. Thus, this work is focused on the development of a 1D differential analysis and evaluating its performance for characterizing Newtonian and non-Newtonian fluids.

We begin our examination of CBR foundations with a Newtonian model because it is the simplest constitutive theory and incorporates the effects of viscosity and surface tension. We then expand our analysis to non-Newtonian behavior to quantify saliva's viscoelastic nature. We model saliva's non-Newtonian behavior with an Oldroyd-B theory because it is the simplest viscoelastic theory for dilute polymer solutions that

predicts BOAS formation, a distinct feature of elongated saliva filaments (Bhat *et al.* 2010).

1.4 Scope of this work

In chapter II, we develop a 1D differential Newtonian analysis for CBR. Our local differential analysis does not require specific assumptions for the axial force to preclude its measurement. Our analysis indicates that measuring gradients in filament curvature is necessary to accurately determine fluid properties when axial force is not measured. We evaluate the performance of the 1D differential approach with experimental CBR data for viscous Newtonian silicone oils and numerical data generated by a 1D model for a viscous Newtonian filament and compare its performance with the standard integral method from literature.

In chapter III, we investigate surfactants and viscoelastic effects in filament dynamics to determine the applicability of our 1D differential approach for characterizing non-Newtonian filaments. We perform a simple experiment with a soap-and-water mixture to examine the role of surfactants in low-viscosity filament dynamics. We also study viscoelastic filament evolution with a 1D model and follow the typical development for CBR analyses which assumes a long, unstable filament with zero initial viscoelastic stresses. This assumption may not accurately represent the physical state of a non-Newtonian filament after an imposed deformation since viscoelastic fluids have memory. However, this assumption simplifies the 1D model and is still useful for investigating trends in viscoelastic filament dynamics and evaluating the performance of the 1D differential analysis.

In chapter IV, we study filament dynamics throughout the deformation process with a 1D model to evaluate the performance of the 1D differential analysis outside the traditional CBR measurement regime. We consider cases when zero initial viscoelastic stresses are an appropriate assumption, such as for the stable, cylindrical fluid sample

in a CBR experiment prior to the imposed stretch. We first model the approximate axial step-strain to demonstrate viscoelastic stresses become important before the start of the conventional CBR measurement regime. We also model the filament evolution driven by oscillating boundaries to investigate a deformation history that avoids filament break-up and facilitates measurements of low-viscosity filaments.

Finally, we summarize the state of the current work regarding the 1D differential analysis in chapter V and provide recommendations for its application. Additionally, we discuss future work to further expand the operating range and validate the performance of the 1D differential method.

In appendix A, we discuss the results of our probative saliva experiments. The purpose of these preliminary experiments is to inform the experimental design for a larger scale investigation on saliva.

Additional details about the experimental set-up and numerical methods for the work presented in chapters II - IV are given in appendices B and C.

CHAPTER II

One-dimensional Differential Newtonian Analysis

2.1 Introduction

Capillary break-up rheometry (CBR) is commonly applied to measure extensional flow properties. CBR provides a single-point, kinematic measurement of the extensional properties that applies to liquids that form a filament or bridge. The extensional properties are determined from the time evolution of the filament's minimum radius due to capillarity after imposing an approximate step-strain. CBR is simpler and less expensive than previous filament rheometers (Matta & Tytus 1990; Tirtaatmadja & Sridhar 1993; Spiegelberg *et al.* 1996) because it does not impose a known deformation profile on the filament nor does it require a force measurement. This latter feature is particularly useful for low-viscosity fluids where small forces are difficult to measure accurately.

The standard CBR analysis proceeds by a 1D force balance applied at the "waist" where the filament radius R is at its minimum ($R_z = 0$). The analysis neglects gravity and inertia. For a Newtonian filament, the uniform axial force F is balanced by the total normal stress on the cross-sectional surface and a surface tension term acting over the perimeter. The normal free surface boundary condition determines pressure and the force balance where $R_z = 0$ becomes

$$F = (-\sigma\kappa + 3\mu w_z)\pi R^2 + 2\pi R\sigma, \tag{2.1}$$

where σ is the surface tension coefficient, κ is twice the mean curvature of the free surface, w is the axial velocity, μ is the viscosity, R is the free surface radius, z is the axial location, t is time and subscripts with independent variables indicate partial differentiation. The viscous term in (2.1) is the Trouton viscosity for axisymmetric extensional flow. Equation (2.1) is combined with the continuity equation integrated over the filament cross-section,

$$(R^2)_t + (wR^2)_z = 0, \tag{2.2}$$

to determine the surface tension to viscosity ratio α

$$\alpha = \frac{\sigma}{6\mu} = \frac{-R_t/R - F/(6\mu\pi R^2)}{\kappa - 2/R}, \text{ where } R_z = 0. \tag{2.3}$$

Equation (2.3) is a local analysis that is exact in the 1D limit, but F is determined from a global analysis (Renardy 1994) or measured experimentally. However, F is difficult to measure for low-viscosity fluids. We review methods where F is approximated to obviate its measurement. Bazilevsky *et al.* (1990) neglects F because of large quasi-static reservoirs at the endplates and also approximates κ as $1/R$. Bazilevsky *et al.* (1990) also neglects the surface tension perimeter term, reducing (2.3) to $\alpha = -R_t$. This simple relationship significantly underpredicts α in investigations on Newtonian fluids (Liang & Mackley 1994; Kolte & Szabo 1999).

McKinley & Tripathi (2000) simplify (2.3) with two approximations to develop a simple single-point analysis without a force measurement. First, κ is approximated by $1/R$ because the filament becomes increasingly cylindrical near break-up ($R_z(z) \to 0$). Then, a limiting argument of $F(t) \to 2\pi\sigma R(t)$ as $R(t) \to 0$ is applied. A new dimensionless variable $X = F/2\pi\sigma R$ is introduced and replaces these terms in (2.1).

If X is a constant, these approximations reduce (2.3) to

$$\alpha = \frac{-R_t}{(2X-1)}, \text{ where } R_z = 0. \tag{2.4}$$

Introducing X removes the requirement for a force measurement. Values of X are determined from local analyses of global solutions describing the break-up of Newtonian filaments (Eggers 1993, 1997; Brenner *et al.* 1996; Papageorgiou 1995). The limiting argument implies X should approach unity as $R \to 0$. However, McKinley & Tripathi (2000) show that X varies with time and asymptotically approaches $X \approx 0.7127$. This is consistent with the value of X determined from a similarity solution for viscous filaments (Papageorgiou 1995).

This limiting argument of McKinley & Tripathi (2000) implies that the first term on the right-hand side in (2.1) vanishes faster than the second term as $R \to 0$. However, X does not approach unity because κ and the axial strain rate w_z are $\mathcal{O}(1/R)$, indicating all terms in (2.1) are $\mathcal{O}(R)$. The standard CBR method uses (2.4) to measure α. In the next section we present a differential approach to determine α that does not require approximations to eliminate F.

2.2 Differential Analysis

We derive a differential equation for α from the 1D governing equation (Eggers 1997)

$$(3\mu w_z R^2)_z - \sigma\kappa_z R^2 - \rho g R^2 = \rho R^2(w_t + w w_z), \tag{2.5}$$

where ρ is the fluid density and g is the gravitational acceleration. Twice the mean curvature κ of an axisymmetric free surface R is

$$\kappa = \frac{1}{R(1+R_z^2)^{1/2}} - \frac{R_{zz}}{(1+R_z^2)^{3/2}}. \tag{2.6}$$

A formal 1D analysis approximates κ as $1/R$ (Schultz & Davis 1982), but we model full curvature to be consistent with static filaments and more complex morphologies such as "beads-on-a-string" where higher-order axial curvature terms are important. The inclusion of the axial curvature also aids numerical stability (Eggers 1997).

Integrating (2.5) with respect to z yields (2.3) where F is the time-dependent constant of integration. Hence, methods that include F are integral approaches. Equation (2.5) is valid wherever extensional flow is rectilinear ($w_r = 0$, where r is the radial coordinate) whereas (2.3) is limited to the waist. Equation (2.5) indicates that the gradient of curvature drives the capillary flow. Without an axial change in the free surface curvature, the capillary pressure would not increase locally to drive the flow away from the filament waist. Therefore, resolving the filament free surface profile $R(z,t)$ is necessary to characterize extensional properties without measuring or inferring force.

A simple geometric analysis to determine α by measuring only $R(z,t)$ is desirable. As in previous studies, velocity measurements may be avoided if the problem is symmetric about the filament waist. Then R and w are even and odd functions of z, respectively, with the origin at the waist. Equations (2.2) and (2.5) maintain this symmetry only by ignoring gravity and by having symmetric boundary (and initial) conditions. The gradient of curvature, κ_z, for a symmetric filament is zero at the waist, however κ_{zz} is non-zero. Therefore, an additional z - derivative of the axial momentum equation is required to account for the gradient of curvature's role in the filament dynamics and results in κ_{zz}. An explicit expression for α is then determined after taking one z - derivative of (2.5), two z - derivatives of (2.2), and one t - derivative of (2.2) to give

$$\alpha = \frac{\sigma}{6\mu} = \frac{3R_tR_{zz} - RR_{zzt}}{\kappa_{zz}R^2} - \frac{1}{3\nu\kappa_{zz}R^2}(3R_t^2 - RR_{tt}), \text{ where } R_z = 0 \qquad (2.7)$$

and where ν is the kinematic viscosity. When inertial effects are small, the term with ν may be neglected. We show below that inertia is negligible for the results presented here.

Equation (2.7) indicates that R_{zz} and the necking rate R_t are needed to determine α without a force measurement. The presence of κ_{zz} in (2.7) also introduces R_{zzzz} through the second term in (2.6). The central role of the gradient of curvature (rather than the curvature itself) is a key development; it suggests that its measurement avoids the approximations and correction factors required to apply (2.3). However, this approach requires measurements of the local filament profile and its curvature gradients. Next, we conduct CBR experiments to demonstrate measurements of the required gradients of curvature and perform a numerical simulation of the filament evolution to compare methods (2.7) and (2.4).

2.3 Experimental Methods

We construct a CBR to determine α from the evolution of the fluid filament profile $R(z,t)$ after an imposed axial strain. These measurements evaluate and compare the performances of the differential formulation (2.7) and the standard integral method (2.4) for Newtonian fluids. The device consists of two parallel, circular plates of radius R_p initially separated by a distance L_0. The fluid sample volume is approximated by $\pi L_0 R_p^2$ and forms a squat cylinder constrained by the initial gap geometry. The top plate is held fixed while the bottom plate falls due to gravity until a final plate separation of L_f imposes an approximate step-strain. The bottom plate is attached to a stem with two collars to guide the vertical motion. The upper collar also acts as a stop for the moving assembly and may be adjusted to vary L_f and consequently the strain L_f/L_0.

Five Newtonian silicone oils (GE Momentive, Brookfield) with viscosities 0.35 Pa-s$<\mu<$10 Pa-s are tested at $R_p = 3$ mm, initial aspect ratio $\Lambda_0 = L_0/R_p = 0.733$, and

$L_f/L_0 = 3$. Viscosities and surface tension coefficients at 20°C are independently measured by a cone-and-plate rheometer (ARES - G2) and by a force balance technique (Padday *et al.* 1975) with a 12.7 mm diameter disk and a milligram balance (Ohaus AP310) to determine reference values. All silicone oils have similar densities and surface tension coefficients ranging between $\rho = 970$ and 990 kg/m^3 and $\sigma = 20$ and 20.4 mN/m, respectively. The properties (μ, ρ, σ) are measured three times for each silicone oil and reported errors are twice the standard deviation of the replications (0.02 to 0.6 Pa-s, 10 to 30 kg/m^3, and 0.3 to 0.8 mN/m, respectively). Measurements for μ, ρ, and σ are within 7% of the values reported by the manufacturers at 25°C.

The operating range of the differential analysis is further investigated by evaluating three sample volumes and three strains with a Newtonian silicone oil of $\mu =$ 1.0 Pa-s. The sample volumes are varied by $R_p = 2$, 3, and 4 mm while keeping $\Lambda_0 = 0.733$ and $L_f/L_0 = 3$. The three strains, $L_f/L_0 = 2$, 3 and 4.5, are achieved by varying L_f while keeping $\Lambda_0 = 0.733$ and $R_p = 3$ mm.

The evolving fluid filaments are backlit with a fiber optic lightsource and captured by a Phantom v210 high-speed camera (Vision Research, 1280 x 800 pixels) through a microscope objective to increase the spatial resolution, particularly in the radial direction. Increasing the magnification limits the field-of-view and consequently the entire free surface profile is not visible, especially before and during the stretching process. Frame rates vary from 40 fps for the most viscous silicone oil to 1000 fps for the least viscous oil. A 10x Nikon microscope objective (numerical aperture $NA =$ 0.30, magnification $M = 14$, 1.2 μm/pixel) aids $R_p = 2$ mm experiments while a 4x Nikon objective (NA =0.13, $M = 4.4$, 3.2 μm/pixel) is used for $R_p = 3$ mm and 4 mm experiments. The step-strain procedure is performed at least five times for each μ, R_p, and L_f/L_0 case.

2.4 Image and Data Analysis

Images of the filament evolution are analyzed in MATLAB to determine $R(z)$ at each time step. The time evolution of the filament is traced by an edge detection scheme (Canny 1986). The distance between the right and left edges of the free surface (indicated in white in figure 2.1a) defines the local value of $2R(z)$, relatively independent of the filament orientation with respect to the camera frame. The resolution of the edge detection scheme is one pixel and results in a piecewise constant description of the free surface as shown in the enlarged view in figure 2.1a. A polynomial least-squares fit in space is applied to describe the filament radius $R(z) = \sum_{n=0}^{N} R_n z^n$ at each time step. A 4th-order polynomial fit is the lowest order fit required to measure R_{zzzz} with a least-squares regression approach. We apply a 6th-order polynomial fit (N=6) because we consider a larger domain size to address limitations in the radial spatial resolution. The domain size for these experiments is 20% of the final separation length L_f. The domain avoids the reservoirs and is centered about the waist by requiring the lowest-order odd coefficient in the polynomial fit of $R(z)$ be 0. This constraint ensures the analysis is at a minimum (or maximum) of R. The coefficients of the higher-order odd terms are measures of filament asymmetry about the waist. A non-inertial coordinate system moves with $R_z = 0$ to achieve local symmetry after an asymmetric stretching process. The coordinate system acceleration is 10% or less of the gravitational acceleration g. We investigated the effect of a non-inertial coordinate system by performing an alternative experiment where the top plate is raised instead of dropping the bottom plate. The values of α determined by either (2.7) or (2.4) for either experimental alternative differ by less than 3%, indicating that the effects of inertia and a non-inertial coordinate are negligible. We also observed that the filament radius in both alternative experiments are larger near the bottom plate (as in figure 2.1a). If gravity were negligible, the filament would be fuller near the stationary plate due to inertia. Hence our observations show that gravity is the

main source of axial asymmetry. The local Bond number, $Bo(t) = 4\rho g R(0,t)^2/\sigma$, quantifies gravitational effects and decreases as the filament evolves toward break-up ($R(0,t) \to 0$). Gravitational effects are considered negligible when $Bo(t) < 0.1$ (McKinley & Tripathi 2000).

Time-varying spatial derivatives of R required for (2.7) are determined from derivatives of the polynomial least-squares fit. The least-squares approach suppresses noise due to spatial discretization of the imaged free surface profile as seen in figure 2.1a for a Newtonian silicone oil filament ($\mu = 1.0$ Pa-s) in a CBR experiment at $R_p = 3$ mm and $L_f/L_0 = 3$. However, the least-squares results for R, its spatial derivatives, and consequently κ_{zz} evaluated at the filament are still noisy as illustrated by the black curves for R_{zz} and κ_{zz} in figure 2.1b. A triangular center-weighted running average (typically 15 points) is applied to R and its derivatives to reduce temporal fluctuations introduced by the time series of least-squares fits in space (gray curves in figure 2.1b). The uncertainties in R, its spatial derivatives, and κ_{zz} are determined by propagating the standard error on the least-squares coefficients. Temporal derivatives, $R_t(t)$ and $R_{zzt}(t)$, are then determined from derivatives of a running least-squares fit in time also applied to 15 points from the triangular center-weighted results for $R(t)$ and $R_{zz}(t)$. As seen in figure 2.1c, a local temporal least-squares fit (gray curves) produces comparable but less noisy results than a central differencing scheme (black curves). The uncertainties in the time derivatives are determined from the standard error in the temporal least-squares coefficients. The spatial and temporal derivatives of R determine $\alpha(t)$ by the differential method (2.7) for each trial. Finally, five replicate trials are ensemble averaged for each experimental condition to determine $\bar{\alpha}(t)$ (figure 2.1d). We also determine values of $\alpha(t)$ by (2.4) with a time-varying necking rate $R_t(t)$, then average over five replicate trials to determine $\bar{\alpha}(t)$. The uncertainties in $\bar{\alpha}(t)$ are the standard error of five trials.

The uncertainties for all terms in (2.7) are monitored, particularly for $R_{zzzz}(t)$,

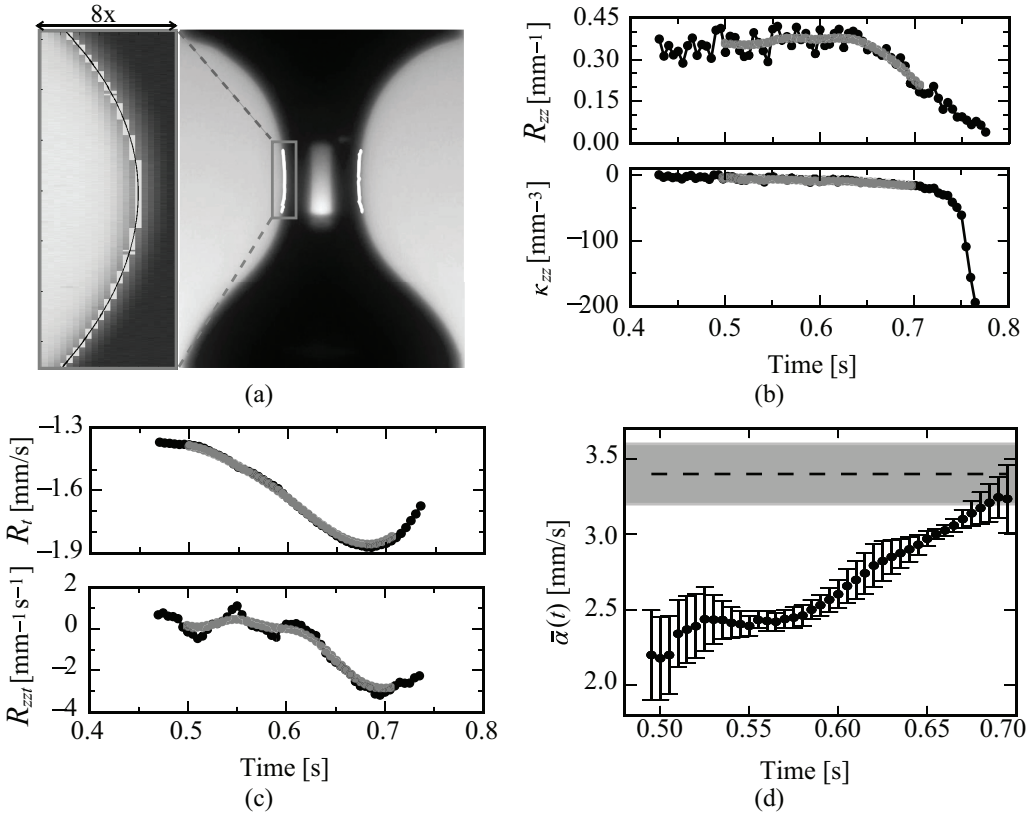

Figure 2.1: (a) A Newtonian silicone oil filament (μ = 1.0 Pa-s) in a CBR experiment 600 ms before break-up. The edge detection scheme applied within a domain that excludes the reservoirs results in a piecewise constant description of the free surface (white). A 6th order least-squares polynomial (black, zoomed in view) applied to the detected edge yields subpixel resolution. (b) The least-squares fits in space is still noisy in time (black) as shown here for R_{zz} and κ_{zz} evaluated at the filament waist. Results are processed with a triangular center-weighted running average (gray) to minimize the temporal fluctuations. (c) Temporal derivatives, R_t and R_{zzt}, are determined from a running least-squares fit in time (gray). This approach is comparable but less noisy than time derivatives determined by a central differencing scheme (black). (d) Ensemble averaged surface tension to viscosity ratios $\bar{\alpha}(t)$ determined by the differential analysis (2.7). Error bars represent the standard error of five replicate trials. The reference value α_{ref} and its uncertainty are represented by the dashed black line and the gray band, respectively. The results reach the expected value at late times due to filament asymmetry and is discussed in section 2.6.

which has the largest error. Measurements are discarded when the signal-to-noise ratio SNR for $R_{zzzz}(t)$ drops below unity, usually close to break-up. An individual trial is discarded when the SNR for $R_{zzzz}(t)$ is less than unity for all time.

The accuracy and errors for terms in (2.7) and subsequently in $\alpha(t)$ are sensitive to the least-squares domain size. A sufficiently large domain is desirable to achieve subpixel resolution for the interpolated profile by fitting a relatively low-order polynomial (6th-order) to hundreds of data points. However, the domain must be sufficiently small to be a local analysis for (2.7). The domain size was varied between $0.15L_f$ and $0.25L_f$ to minimize errors in $\alpha(t)$. Errors in $\alpha(t)$ can be greater than 20% for domains smaller than $0.2L_f$ because of inadequate radial dynamic range. The selected domain size is $0.2L_f$ because it is the domain that minimizes errors in $\alpha(t)$ near break-up (as $Bo(t) \to 0$ or $R(0,t) \to 0$).

We evaluated three sets of increasingly unfocused (blurry) image sequences to determine the impact of image sharpness on the detection and fit of the interface. Unfocused image sequences are created by applying a Gaussian filter to the image sequence from one experimental trial. Increasingly unfocused image sequences are obtained by increasing the standard deviation of the filter ($\sigma_{gauss} = 1, 3, 5$). Values of α determined from these out-of-focus image sequences differ from the original determination by less than 3% for all σ_{gauss}. The outcome of this sensitivity analysis indicates that our technique is robust to imperfect images.

2.5 Numerical Model

We simulate the evolution of a viscous Newtonian fluid filament by numerically solving the 1D model, (2.2) and (2.5), with Runge-Kutta 4th-order temporal integration and a 2nd-order central finite difference scheme on a spatial mesh. The mesh size for the 1D model results shown in figure 2.2 is 513 nodes. The scales for (2.2) and (2.5) are R_p, σ, and μ. The scaled bulk continuity equation is the same as (2.2)

and the scaled axial momentum equation is

$$(3w_z R^2)_z - \kappa_z R^2 - BoR^2 = Re(w_t + ww_z)R^2, \tag{2.8}$$

where $Bo = \rho g R_p^2/\sigma$ is the Bond number and $Re = \rho\sigma R_p/\mu^2$ is the Reynolds number.

The differential analysis (2.7) requires symmetry about the filament waist, as is the case when gravity and inertia are negligible. Thus, we consider the case when Re=0 and Bo=0. The initial condition for $R(z)$ at $t = t_1$, when the stretching process ends, is a symmetric, 6th-order polynomial constructed to have the same mass as an initially squat circular fluid cylinder with an initial aspect ratio $\Lambda_0 = 0.733$ and with a final strain $L_f/L_0 = 3$. The axial domain ranges from $-L_f/2R_p \leq z \leq L_f/2R_p$. The interface remains pinned to the plate edges, represented by $R(z = -L_f/2R_p, t) = R(z = L_f/2R_p, t) = 1$. The no-slip condition at the plates is $w(z = -L_f/2R_p, t) = w(z = L_f/2R_p, t) = 0$. The inertia-free limit of equations (2.2) and (2.8) contain only an evolution equation for $R(z)$. Therefore, the numerical procedure is as follows: for every $R(z)$, the corresponding $w(z)$ is solved from (2.8) and then $R(z)$ for the next time step is determined. The dimensionless time step is $\Delta t = 10^{-4}$. The simulation is halted when $R(0)/R_p$=0.003.

We determine spatial and temporal derivatives of R from the numerical data according to the same procedures for the experimental results (c.f. section 2.4). These spatial and temporal derivatives are combined to determine dimensionless surface tension to viscosity ratios $\alpha^*(t)$ by (2.7). Values of $\alpha^*(t)$ for the standard integral method (2.4) are evaluated by the necking rate determined from the 1D model.

We considered two additional symmetric initial conditions for $R(z)$, including the lubrication solution in (Spiegelberg *et al.* 1996). All initial conditions have the same mass as an initially squat fluid cylinder with $\Lambda_0 = 0.733$ and $L_f/L_0 = 3$. The three initial conditions yield similar results for $\alpha(t)$ determined by (2.7) and (2.4). This indicates (2.7) and (2.4) are insensitive to the initial conditions when the filament is

symmetric.

2.6 Results and Discussion

We experimentally evaluate the differential method (2.7) and the standard integral method (2.4) with five Newtonian silicone oils (0.35 Pa-s$<\mu<$10 Pa-s). We also evaluate (2.7) and (2.4) with numerical data from a preliminary 1D model for an evolving symmetric filament. The 1D model with a symmetric initial condition and negligible gravity and inertia satisfies axial symmetry about the filament waist, as required by (2.7). The initial and final aspect ratios in the 1D model are consistent with the experiments. The performances of (2.7) and (2.4) are compared in figure 2.2 where the scaled time-dependent surface tension to viscosity ratio $\alpha^*(t) \equiv \bar{\alpha}(t)/\alpha_{\text{ref}}$ is plotted versus $Bo(t)$. The reference values α_{ref} are determined by independent measurements of surface tension σ and viscosity μ at 20°C (section 2.3). The uncertainties in α_{ref} are determined by the errors in independent measurements of σ and μ. The uncertainties in the experimental $\alpha^*(t)$ are determined from the standard error in $\bar{\alpha}(t)$. Finally, the uncertainty in the expected value, α^*=1, is $\pm$5% and is determined from the error in α_{ref}.

The results in figure 2.2 are plotted against $Bo(t)$ to facilitate comparisons with McKinley & Tripathi (2000). The $Bo(t)$ is experimentally relevant because gravity makes the filament profile asymmetric, violating a required assumption for (2.7). Non-negligible gravitational effects are also problematic for (2.4) because it disrupts the assumption that F is constant in space. However, $Bo(t)$ is not suitable for the 1D model because gravity is not considered in the development of (2.7) nor (2.4). Even so, we present the 1D model results as a function of $Bo(t)$ determined by $g = 9.81\text{m/s}^2$ (instead of $g = 0$) to compare with experimental results. We discuss alternate approaches to rescaling our problem below.

In figure 2.2, the experimental results determined by (2.7) are scattered and noisy

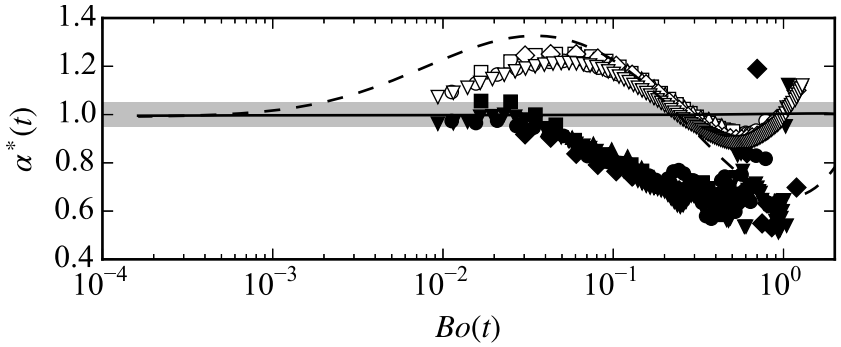

Figure 2.2: Experimental results for dimensionless surface tension to viscosity ratios $\alpha^*(t)$ for five Newtonian silicone oils (μ=0.35 Pa-s:●, μ=0.51 Pa-s:■, μ=1.0 Pa-s:▲, μ=4.8 Pa-s:◆, μ=10 Pa-s:▼) versus the local Bond number, $Bo(t)$. Differential method results (2.7) and standard integral method results (2.4) are shown in filled and open markers, respectively. Every third data point is plotted for clarity. Results determined by applying (2.7) and (2.4) to the 1D model data for a symmetric filament are shown by solid and dashed lines, respectively, with the solid line appearing as $\alpha^* = 1$ to graphical accuracy. Error bars are not shown for clarity. The gray band indicates the expected value, $\alpha^* = 1$, and its error.

shortly after the stretch ($Bo(t) > 0.3$). The scatter and noise decrease as $Bo(t)$ decreases until $Bo(t) < 0.2$ when the results become independent of the viscosity range considered. The differential method results for $\alpha^*(t)$ are 30 to 40% below the expected value of unity for $Bo(t) < 0.2$ but approach unity as $Bo(t)$ further decreases, reaching the expected value for $Bo(t) < 0.04$. Uncertainties in $\alpha^*(t)$ for $Bo(t) < 0.3$ are typically less than 10%. The result evaluated by applying (2.7) to the 1D model data is constant with $Bo(t)$ and deviates less than 0.5% from $\alpha^* = 1$. The result for α^* using the 1D model data is essentially error free because the 1D model and (2.7) share the same assumptions (axial symmetry about the waist, rectilinear flow, gravity- and inertia-free). Deviations in the experimental results from $\alpha^* = 1$ may also be caused by small viscoelastic and surfactant effects in the silicone oils that are not captured by the 1D model or (2.7). However, the deviations from $\alpha^* = 1$ are caused by filament asymmetry in the CBR experiments, as discussed below.

The experimental differential method results presented here are determined by

(2.7) without the inertial terms. The results for $\alpha^*(t)$ change the largest Re silicone oil (μ=0.35 Pa-s) by less than 5% and only near break-up ($Bo(t) < 0.04$) when such inertial terms are included. Therefore, inertial effects are small for the test fluids considered in this study and are not considered in (2.7) for the rest of this paper.

The experimental results determined by (2.4) in figure 2.2 overlap for all $Bo(t)$ shown and indicate that this method is independent of μ within the range tested. As $Bo(t)$ decreases $\alpha^*(t)$ first grows to a maximum then decreases again toward but does not reach unity. The 3% uncertainties in the experimental results determined by (2.4) are smaller than the 10% uncertainties in (2.7). The larger uncertainties in the differential method results stem from measurements of higher-order derivatives of $R(z,t)$ (discussed in figure 1). The result determined by applying (2.4) to the 1D model data when $Bo(t) > 0.0005$ follows a similar trend as the experimental results. However, $\alpha^*(t)$ determined from the 1D model data has larger deviations from $\alpha^* = 1$ than the experimental results. Furthermore, the minimum and maximum values predicted from the 1D model are shifted horizontally relative to the experimental results.

The differences between the experimental and 1D model results are related to gravitational effects on the necking rate $R_t(t)$ because the experiments are subjected to gravity while the 1D model results are not. These differences suggest that gravity increases $|R_t|$ at early times but decreases $|R_t|$ at longer times. Our findings are consistent with the numerical results with and without gravity in McKinley & Tripathi (2000). The variation in $\alpha^*(t)$ throughout earlier times, corresponding to high $Bo(t)$, in the filament evolution is due to force and curvature approximations. It also shows that $|R_t|$ is not constant and that a time-dependent correction factor is required in this regime. The 1D model result for α^* determined by (2.4) reaches a constant value of unity for $Bo(t) < 0.0005$. This indicates that the filament waist evolution does follow the similarity solution of Papageorgiou (1995) when $Bo(t) < 0.0005$ because

applying $X = 0.7127$ in (2.4) yields the correct result.

McKinley & Tripathi (2000) recommends that (2.4) be applied when $Bo(t) < 0.1$. However, experimental and 1D model results determined by (2.4) in figure 2.2 show that a smaller, stricter $Bo(t)$ criterion is necessary to improve the accuracy of measurements performed at the sample volume and strain conditions studied here. As mentioned by McKinley & Tripathi (2000), the time required to reach the self-similar regime described by Papageorgiou (1995) depends on multiple parameters including sample volume and strain. Therefore the $Bo(t)$ criterion to indicate when the filament evolution has reached the self-similar regime will also vary with sample volume and strain. For the conditions considered here, which correspond to those studied by McKinley & Tripathi (2000), the $Bo(t)$ criterion needs to be much stricter than $Bo(t) < 0.1$.

In addition to varying μ, we experimentally investigate the operating range of the differential method (2.7) with three sample volumes represented by plate radius R_p=2 mm, 3 mm and 4 mm, and three strains, L_f/L_0=2, 3 and 4.5. The largest strain case has the flattest (least curved) filament profile, indicated by small R_{zz} and R_{zzzz}. Despite our use of microscope objectives to resolve the filament, the profile for the largest strain case typically varies by less than 10 pixels in the radial direction. The radial variation in all other filament profiles are resolved with 2 to 4 times more pixels. The SNR for $R_{zzzz}(t)$ is below unity throughout the $L_f/L_0 = 4.5$ trials and therefore this condition has been excluded from our analysis.

The time-dependent experimental differential method results for varying μ, R_p, and L_f/L_0 are summarized in figure 2.3. The results are plotted as a function of two different time-varying parameters to determine a suitable dimensionless variable to characterize the filament evolution: $Bo(t)$ and dimensionless radius at the waist scaled by the local free surface curvature, R_{zz}. Time increases from right to left in each of the plots in figure 2.3. The results for all experimental conditions shown have

large deviations from α^*=1 at early times, corresponding to large dimensionless parameter values. The results generally approach and reach $\alpha^* = 1$ as the dimensionless parameters decrease corresponding to late times. The only exception is the smallest strain case which increases to $\alpha^* = 0.85$. The results plotted against $Bo(t)$ generally collapse while $\alpha^*(RR_{zz})$ do not when the sample volume or strain are varied. A universal curve is not expected for $\alpha^*(RR_{zz})$ because $R_{zz}(t)$ is affected by sample volume and strain.

Dimensionless CBR results are commonly presented according to time scaled by a visco-capillary or inertio-capillary time, $R(t)/R_p$, and $Bo(t)$ (McKinley & Tripathi 2000; Papageorgiou 1995; Anna & McKinley 2001; Bhat *et al.* 2010). A dimensionless time is problematic because it requires an arbitrarily defined reference time such as the time at break-up or the time when the plates come to rest. In addition, $R(t)/R_p$ is not suitable because (2.7) and (2.4) are local analyses and R_p is an external dimension relevant to the reservoir and not the fluid filament. Scaling the radius at the waist with a local length scale such as $R_{zz}(t)$, the free surface curvature at the waist, is a more meaningful approach to represent dimensionless radius in our local analysis (2.7). But the lack of a universal curve for $\alpha^*(RR_{zz})$ (shown in figure 2.3b) makes it difficult to develop a criterion to indicate when to apply (2.7) based on this parameter. For practical purposes we therefore suggest a criterion based on $Bo(t)$ to indicate when the differential method (2.7) is valid. Theoretically $Bo(t)$ is not a relevant parameter because gravity is neglected in the differential method (2.7) to enforce axial symmetry and ultimately avoid an axial fluid velocity measurement at the waist. Gravity (and inertia) is also neglected in (2.4) to avoid a spatially varying axial force. Even when gravitational effects are included, (2.7) is not explicit in g because it does not appear in the differentiated equations after being evaluated at the filament waist. Instead the effect of gravity is detected in the filament shape because it disrupts the axial symmetry required by (2.7).

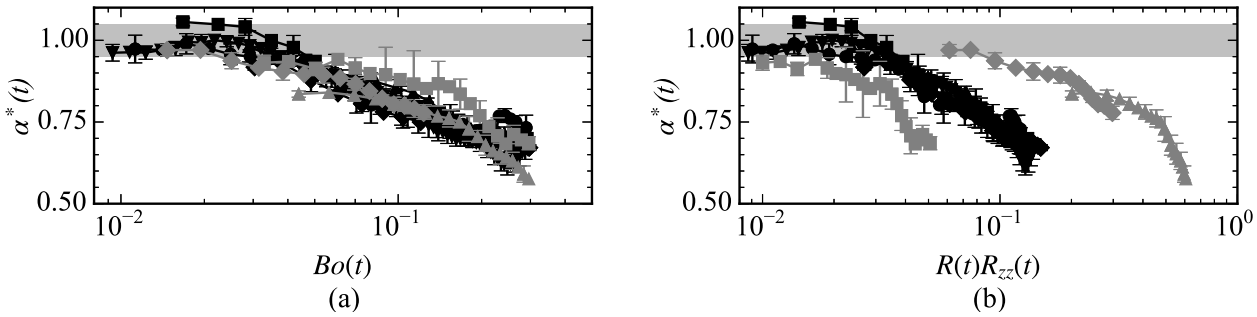

Figure 2.3: Experimental results for dimensionless surface tension to viscosity ratios $\alpha^*(t)$ determined by (2.7) plotted against two dimensionless time-dependent parameters. Results are shown for five Newtonian silicone oils (μ=0.35 Pa-s:●, μ=0.51 Pa-s:■, μ=1.0 Pa-s:▲, μ=4.8 Pa-s:◆, μ=10 Pa-s:▼), three sample volumes ($R_p = 2$ mm: ◆, $R_p = 3$ mm: ▲, $R_p = 4$ mm: ■), and two strains ($L_f/L_0 = 2$: ▲ , $L_f/L_0 = 3$: ▲). Error bars are the standard error of five replicated trials. Every 2nd data point is shown for clarity and error bars are shown for every 4th point. The gray band indicates the expected value, $\alpha^* = 1$, and its error.

Figure 2.3a shows that differential method results are accurate for $Bo(t) < 0.04$. The experimental results are summarized in figure 2.4 where time-averaged differential method results $\langle\alpha^*\rangle$ are plotted against viscosity μ except for the $L_f/L_0 = 2$ case because the series terminates early owing to limited temporal resolution. The results in figure 2.4 are determined by averaging all values of $\alpha^*(t)$ for $Bo(t) < 0.04$. The uncertainties in $\langle\alpha^*\rangle$ are one standard deviation for values of $\alpha^*(t)$ when $Bo(t) < 0.04$.

Values of $\langle\alpha^*\rangle$ determined by (2.7) for the five Newtonian silicone oils agree with the expected value. These time-averaged results are relatively constant with respect to viscosity and are independent of sample volume (with an outlier at $R_p = 4$ mm). Uncertainties in $\langle\alpha^*\rangle$ for all cases in figure 2.4 are less than 4%.

Figures 2.2 and 2.3 indicate the appropriate range to analyze differential method results is at late times corresponding to $Bo(t) < 0.04$. We examine the assumptions made in deriving (2.7) to identify the cause for deviations from $\alpha^* = 1$ at earlier times (larger $Bo(t)$). The symmetry condition required by (2.7) is mainly disrupted by gravitational effects (larger sample volumes) for the experimental conditions in-

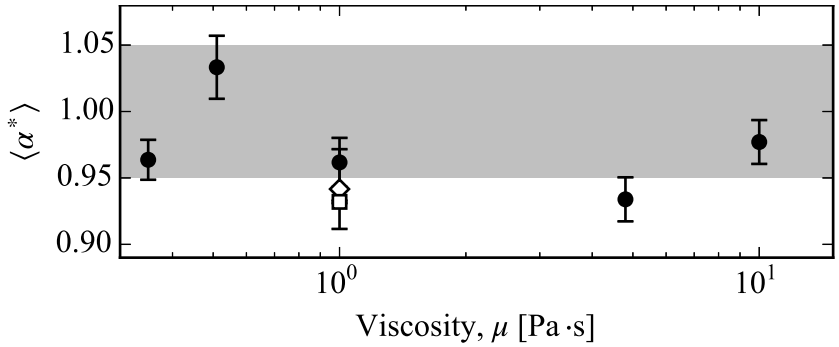

Figure 2.4: Experimental results for time-averaged dimensionless surface tension to viscosity ratios $\langle \alpha^* \rangle$ determined by the differential method (2.7) versus viscosity, μ. Results are shown for five Newtonian silicone oils (0.35 Pa-s$<\mu<$10 Pa-s:●) and three sample volumes (R_p=2 mm:◇, R_p=3 mm:●, R_p=4 mm:□). Results are determined by averaging over $Bo(t) < 0.04$ and error bars represent one standard deviation. The $L_f/L_0 = 2$ result does not generate a time-averaged value because the data set does not extend past $Bo(t) < 0.04$. The gray band indicates the expected value, $\alpha^* = 1$, and its error.

vestigated here. When the filament is asymmetric, two additional terms requiring a velocity measurement at the waist, $wR_{zzz}/\kappa_{zz}R$ and $ww_{zz}/6\nu\kappa_{zz}$, would need to be included in (2.7) to determine α. To maintain a purely geometric approach, we measure the asymmetry about the waist to determine when the two additional terms may be considered negligble. We define an asymmetry measure

$$\Omega(t) = \frac{|R_{zzz}(t)|}{R_{zz}^2(t) + |R_{zzzz}(t)|^{2/3}}. \tag{2.9}$$

This definition compares the relative magnitudes of $R_{zzz}(t)$, a measure of filament asymmetry about the waist, to the gradients of curvature that drive the filament evolution.

The differential method results for $\alpha^*(t)$ versus asymmetry $\Omega(t)$ for varying μ, R_p, and L_f/L_0 are plotted in figure 2.5 for $Bo(t) < 0.3$. Excluded results for larger $Bo(t)$ are noisy with uncertainties greater than 10% (see figure 2.2). Values of $\alpha^*(t)$ generally follow the same behavior. At short times $\Omega(t)$ increases toward its maximum and α^* is underestimated, typically by 30%. For the viscosity range considered, $\alpha^*(t)$

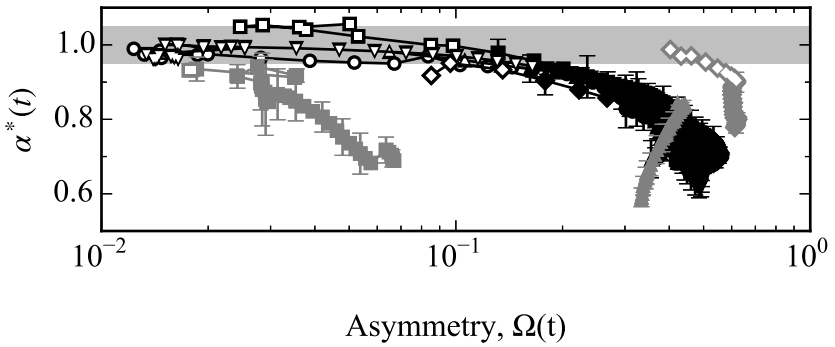

Figure 2.5: Experimental results for dimensionless surface tension to viscosity ratios $\alpha^*(t)$ determined by (2.7) versus asymmetry $\Omega(t)$ (2.9) for $Bo(t) < 0.3$. Results are shown for five Newtonian silicone oils (μ=0.35 Pa-s:●, μ=0.51 Pa-s:■, μ=1.0 Pa-s:▲, μ=4.8 Pa-s:◆, μ=10 Pa-s:▼), three sample volumes (R_p = 2 mm: ◆, R_p = 3 mm: ▲, R_p = 4 mm: ■), and two strains (L_f/L_0 = 2: ▲ , L_f/L_0 = 3: ▲).Unfilled markers represent values when $Bo(t) < 0.04$. Error bars are the standard error of five replicated trials and are shown on every 3rd data point for clarity. The gray band indicates the expected value, $\alpha^* = 1$, and its error.

grows gradually as $\Omega(t)$ approaches its maximum. In contrast, $\Omega(t)$ grows gradually compared to the increase in $\alpha^*(t)$ for $R_p = 2$ mm and $L_f/L_0 = 2$. Unlike other results, $\Omega(t)$ generally decreases when $Bo(t) < 0.3$ for the $R_p = 4$ mm case.

The differential method results approach $\alpha^* = 1$ from below as asymmetry decreases. Generally, $\alpha^*(t)$ reaches unity near break-up ($Bo(t) < 0.04$) as $\Omega(t)$ rapidly decreases, with the exception of noisy $\alpha^*(t)$ when asymmetry becomes small. In addition, the overall asymmetry decreases with growing R_p despite our expectations that a larger sample volume would have greater asymmetry, especially before stretching. The errors in $\alpha^*(t)$ also grow with increasing R_p. This behavior indicates that measurements for the larger samples are more challenging because of smaller axial curvatures caused by larger gravitational effects. Methods to reduce noise in measuring R and its derivatives are part of continuing work.

Figure 2.5 shows that axial symmetry is a key requirement to develop a geometric differential analysis (2.7). The negligible error in comparing (2.7) to the 1D symmetric model demonstrates that most of the experimental error is due to asymmetry.

Discrepancies in $\alpha^*(t)$ determined by (2.7) is attributed to the missing velocity terms that diminish as the asymmetry decreases near break-up.

Figure 2.5 also shows no universal curve, as expected, for $\alpha^*(\Omega)$ because filament asymmetry is affected by the initial Bond number (sample volume) and the strain as well as the initial aspect ratio, initial asymmetry and strain rate. Furthermore, filament asymmetry is indicated by deviations of $R(z)$ and $w(z)$ from purely even and odd functions, respectively, and hence our definition of $\Omega(t)$ (2.9) is incomplete. All curves in figure 2.5 demonstrate that the differential analysis (2.7) accurately determines α^* when asymmetry is sufficiently small and $d\alpha^*/d\Omega \to 0$ (or $d\alpha^*/dBo(t) \to 0$). The asymmetry should be assessed as sufficiently small compared to the initial asymmetry. We are not yet able to evaluate the asymmetry before and during the stretching process because microscope objectives improve radial resolution but limit the field-of-view. In the future a cylindrical lens will enable measurements of the entire filament evolution while increasing the radial resolution. As a proxy, sufficiently small asymmetry for accurate determination of α^* occurs when $Bo(t) < 0.04$ and $d\alpha^*/dBo(t) \to 0$.

2.7 Conclusions

Capillary break-up rheometry is an established technique for measuring flow properties such as surface tension and viscosity in the context of elongational flows when rheological differences and surface rheology are emphasized. We have demonstrated a 1D, Newtonian differential analysis (2.7) that requires gradients of filament curvature to determine the surface tension to viscosity ratio α when axial force measurements are not taken for capillary breakup rheometry. Our differential approach for Newtonian fluids (2.7) requires fewer assumptions than the standard integral method (2.4) and is the first step for characterizing extensional flows from the shape of the free surface profile. We recommend the differential method when measured values must

be accurate to within 10%.

Axial symmetry about the filament waist (where $R_z = 0$) is a major requirement for (2.7) to maintain a purely geometric approach (i.e. when no velocities are measured). The differential method evaluated by data from a 1D model for a symmetric filament without gravity or inertia is well within 0.5% of $\alpha^* = 1$, the expected value, throughout the simulation. The experimental results for five silicone oils (0.35 Pa-s$<\mu<$10 Pa-s), three sample volumes, and two strains also agree with $\alpha^* = 1$ when the asymmetry is sufficiently small near filament break-up. Deviations from $\alpha^* = 1$ in the experiments occur at early times when asymmetry Ω is large.

We recommend applying (2.7) when the asymmetry is sufficiently small relative to the initial asymmetry and $d\alpha^*/d\Omega \to 0$. Alternatively, $Bo(t) < 0.04$ and $d\alpha^*/dBo \to 0$ may be used as a proxy for the asymmetry evaluation. The error for all terms in (2.7) should be monitored, particularly for $R_{zzzz}(t)$. Measurements should be discarded when the signal-to-noise ratio for $R_{zzzz}(t)$ is below unity.

We acknowledge that measurements near filament break-up are challenging due to the spatial and temporal limitations of the imaging set-up. Inertial, viscoelastic, and surfactant effects may also begin to dominate near break-up. These challenges may be avoided by enforcing symmetry in the filament to apply (2.7) at earlier times. Filament symmetry may be achieved by testing smaller sample volumes and/or moving both plates in equal and opposite directions. Alternate deformation profiles that maintain symmetry but avoid break-up are also recommended.

Ongoing efforts will focus on improving the accuracy and error in the differential analysis by optimizing the least-squares polynomial fits of the filament free surface. These efforts include increasing the radial resolution and subsequently the degrees of freedom for the least-squares regression with a cylindrical lens and an edge detection scheme that uses grayscale more effectively. The domain size and the degree of the polynomial fit will also be further investigated to minimize error in the differential

approach (2.7). We are also developing additional differential methodologies based on the 1D model to quantify individual flow properties from a single elongated filament.

CHAPTER III

One-dimensional non-Newtonian Analyses without Stretching

3.1 Introduction

In the previous chapter we developed a 1D differential approach (2.7) to characterize material properties, specifically the surface tension to viscosity ratio α, from an evolving Newtonian filament. We now expand our 1D differential methods to characterize non-Newtonian fluids.

The "tackiness" or "stickiness" of a (saliva) filament may be attributed to extensional viscoelastic properties of long-chained molecules (such as mucins) or by surfactants (such as in soap films). Saliva viscoelasticity and its implications on health diagnosis are commonly studied both in shear and extension (Stokes & Davies 2007; Zussman *et al.* 2007; Haward *et al.* 2011; Turcanu *et al.* 2015; Wagner 2015). Less is known about surfactant effects on saliva filament dynamics but Kazakov *et al.* (2009) shows significant differences in the dynamic surface tension measurements for saliva in children with cavities and without cavities. Therefore, there is some evidence that characterizing saliva's surface activity may be useful for health diagnosis.

In this chapter, we first study the role of surfactants in low-viscosity filament dynamics with a simple experiment. We also investigate 1D viscoelastic filament

dynamics with a numerical model to assess the validity of the differential Newtonian analysis (2.7) for characterizing the initial viscous regime in the filament evolution. In particular, we evaluate the performance of (2.7) for viscous and inviscid fluids with varying viscoelastic effects.

Since we now examine fluids with memory (where the extra stress is nonlinearly related to the strain-rate), the deformation (stretch) history should be included. However, the typical development of CBR analyses (Bazilevsky *et al.* 1990; Entov & Hinch 1997; Bousfield *et al.* 1986; Renardy 1994; Clasen *et al.* 2006*a*) assumes a long, unstable filament with zero initial polymer stresses at the start of the CBR measurement. Additionally, the fluid is modeled with freely moving contact lines at the solid plates with constant 90 degrees contact angles, represented by Neumann boundary conditions for $R(z)$. These assumptions do not accurately represent the physical state of a non-Newtonian filament at the start of the CBR measurement (Anna & McKinley 2001). Nevertheless, these assumptions simplify the 1D analysis and are still useful for investigating trends in viscoelastic filament dynamics. We will delay a more accurate CBR model to chapter IV, where the stretching phase will be included.

3.2 Surfactants

Previously we investigated Newtonian filament dynamics under the assumption of constant surface tension. However, the presence of surface active constituents or surfactants (Kazakov *et al.* 2009; Proctor *et al.* 2005; Carpenter 2013) may result in spatially- and temporally-varying surface tension. Therefore, we investigate the role of surfactants on filament dynamics.

Surfactants are present in many commercial and industrial applications, such as pharmaceutical products, detergents, and ink-jet printing. They are frequently utilized to manipulate the break-up dynamics of droplets and jets. At low concentrations, surfactants adsorb to interfaces and alter the surface tension σ. Variations in

surfactant concentration on the interface lead to surface tension gradients and consequently impose a shear stress on the free surface. This tangential stress, termed the Marangoni stress, drives the flow toward regions of higher surface tension and may help or hinder capillary-driven instabilities (Rosen & Kunjappu 2012).

We are particularly interested in the effect of Marangoni flows on low-viscosity fluid filament dynamics because saliva's viscosity is similar to that of water (Bhat *et al.* 2010; Carpenter 2013; Zussman *et al.* 2007). The linear stability analysis by Timmermans & Lister (2002) shows insoluble surfactants do not significantly reduce the maximum growth rate for a disturbance in a low-viscosity fluid or affect the wavelength where the maximum growth rate k_{max} occurs. In contrast, the linear stability analysis for a viscous fluid shows increasing surfactant strength dramatically reduces the maximum growth rate and shifts k_{max} to longer wavelengths. Ambravaneswaran & Basaran (1999) and Liao *et al.* (2006) each show an insoluble surfactant has little impact on increasing the limiting length of a low-viscosity filament during stretching. Additionally, Ambravaneswaran & Basaran (1999) and Liao *et al.* (2006) also show the filament limiting length increases with viscosity. These studies indicate surfactant effects depend on viscosity for two reasons. First, Marangoni flows cannot persist without a restorative force provided by viscosity. Additionally, the effects of surface tension gradients on the free surface are not transmitted to the bulk flow without viscosity (Timmermans & Lister 2002; Liao *et al.* 2006). Furthermore, surfactants are swept away from the filament waist near break-up and thus its evolution is similar to that of filament without surfactant (Craster *et al.* 2002; Timmermans & Lister 2002).

We performed a set of qualitative experiments with a homemade bubble solution to investigate surfactant effects on low-viscosity fluid filament dynamics. The simplest bubble solution may be created with dish soap and water. The ratio of dish soap to water in bubble recipes found online varies widely, from 1:24 to 1:1 (Agee 2014; Sci 2011). A soap bubble is a spherical film that consists of a thin water layer between

two layers of soap molecules. Each soap molecule has a hydrophilic head and a hydrophobic tail. Due to interactions with the water molecules, the hydrophobic tails are forced to stick out of the water at the surface, into the air (Gennes & Brochard-Wyart 2004).

Bubbles created from a soap-water mixture are short-lived. Many bubble solutions also add glycerin (a.k.a. glycerol or glycerine) to the dish soap and water mixture. The ratio of glycerin to water also varies across these formulations, from as low as 1:192 to 1:1. Glycerin extends the lifetime of soap films and bubbles by slowing the evaporation of water and increasing the viscosity of the mixture to delay the draining (Gennes & Brochard-Wyart 2004; Isenberg 1978). Corn syrup is a suitable and more readily available alternative to glycerin in bubble solutions.

Our bubble solution was prepared with a 1:24 dish soap (Kirkland Signature Evironmentally Friendly Ultra Liquid Dish Soap) to water ratio and a 1:86 glycerin (Sigma-Aldrich) to water ratio. We used a small amount of glycerin to maintain a viscosity similar to water. The mixture was exposed to ambient conditions for at least 12 hours to allow any alcohols in the dish soap to evaporate.

The qualitative extensional behavior of this simple surfactant solution was evaluated by stretching a small drop ($\sim$1 mm^3) between forefinger and thumb. We experienced unexpected difficulties forming a filament with the bubble mixture. The fluid sample ruptured before a filament could be observed. In fact, the bubble solution's filament forming capabilities were not noticeably different from that of a similarly sized water droplet. In contrast, the bubble solution easily formed a relatively long-lived film as observed by extracting a ring from the mixture. The results of our qualitative experiments are consistent with the previous findings (Timmermans & Lister 2002; Ambravaneswaran & Basaran 1999; Liao *et al.* 2006) that surfactants do not significantly impact the filament formation and dynamics of low-viscosity fluids. Therefore, we conclude that surfactants do not play a significant role in the bulk

flow of saliva filament dynamics. Proctor *et al.* (2005) does show that saliva's surface active constituents such as statherin, a protein, and calcium ions do affect the rheological properties of saliva films and have implications for maintaining moist tissues and providing lubrication between surfaces in the oral cavity. However, the study of saliva surface rheology is beyond the scope of this work.

3.3 Viscoelastic Models

We investigate viscoelastic effects on filament dynamics because saliva's viscoelastic nature has been demonstrated in shear and extension. Saliva exhibits shear-thinning (Schwarz 1987; van der Reijden *et al.* 1993; Stokes & Davies 2007) and the formation of beads-on-a-string BOAS in elongation (Bhat *et al.* 2010). Therefore, a suitable viscoelastic model to study saliva must contain these features. We begin our selection process with the Maxwell, Oldroyd-B, and FENE-P models because they are well studied and commonly considered in investigations related to saliva viscoelasticity (Stokes & Davies 2007; Zussman *et al.* 2007; Bhat *et al.* 2010; Bazilevsky *et al.* 2011; Wagner *et al.* 2015; Clasen *et al.* 2006*a*).

3.3.1 Maxwell, Oldroyd-B and FENE-P models

The Maxwell model is the simplest linear viscoelastic continuum mechanics theory. It combines the constitutive theories for a Newtonian fluid and Hookean solid to describe a material with viscous and elastic properties. A useful mechanical representation of the Maxwell model is a dashpot (Newtonian fluid) and infinitely extensible linear spring (Hookean solid) in series. The Maxwell model forms the basis of many viscoelastic constitutive theories and therefore we discuss some of its characteristics here. The most general differential expression for the Maxwell model is

$$\tau_{ij} + \lambda \left(\frac{\mathscr{D}\tau_{ij}}{\mathscr{D}t} - a[\tau_{ik}\dot{\gamma}_{kj} + \dot{\gamma}_{ik}\tau_{kj}] \right) = 2\mu_0 \dot{\gamma}_{ij}, \tag{3.1}$$

where τ_{ij} is the total deviatoric stress tensor, λ is the polymer relaxation time, and μ_0 is the total zero-shear viscosity. The symmetric strain-rate tensor is defined as $\dot{\gamma}_{ij} = \frac{1}{2}(u_{i,j} + u_{j,i})$. The Jaumann (or co-rotational) derivative is a type of frame invariant time derivative and is given as

$$\frac{\mathscr{D}(\cdot)}{\mathscr{D}t} = \frac{D(\cdot)}{Dt} + \omega_{ik}(\cdot)_{kj} - (\cdot)_{ik}\omega_{kj}, \tag{3.2}$$

where $D(\cdot)/Dt$ is the material derivative and the antisymmetric strain-rate tensor (or vorticity tensor) is defined as $\omega_{ij} = \frac{1}{2}(u_{j,i} - u_{i,j})$. The upper-convected time derivative,

$$\begin{aligned} \overset{\triangledown}{(\cdot)} &= \frac{\mathscr{D}(\cdot)}{\mathscr{D}t} - (\dot{\gamma}_{ik}(\cdot)_{kj} + (\cdot)_{ik}\dot{\gamma}_{kj}) \\ &= \frac{D(\cdot)}{Dt} - (u_{i,k}(\cdot)_{kj} + (\cdot)_{ik}u_{j,k}), \end{aligned} \tag{3.3}$$

is another frame invariant time derivative commonly encountered in fluid rheology.

Equation (3.1) encompasses several variations of the Maxwell model. These variations depend on the type of frame invariant time derivative considered and are obtained by adjusting the value of a. Although the Maxwell model (3.1) is a continuum mechanics theory, the parameter a can be interpreted to represent the amount of slip between molecules. The parameter a may vary from $-1 \leq a \leq 1$ but values in the range $0 \leq a \leq 1$ are the most relevant to polymer rheology studies (Petrie 1979). The co-rotational Maxwell (CRM) model or the upper-convected Maxwell (UCM) model is obtained for $a = 0$ or $a = 1$, respectively.

The CRM model qualitatively describes shear thinning. In contrast, the UCM model qualitatively describes extension thickening but not shear thinning (Bird *et al.* 1987*a*; Larson 1988). A model combining the responses in shear and extension of the

CRM and UCM models selects $0 < a < 1$. Furthermore, a non-zero value of a can relieve the singularity in the extensional viscosity predicted by the UCM model that occurs at finite extension rates (Petrie 1979). This singularity is a result of modeling the Hookean solid as an infinitely extensible spring.

The Oldroyd-B model for the total deviatoric stress is the viscoelastic model associated with the original CBR analysis (Bazilevsky *et al.* 1990; McKinley & Tripathi 2000) and the basic model for dilute polymer solutions, like saliva (Bhat *et al.* 2010). The Oldroyd-B model represents a suspension of polymer chains as non-interacting, infinitely extensible Hookean dumbbells (Clasen *et al.* 2006*a*; Bird *et al.* 1987*a*). A common representation of the Oldroyd-B model expresses the total deviatoric stress as the sum of a Newtonian solvent stress $\tau_{ij}^s = 2\mu_s\dot{\gamma}_{ij}$ and a non-Newtonian polymer stress τ_{ij}^p. Superscripts 's' and 'p' are employed as labels for the stresses to avoid confusion with tensor notation. The polymer stress is modeled by the UCM theory, obtained by setting $a = 1$ and $\mu_0 = \mu_p$ in (3.1) (Larson 1988; Bird *et al.* 1987*a*; Petrie 1979). The solvent and polymer shear viscosities (at zero-shear) are represented by μ_s and μ_p, respectively, and are related to the total viscosity $\mu_0 = \mu_s + \mu_p$.

Decomposing the total stress tensor into contributions from the solvent and the polymer is commonly seen in kinetic theories. In fact, the Oldroyd-B model also has a kinetic theory representation for the polymer stress

$$\tau_{ij}^p = \frac{\mu_p}{\lambda}\left(f(R)A_{ij} - \delta_{ij}\right), \tag{3.4}$$

where A_{ij} is the dimensionless conformation tensor describing the orientation and extension of the polymers, δ_{ij} is the identity tensor, and $f(R)$ is a model for the spring force law. It will be shortly shown that $f(R) = 1$ in the Oldroyd-B model. The evolution of A_{ij} is governed by

$$\overset{\triangledown}{A}_{ij} = -\frac{1}{\lambda}(f(R)A_{ij} - \delta_{ij}). \tag{3.5}$$

The continuum mechanics Oldroyd-B representation for τ_{ij}^p may be determined from the kinetic theory representation (3.4) without a closure approximation (Oliveira 2009). The derivation is simple and begins by applying the upper-convected derivative (3.3) to (3.4), assuming μ_p and λ are constants

$$\overset{\triangledown}{\tau}_{ij}^p = \frac{\mu_p}{\lambda}\left(\overset{\triangledown}{A}_{ij} - \overset{\triangledown}{\delta}_{ij}\right). \tag{3.6}$$

This result is then combined with $\overset{\triangledown}{\delta}_{ij} = -2\dot{\gamma}_{ij}$, (3.4) and (3.5) to give

$$\tau_{ij}^p + \lambda\overset{\triangledown}{\tau}_{ij}^p = 2\mu_p\dot{\gamma}_{ij}. \tag{3.7}$$

Comparing (3.7) with (3.1) when $a = 1$ confirms the Oldroyd-B polymer stress derived from kinetic theory is equivalent to the continuum mechanics model, specifically τ_{ij}^p modeled by the UCM theory.

The Oldroyd-B model exhibits extension thickening and predicts an infinite extensional viscosity at finite strain-rates (Bird *et al.* 1987*a*). This is unsurprising given that the polymer stress is modeled by the UCM model which exhibits the same characteristics. Renardy (1994) also shows that an Oldroyd-B fluid thread never breaks up. However, the Oldroyd-B model is the simplest viscoelastic model able to predict BOAS for polymer solutions (Bhat *et al.* 2010; Ardekani *et al.* 2010).

The unphysical singularity in the UCM and (consequently) Oldroyd-B theories is addressed by modeling the polymer chains as Hookean dumbbells with finitely extensible non-linear elastic (FENE) spring forces. There are several variations of the FENE model and each propose a different description for the non-linear spring force. The FENE-P model is a closed formed theory for τ_{ij}^p (Herrchen & Öttinger 1997; Oliveira 2009; Bird *et al.* 1987*b*). The closure is provided by Peterlin's approximation to replace a ratio of two quadratic terms with a ratio of spatially averaged squared terms. More details on the development of FENE models may be found in Bird *et al.*

(1987*b*); Herrchen & Öttinger (1997); Keunings (1997).

The FENE-P polymer stress may be expressed by the same kinetic theory representation as the Oldroyd-B model (3.4). However, in the FENE-P model the spring force law is $f(R) = \frac{1}{1-R/L^2}$ where R is the trace of A_{ij} or $R = A^{zz} + 2A^{rr}$. Additionally, the finite extensibility parameter L is now introduced and defined as a ratio of the fully extended length of the dumbbell to its equilibrium length (Bird *et al.* 1987*b*). For an infinitely extensible spring, as in the Oldroyd-B model, $L \to \infty$ and therefore $f(R) \to 1$.

The FENE-P describes shear thinning and bounded extensional thickening (Herrchen & Öttinger 1997; Fontelos & Li 2004; McKinley 2005). In addition it has characterized saliva viscoelasticity in experimental studies (Stelter *et al.* 2000; Stokes & Davies 2007; Zussman *et al.* 2007). However, the FENE-P model so far does not predict BOAS (Oliveira & McKinley 2005; Wagner *et al.* 2005; Oliveira *et al.* 2006). We proceed with the Oldroyd-B model because it is the simplest viscoelastic model that describes BOAS formation. Issues with the singularity will be addressed by avoiding break-up.

3.3.2 Current 1D viscoelastic CBR analysis

The details for the viscoelastic CBR analysis introduced by Bazilevsky *et al.* (1990) are later given by Entov & Hinch (1997) in the context of a 1D multi-mode FENE-CR model. The original analysis is based on a filament where initial polymer stresses are zero. Although not explicitly stated by Entov & Hinch (1997), it is most likely for a cylindrical filament with a small radial profile perturbation.

The derivation of the original CBR viscoelastic analysis also begins with the local force balance at the filament mid-plane (1.1). When τ_{ij} is decomposed into Newtonian solvent and polymer stresses, the resulting force balance is similar to (2.1) and includes the elastic (polymer) stresses acting over the cross-sectional area

$$F = (-\sigma\kappa + 3\mu_s w_z + \tau^{p,zz} - \tau^{p,rr})\pi R^2 + 2\pi\sigma R, \text{ where } R_z = 0. \tag{3.8}$$

In the FENE-CR model, the polymer stresses are $\tau^{p,zz} = \frac{\mu_p}{\lambda}(fA^{zz} - 1)$ and $\tau^{p,rr} = \frac{\mu_p}{\lambda}(fA^{rr} - 1)$, respectively. The 1D representations for the evolution of A^{zz} and A^{rr} are

$$fA^{zz} + \lambda(A_t^{zz} + wA_z^{zz} - 2w_z A^{zz}) = 1 \tag{3.9a}$$

$$fA^{rr} + \lambda(A_t^{rr} + wA_z^{rr} + w_z A^{rr}) = 1. \tag{3.9b}$$

In the early stage of evolution, the stress is attributed to the solvent viscosity since the initial elastic (polymer) stresses in the filament are assumed to be zero. Furthermore, the elastic stresses only enter when the deformation is large. This regime is often referred to as the early viscous phase because the filament evolves due to viscous and capillary forces. When elastic stresses are negligible, (3.8) simplifies to the Newtonian force balance (2.1). The filament midpoint is observed to decrease linearly in this phase. The original analysis (Bazilevsky *et al.* 1990; Entov & Hinch 1997) and the subsequent correction (McKinley & Tripathi 2000) indicate material parameters, specifically the surface tension to viscosity ratio α, may be determined directly from the necking rate R_t at the filament waist. However, we show the limitations of this technique in chapter II.

The filament evolution enters a second regime once the elastic stresses have grown to the same order as the capillary and viscous stresses. The viscous stress then decreases with the strain-rate such that the capillary pressure balances the elastic stresses. The axial deformation is considered large relative to the radial deformation and thus $\tau^{p,zz} >> \tau^{p,rr}$. Additionally, the axial deformation is still small relative to the finite extension limit and therefore the Oldroyd-B model is valid in this phase.

The axial stress evolution at the waist is derived by evaluating the continuity

equation (2.2) at $R_z = 0$ to determine the axial strain rate $w_z = -2R_t/R$. Equation (3.9a) is also evaluated at $R_z = 0$ and the constant on the right-hand-side is neglected to ease one integration in time. The resulting expression combined with w_z at the filament midpoint gives

$$A^{zz} = \left(\frac{R(t_E)}{R(t)}\right)^4 \exp(-t/\lambda), \text{ at } R_z = 0 \text{ for } t > t_E. \tag{3.10}$$

Here it is noted that t_E marks the start of the second regime, often termed the elasto-capillary regime. An expression for the filament midpoint evolution is determined by neglecting the viscous and radial stress contributions in (3.8). After applying the same three approximations regarding F, the surface tension perimeter term, and κ made in the Newtonian force balance (c.f. section 2.1), the simplified force balance is combined with (3.10) to give

$$R(t) = R(t_E)\left(\frac{R(t_E)\mu_p}{\lambda\sigma}\right)^{1/3} \exp(-t/3\lambda), \text{ at } R_z = 0 \text{ for } t > t_E. \tag{3.11}$$

The exponential decrease in the filament midpoint predicted by (3.11) is the most recognizable feature of a thinning viscoelastic fluid thread. A prefactor of $2^{-1/3}$ (not include here) was later introduced in (3.11) by Clasen *et al.* (2006*a*) to account for the missing surface tension term in the original theory (Bazilevsky *et al.* 1990; Entov & Hinch 1997). However, the correction does not affect the rate of exponential thinning. Furthermore, combining (3.10) and (3.11) indicates $\tau^{p,zz}(t) \sim \exp(t/3\lambda)$ in the elasto-capillary phase.

In the final regime, the polymer chains become fully elongated and therefore the effects of finite extensibility can no longer be ignored. The elastic stress due to the polymer is unable to balance the capillary pressure. Additionally, the radial deformation is also significant and therefore $\tau^{p,rr}$ cannot be ignored. The filament midpoint once again thins linearly in time like a Newtonian fluid with a large, anisotropic vis-

cosity (Clasen *et al.* 2006*b*; Anna & McKinley 2001). The linear decay of the midpoint has been observed experimentally in the final stages of viscoelastic filament evolution (Liang & Mackley 1994).

The largest polymer relaxation time is commonly determined by applying (3.11) during the exponentially thinning regime. This approach works reasonably well for polymer solutions with various concentrations and molecular weights (Bazilevsky *et al.* 1990; Anna & McKinley 2001; Clasen *et al.* 2006*b*). The operating range for (3.11) is discussed in Rodd *et al.* (2005).

We focus our efforts on the initial phase of the filament evolution since the method (3.11) for characterizing λ works well. In particular, we investigate the possibility of determining α with the differential Newtonian analysis (2.7) developed in chapter II with numerical data generated by a 1D model for an evolving viscoelastic filament.

3.3.3 1D viscoelastic model and simulation

We model the 1D evolution of a viscoelastic filament in the absence of gravity with a single-mode (single relaxation time) Oldroyd-B model for simplicity, since we are interested in characterizing material parameters from early regimes when the effects of finite extensibility are negligible. The original 1D model discussed by Entov & Hinch (1997) considers viscoelastic contributions from a discrete spectrum of relaxation times representing a suspension of dumbbells with varying spring constants. However, experiments (Spiegelberg *et al.* 1996; Anna & McKinley 2001) and analysis (Clasen *et al.* 2006*a*) show the filament evolution is dominated by the largest relaxation time. Therefore, a single-mode model is a simple and reasonable approximation.

It is important to emphasize the typical development of CBR analyses (Bazilevsky *et al.* 1990; Entov & Hinch 1997; Bousfield *et al.* 1986; Renardy 1994; Clasen *et al.* 2006*a*) assumes a long, unstable filament with zero initial polymer stresses at the start of the CBR measurement. These assumptions may not accurately represent

the physical state of a non-Newtonian fluid after an imposed deformation (Anna & McKinley 2001). Nevertheless, these assumptions simplify the 1D analysis and are still useful for investigating trends in viscoelastic filament dynamics arising from various parameters such as Oh, De and S.

We consider the form of the Oldroyd-B constitutive theory that distinguishes the stress contributions from the Newtonian solvent and the non-Newtonian polymer. The set of 1D governing equations for mass and momentum and the stress evolution equations given by the Oldroyd-B model are scaled by R_p, σ, and an inertio-capillary time scale $t_c = \sqrt{\rho R_p^3/\sigma}$ and yields

$$(R^2)_t + (wR^2)_z = 0 \tag{3.12a}$$

$$(w_t + ww_z)R^2 = -\kappa_z R^2 + 3OhS(w_z R^2)_z + ((\tau^{p,zz} - \tau^{p,rr})R^2)_z \tag{3.12b}$$

$$\tau^{p,zz} + De(\tau_t^{p,zz} + w\tau_z^{p,zz} - 2w_z\tau^{p,zz}) = 2Oh(1-S)w_z \tag{3.12c}$$

$$\tau^{p,rr} + De(\tau_t^{p,rr} + w\tau_z^{p,rr} + w_z\tau^{p,rr}) = -Oh(1-S)w_z. \tag{3.12d}$$

Equation (3.12b) is similar to the axial momentum equation for Newtonian flow (2.5) but includes an extra term to account for contributions from the polymer. As in the previous chapter (c.f. section 2.2), κ is twice the mean curvature of the filament free surface

$$\kappa = \frac{1}{R(1+R_z^2)^{1/2}} - \frac{R_{zz}}{(1+R_z^2)^{3/2}}. \tag{3.13}$$

The form of the 1D viscoelastic equations (3.12) are derived by Bechtel *et al.* (1988) and are ubiquitous in extensional viscoelastic flow literature (Fontelos & Li 2004; Tembely *et al.* 2012; Anna & McKinley 2001; Clasen *et al.* 2006*a*; Ardekani *et al.* 2010). The evolution equations for the polymer stresses (3.12c-d) only contain one convective term. However, Schultz (1987) shows both convective terms are of the same order with a formal asymptotic expansion. For example, $u\tau_r^{p,zz}$ should be included

in the second term on the left in (3.12c). Unfortunately, the missing convective terms, $u\tau_r^{p,zz}$ and $u\tau_r^{p,rr}$, introduces r as an independent variable and would make the problem two-dimensional. Thankfully, the analysis of the CBR is very nearly pure elongation, especially at the midpoint of viscoelastic threads. Hence, the 1D approximation (Bechtel *et al.* 1988) may be more suitable here.

The scaled 1D viscoelastic model (3.12) includes three dimensionless parameters to characterize the contributions of λ, μ_s and μ_p: the Deborah number $De = \lambda/t_c$; the Ohnesorge number $Oh = \mu_0/\sqrt{\rho\sigma R_0}$, a comparison of viscous to inertial forces similar to a Reynolds number; and $S = \mu_s/\mu_0$. A Newtonian limit of the 1D Oldroyd-B model (3.12) is recovered when $De \to 0$. For healthy saliva in conventional CBR experiments, $De \sim 10^{-1} - 10^2$ and $Oh \sim 10^{-3} - 10^{-2}$ (Zussman *et al.* 2007; Turcanu *et al.* 2015; Wagner 2015). Values of S representative of healthy saliva characterized by shear rheometry (Stokes & Davies 2007) and extensional rheometry (Wagner 2015) range from $\sim 0.005 - 0.66$.

We consider the same 1D model as Clasen *et al.* (2006*a*) to verify our numerical approach. The 1D model (3.12) is solved numerically with a pseudospectral approach incorporating backward Euler temporal integration and a Chebyshev spatial scheme with N=129 nodes. Each dependent variable is represented by a linear combination of N polynomials, as shown for R

$$R(x) = \sum_{n=0}^{N} \hat{r}_n T_n(x), \tag{3.14}$$

where $T_n(x) = \cos(n\theta)$ is the nth Chebyshev polynomial of the first kind and is of degree n for $n \geq 0$. Chebyshev polynomials are defined on a domain $x = \cos(\theta) \in [-1, 1]$ where $\theta \in [0, 2\pi]$. The Chebyshev domain $x \in [-1, 1]$ may be mapped to another domain with a simple linear transformation. Equation (3.14) may also be represented by a sum of N cosine functions with $n = N$ modes

$$R(\theta) = \sum_{n=0}^{N} \hat{r}_n \cos(n\theta). \tag{3.15}$$

The magnitude of the Chebyshev coefficients, $\hat{r}_n$ for $R(z)$ (3.14 - 3.15), indicates the relative importance of the contribution from the nth mode. More details about Chebyshev polynomials and spectral methods may be found in references by Trefethen (2000), Boyd (2001), and Shen *et al.* (2011).

Our implicit Euler - Chebyshev numerical scheme is the same approach we apply to model the Newtonian filament dynamics throughout the deformation process presented later in chapter IV. Despite its lower-order accuracy, an implicit temporal integration scheme is necessary for modeling the deformation process to overcome challenges with numerical instabilities (sawtooth instabilities) that develop with a higher-order explicit temporal scheme such as 4th-order Runge-Kutta. The Chebyshev spatial scheme is employed to determine derivatives with spectral accuracy, to give the flexibility of enforcing non-periodic boundary conditions (c.f. chapter IV), and to provide finer resolution near the boundaries where sawtooth instabilities originate. Additional details regarding the numerical methods employed are discussed in appendix C.

As in Clasen *et al.* (2006*a*), the filament is initially a long cylinder with a small perturbation spanning the axial domain $-2\pi \leq z \leq 2\pi$. The initial filament free surface is symmetric and described by $R(z,0) = 1 + 0.05\cos(z/2)$. We begin with a quiescent fluid filament such that $w(z,0) = \tau^{p,zz}(z,0) = \tau^{p,rr}(z,0) = 0$. We also apply periodic-like boundary conditions for $R(z)$ and $w(z)$, $R_z(-2\pi, t/t_c) = R_z(2\pi, t/t_c) = 0$ and $w(-2\pi, t/t_c) = w(2\pi, t/t_c) = 0$, respectively.

The 1D Oldroyd-B model for the polymer stresses (3.12c-d) contains one z-derivative of τ^p_{ij}, indicating only one boundary condition is required for each stress component. However, this requires knowledge of the fluid deformation history at a particular location for all times. It is also unclear to which of the two boundaries the

boundary condition should be applied for the problem of capillarity-induced filament dynamics. Insight regarding the appropriate boundary conditions for the polymer stresses may be developed by considering various Newtonian limits of the 1D model (3.12) when the fluid contact line is pinned ($R = 1$ and $w = 0$ at the plates), as discussed in chapter IV. However, we summarize our rational here. The 1D Oldroyd-B model considered here (3.12) contains three Newtonian limits: $De \to 0$, $S \to 1$, and small deformations. When the fluid is pinned at the boundaries, w_z must also be zero to satisfy the no-slip boundary condition and continuity (3.12a). This implies $\tau^{p,zz} = \tau^{p,rr} = 0$ at the wall. As shown below, $\tau^{p,zz} = \tau^{p,rr} = 0$ is a solution to (3.12c-d) when $S \to 1$ and therefore the correct boundary conditions for the polymer stresses are naturally satisfied. However, $\tau^{p,zz}$ and $\tau^{p,rr}$ are non-trivial in the other two Newtonian limits, $De \to 0$ and small deformations, and therefore may not naturally satisfy homogeneous Dirchlet boundary conditions. It is desirable to avoid enforcing special boundary conditions for various limits of the 1D model (3.12). Fortunately, $w_z = 0$ is naturally satisfied at the plates and therefore we do not prescribe any boundary conditions on the polymer stresses. We also note that when the fluid contact angle rather than its contact line is prescribed, as is the case considered in this chapter, w_z must be non-zero at the plates to satisfy (3.12a). Thus, in the Newtonian limits of (3.12), $\tau^{p,zz}$ and $\tau^{p,rr}$ at the boundaries must vary with w_z in time. Hence, we also do not enforce boundary conditions on the polymer stresses when the fluid contact angle is fixed. Several previous studies (Yao *et al.* 1998; Yildirim & Basaran 2001; Vadillo *et al.* 2012; Tembely *et al.* 2012) also do not apply boundary conditions to the polymer stress evolution equations. In particular, Vadillo *et al.* (2012) and Tembely *et al.* (2012) justify this approach because both studies consider only weakly viscoelastic fluids ($De < 5$).

The 1D model (3.12) contains four evolution equations for $R, w, \tau^{p,zz}$ and $\tau^{p,rr}$. The backward Euler temporal integration scheme is implemented by first linearizing

the evolution equations (3.12). This yields a $4N \times 4N$ system of equations at each time step that is solved iteratively until the solution changes by less than 10^{-6} between two iterations. Spatial derivatives are determined spectrally by recurrence relations applied to the Chebyshev coefficients (Trefethen 2000; Boyd 2001; Shen *et al.* 2011). The Chebyshev coefficients are determined by applying a discrete cosine transform to to each dependent variable, $R(z), w(z), \tau^{p,zz}(z)$ and $\tau^{p,rr}(z)$, at each time step. The dimensionless time step is $\Delta t = 0.005$. The spatial and temporal meshes were refined until changes in $R(z)$ were less than 0.5%. This corresponds to changes in α^* of less than 0.001%.

The numerical schemes in Clasen *et al.* (2006*a*) (based on the numerical methods of Eggers & Dupont (1994)) use adaptive spatial and temporal meshes to resolve a larger range of time and length scales than is typically observed in Newtonian flow simulations. Clasen *et al.* (2006*a*) indicates these adaptive schemes are critical for investigating the elasto-capillary regime. Therefore, we monitor the quality of our 1D model (3.12) results to determine when our numerical simulation breaks down since it does not adaptively adjust the temporal and spatial meshes.

Sawtooth instabilities in the free surface profile $R(z)$ indicate that our numerical simulation is beginning to fail. These instabilities essentially add high-frequency noise to $R(z)$ and may be detected by monitoring the growth of Chebyshev coefficients associated with higher modes. We examine results for two simulations produced by our numerical scheme to develop a metric for evaluating when the simulation begins to fail.

Figure 3.1a shows the filament midpoint evolution R/R_p of a viscous viscoelastic fluid with $Oh = 3.16, De = 100$ and $S = 94.9$ determined by our numerical approach applied to the 1D model (3.12). These parameter values are taken from figures 3 and 4 in Clasen *et al.* (2006*a*). The result is plotted with time scaled by an inertio-capillary time scale to facilitate comparisons with Clasen *et al.* (2006*a*) although it is more

appropriate to consider a viscous time scale for $Oh = 3.16$. The result predicted by our numerical scheme, shown in a semilogarithmic plot, reproduces the midfilament evolution shown in figure 4 of Clasen *et al.* (2006*a*), also shown in a semilogarithmic plot. The initial viscous phase is identified qualitatively as an "inverted parabola." The following middle elastic regime when the filament midpoint decays exponentially appears as a linear decay in the semilogarithmic frame. The transition between the visco-capillary and elasto-capillary phases occurs between $20 < t/t_c < 30$.

Free surface profiles $R(z)$ throughout the simulation are shown in figure 3.1b. The profiles are chosen to demonstrate the filament shapes during the initial viscous phase and middle elastic regime. The profile at $t/t_c = 31.6$ is specifically selected to further demonstrate that our numerical scheme reproduces the results shown in figure 3b in Clasen *et al.* (2006*a*). At $t/t_c = 20$, in the visco-capillary regime, $R(z)$ is qualitatively described by an hourglass shape. At later times in the elasto-capillary regime, axial variations in $R(z)$ between the two reservoirs decay as shown for $t/t_c = 31.6$ and $t/t_c = 80$.

Figure 3.1c shows the magnitude of even Chebyshev coefficients for $R(z)$ at times corresponding to the profiles shown in figure 3.1b. The results are shown in a semilogarithmic plot. Odd modes are effectively zero because $R(z)$ is symmetric and therefore are omitted for clarity. The filament free surface profile is initially resolved by fewer than 20 modes and $\hat{r}_n$ decays rapidly as the mode n increases. The number of non-zero modes (coefficients) roughly doubles at $t/t_c = 10$ and quadruples at $t/t_c = 20$. Rapid growth in $|\hat{r}_n|$, particularly for $n > N/2$, occurs between $20 < t/t_c < 30$ and then the spectrum stays roughly constant through the end of the simulation at $t/t_c = 80$. In general, $|\hat{r}_n|$ decays more gradually with increasing n as time increases.

The substantial growth in $|\hat{r}_n|$, specifically for $n > N/2$, corresponds to the cross-over between the initial viscous and middle elastic regimes. Despite the large growth in $|\hat{r}_n|$ at higher modes, sawtooth instabilities are not detectable in the free surface

profiles at $t/t_c = 31.6$ and $t/t_c = 80$. Thus we examine a second example to develop a criterion to indicate when our numerical scheme becomes problematic.

Figure 3.2a presents the filament midpoint evolution for a viscoelastic filament with $Oh = 3.16, De = 94.9$ and $S = 0$ predicted by the 1D model (3.12). The result for R/R_p at the midpoint determined by our numerical scheme applied to (3.12) is presented in a semilogarithmic plot. The dashed line near the end of the simulation indicates when our numerical approach begins to fail and will be discussed shortly. The midfilament evolution decays as expected during the early viscous regime but a region of exponential decay is not observed. Instead, R/R_p passes through a minimum around $t/t_c = 13$ and then increases, indicating local growth.

Figure 3.2b presents selected free surface profiles throughout the evolution of a viscoelastic filament with $Oh = 3.16, De = 94.9$ and $S = 0$. The profile shown during the initial viscous phase at $t/t_c = 9$ has an hourglass shape similar to $R(z)$ at $t/t_c = 20$ in figure 3.1b. Around the end of the initial viscous phase at $t/t_c = 11$ $R(z)$ near the midpoint becomes slightly convex because the filament decays faster near the reservoirs than at the midpoint. As time increases, a bead forms at the filament midpoint due to local growth (figure 3.2a) and is shown in detail by $R(z)$ for $t/t_c \geq 14$. The sawtooth instabilities in $R(z)$ at $t/t_c = 14.4$ indicates our numerical scheme is starting to fail.

Figure 3.2c shows the spectrum of $|\hat{r}_n|$ for even modes corresponding to the filament profiles in figure 3.2b. Once again $\hat{r}_n$ associated with odd modes are effectively zero and therefore not shown for clarity. Values of $|\hat{r}_n|$ increase with time. For $t/t_c \leq 11$ $|\hat{r}_n|$ decreases as n increases and the decay becomes more gradual with time. At $t/t_c = 14$ $|\hat{r}_n|$ decreases slightly until $n \sim 80$ and then becomes relatively constant. When sawtooth instabilities are visible in $R(z)$ at $t/t_c = 14.4$ (figure 3.2c), $|\hat{r}_n|$ decreases gradually until $n \sim 45$ and then increases.

A comparison of the results shown in figure 3.1 and figure 3.2 demonstrates that

our numerical approach applied to the 1D model gives reasonable results when $|\hat{r}_n|$ decreases with increasing n. Sawtooth instabilities are detected from the spectrum of Chebyshev coefficients when the magnitude of coefficients at higher modes, particularly $n > N/2$, are greater than those at lower modes. Therefore we apply a linear fit to $|\hat{r}_n|$ for $n > N/2$ at each time step and identify problematic regions of our simulation when the slope of the fit is larger than zero, indicating increasing $|\hat{r}_n|$ with increasing n. We represent these problematic regions in our results by dashed lines, as shown in the midfilament evolution for $t/t_c > 12.5$ (figure 3.2a).

In the next sections we investigate the validity of our 1D differential Newtonian analysis (2.7) during the early viscous phase of viscoelastic filament evolution for various regions of the $Oh - De - S$ space with data generated by the 1D Oldroyd-B model (3.12).

3.3.4 Characterizing the early viscous regime – high-viscosity (large Oh)

We model the filament dynamics of viscous ($Oh = 3.16$) viscoelastic fluid threads with a range of relaxation times ($0 \leq De \leq 100$) and viscous polymer contributions ($0 \leq S \leq 1$) to evaluate the performance of our 1D Newtonian analysis (2.7) during the early viscous phase of filament evolution.

Figure 3.3a shows the midfilament evolution R/R_p predicted by the 1D Oldroyd-B model (3.12) for $Oh = 3.16, S = 0.25$ and $0 \leq De \leq 100$ plotted against t/t_c. The results are presented in a semilogarithmic plot. The transition between the visco-capillary to elasto-capillary phases shifts to earlier times as De increases and to smaller values of R at the waist. As $De \to 0$, a Newtonian limit of the 1D model (3.12), the exponential decay (elasto-capillary regime) becomes difficult to identify.

Figure 3.3b presents the same results as figure 3.3a, but rescales time by λ. In nearly uniaxial extensional flow (i.e. as in a CBR experiment) λ is the time scale representing viscoelastic stress growth (Eggers 1997; Rodd *et al.* 2005). Therefore we

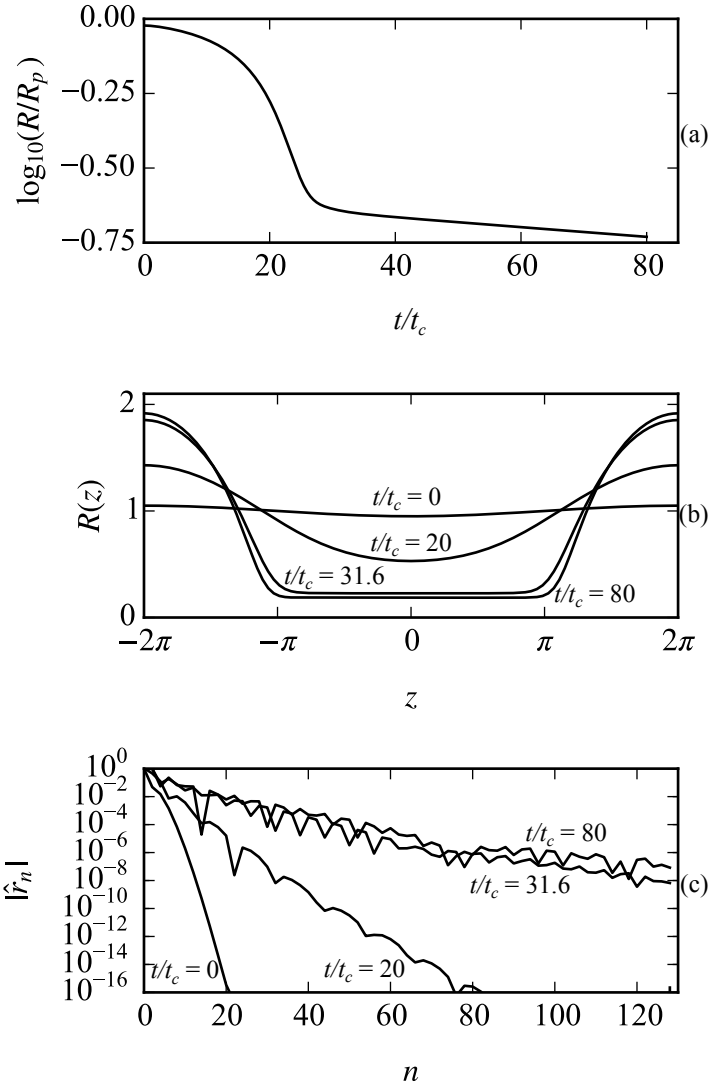

Figure 3.1: (a) Dimensionless filament midpoint evolution R/R_p for a viscous viscoelastic filament with $Oh = 3.16, De = 94.9$ and $S = 0.25$ as a function of dimensionless time t/t_c. The result is shown in a semilogarithmic (base 10) plot to facilitate comparisons with figure 4 in Clasen *et al.* (2006*a*); (b) Dimensionless free surface profiles $R(z)$ at select times throughout the filament evolution to illustrate the filament shapes during the early viscous regime and middle elastic phase; (c) Magnitude of even Chebyshev coefficients $|\hat{r}_n|$ at times corresponding to those shown in (b). Odd modes are effectively zero because $R(z)$ is symmetric and therefore are not shown.

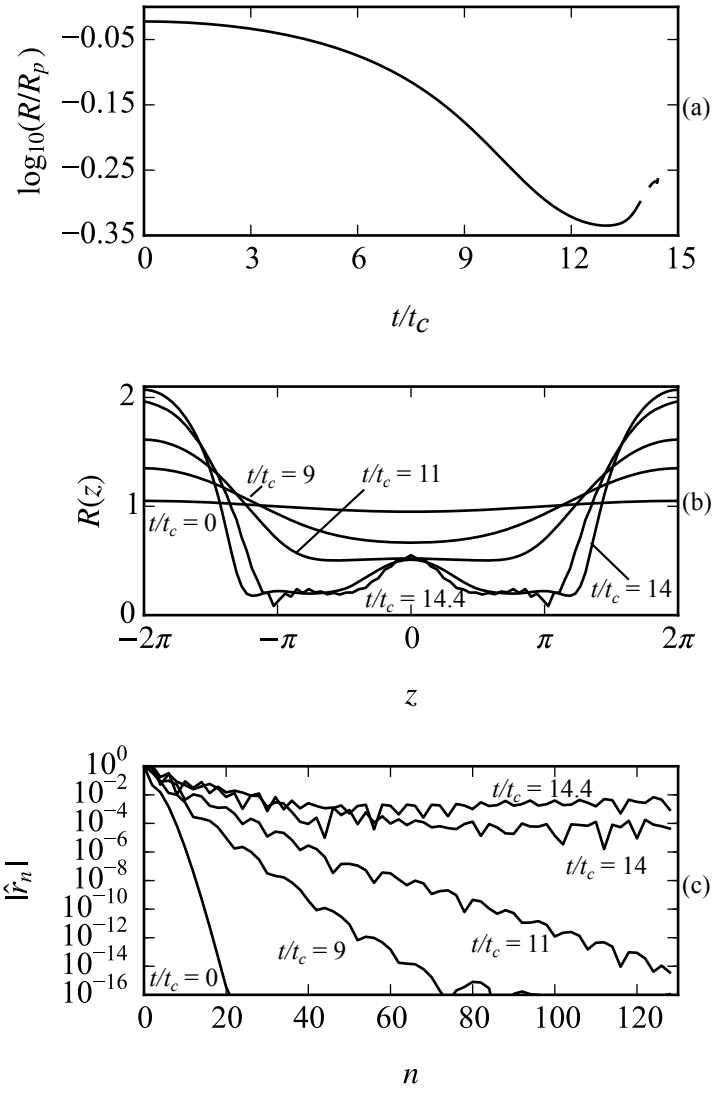

Figure 3.2: (a) Dimensionless filament midpoint evolution R/R_p for a viscous viscoelastic filament with $Oh = 3.16, De = 94.9$ and $S = 0$ as a function of dimensionless time t/t_c. The dashed line for $t/t_c > 14$ represents the results when our numerical scheme begins to fail; (b) Dimensionless free surface profiles $R(z)$ at select times to illustrate the filament shapes throughout the filament evolution. Sawtooth instabilities are visible in $R(z)$ at $t/t_c = 14.4$; (c) Magnitude of even Chebyshev coefficients $|\hat{r}_n|$ at times corresponding to $R(z)$ shown in (b). Odd modes are effectively zero because $R(z)$ is symmetric and therefore are not shown. When sawtooth instabilities are visible in $R(z)$ at $t/t_c = 14.4$, $|\hat{r}_n|$ gradually decreases until $n \sim 45$ and then increases indicating contributions from higher modes (noise) are greater than those from lower modes.

expect the transition from the visco-capillary phase to the elasto-capillary regime to scale with λ. However, the transition from the initial viscous phase to the middle elastic period also shifts to earlier times as De increases when time is scaled by λ. This indicates the cross-over time from the visco-capillary regime to the elasto-capillary regime is a function of multiple parameters including λ.

The blue lines in figure 3.3b represent the rate of exponential thinning predicted by the original theory (Entov & Hinch 1997) in the elasto-capillary regime. The 1D model results for the midfilament evolution during the elasto-capillary regime agree reasonably well with the evolution predicted by (3.11) for the larger De shown here. However, it is unclear from the 1D model results for $De = 1$ if the elasto-capillary regime has been reached. Therefore we cannot definitively validate (or invalidate) the original theory's applicability to the elasto-capillary regime for smaller De.

We now turn our attention to characterizing the early viscous regime. The differential Newtonian analysis (2.7) scaled by R_p, σ and t_c is

$$\alpha^* = 1 = 6\left(Oh\frac{(3R_tR_{zz} - RR_{zzt})}{\kappa_{zz}R^2} - \frac{(3R_t^2 - RR_{tt})}{3\kappa_{zz}R^2}\right), \text{ at } R_z = 0. \tag{3.16}$$

The results for α^* determined by (3.16) applied to the early viscous regime are shown in figure 3.4 for viscous viscoelastic filaments ($Oh = 3.16, S = 0.25$) with $0 \leq De \leq 100$. The differential method predicts $\alpha^* = 1$ in the Newtonian limit ($De \to 0$), as expected, and indicates μ_0 is accurately characterized. Values of α^* determined by (3.16) for $De > 0$ are generally overpredicted and deviations increase with De. The differential method results for α^* increase sharply from an initial value of $\alpha^* = 1$ for $De > 0$. The results for $De = 1$ and $De = 10$ then decline rapidly, become relatively constant for a brief period and then decrease sharply again. In contrast, α^* for $De = 100$ decreases gradually before a final rapid decline. Values of α^* determined by (3.16) for $De > 0$ fall below zero (giving unphysical results)

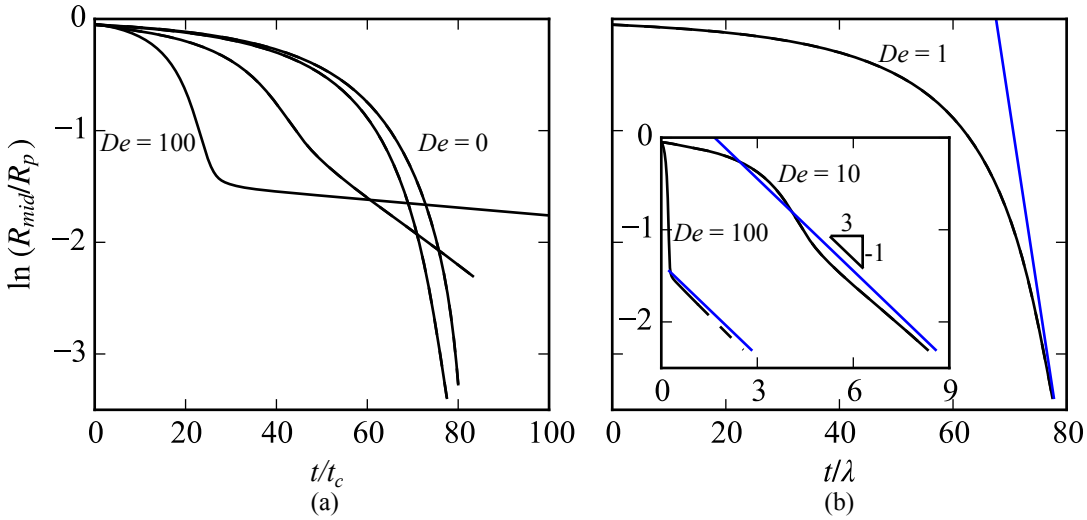

Figure 3.3: Dimensionless filament midpoint evolution R/R_p for $Oh = 3.16, S = 0.25$ and $De = 0, 1, 10$, and 100 as a function of time scaled by (a) an inertio-capillary time t/t_c; and (b) the polymer relaxation time t/λ. The results are shown in a semilogarithmic plot. The blue lines in (b) represent the exponential decay rate predicted by the original viscoelastic CBR analysis (3.11) (Entov & Hinch 1997). The early viscous phase corresponds to the region crudely described as an "inverted" parabola. The middle elastic phase is identified by the region of exponential thinning that appears as a linearly decreasing function in the semilogarithmic frame. An exponentially decaying filament is not observed in the Newtonian limit ($De \to 0$).

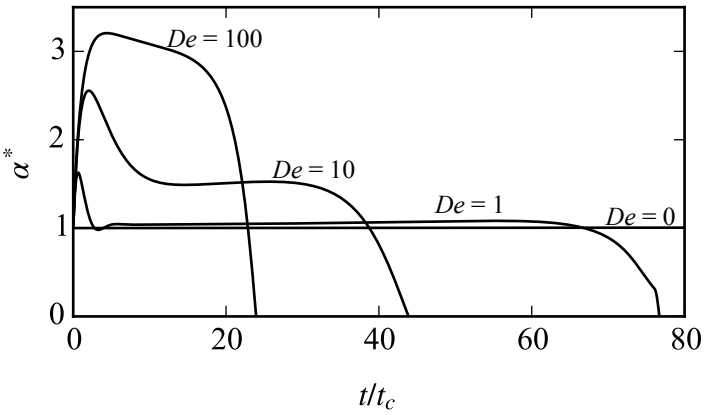

Figure 3.4: Dimensionless surface tension to viscosity ratios α^* determined by the differential method (3.16) for $Oh = 3.16, S = 0.25$ and $De = 0, 1, 10$, and 100 plotted with dimensionless time t/t_c. The time period shown here corresponds to the initial viscous regime.

near the end of the initial viscous phase as shown by comparing figures 3.3a and 3.4. The end of the visco-capillary phase for $De = 1$ is easier to identify by $\alpha^* < 0$ in figure 3.4 since the region of exponential thinning is difficult to distinguish for the corresponding curve in 3.3a.

Figure 3.5 shows the dimensionless capillary, viscous solvent, and elastic terms in the midfilament force balance (3.8) plotted with t/t_c for $Oh = 3.16, S = 0.25$ and $0 \leq De \leq 100$. The capillary terms are initially the largest terms. The temporal evolutions of the capillary terms resemble the corresponding results for R/R_p in figure 3.3a because the largest contribution to the capillary term in (3.8) is R. The viscous solvent terms generally increase rapidly from zero at very early times and then grow more modestly to a peak value. The maximum values of the viscous solvent terms shift to earlier times and larger values with increasing De. The elastic terms also increase from zero but their initial growth lags behind the corresponding viscous solvent terms. The initial growth rates for the elastic terms also becomes smaller as De increases. Peak values for the elastic terms also increase and shift to earlier times as De increases. Maximum values for the viscous solvent terms occur slightly earlier

than the peak values for the corresponding elastic terms when $De > 0$.

The evolutions of the elastic terms for $De \leq 1$ are qualitatively similar to the corresponding viscous solvent terms because the viscous contribution from the polymer is stronger than its non-Newtonian contribution near or in the Newtonian limit $De \to 0$. The elastic terms are larger than the viscous solvent contributions for small De because $S = 0.25$ indicating the viscous polymer contribution to μ_0 is larger than the solvent contribution. For small De, capillary terms remain larger than the viscous solvent and elastic terms throughout the evolution shown.

The temporal behavior of the viscous solvent and elastic terms becoming increasing dissimilar with increasing De. The elastic contribution increases with De such that it exceeds the capillary term at intermediate times in the period shown when $De = 100$. Additionally, the elastic terms decay at the same rate as R/R_p and the capillary terms at larger De.

The behavior of the differential method results for α^* in figure 3.4 for $De > 0$ may be explained by the evolution of the individual terms in the midfilament force balance (3.8). The early "bump" observed in values of α^* (3.16), especially distinct for $De = 1$ and $De = 10$, is related to the lag in growth between the viscous solvent and elastic terms. Following the initial overshoot, values of α^* for $De > 0$ plateau when the elastic terms grow at a relatively constant rate. Finally, the sharp decrease in the differential method results leading to unphysical values of α^* occurs when the viscous solvent terms decay and are exceeded by the growing elastic terms. At longer times, capillary and elastic terms dominate in the midfilament force balance (3.8).

Figure 3.6 compares $R(z)$ for $De = 0$ and $De = 100$ at specific times corresponding to features in the differential method results for α^* and the force terms for $De = 100$ (figures 3.4 and 3.5, respectively). The filament profiles for $De = 0$ when $t/t_c \leq 31$ qualitatively resemble hourglasses with increasingly pronounced waists as time progresses. The filament profile near the midpoint begins to flatten out at longer times

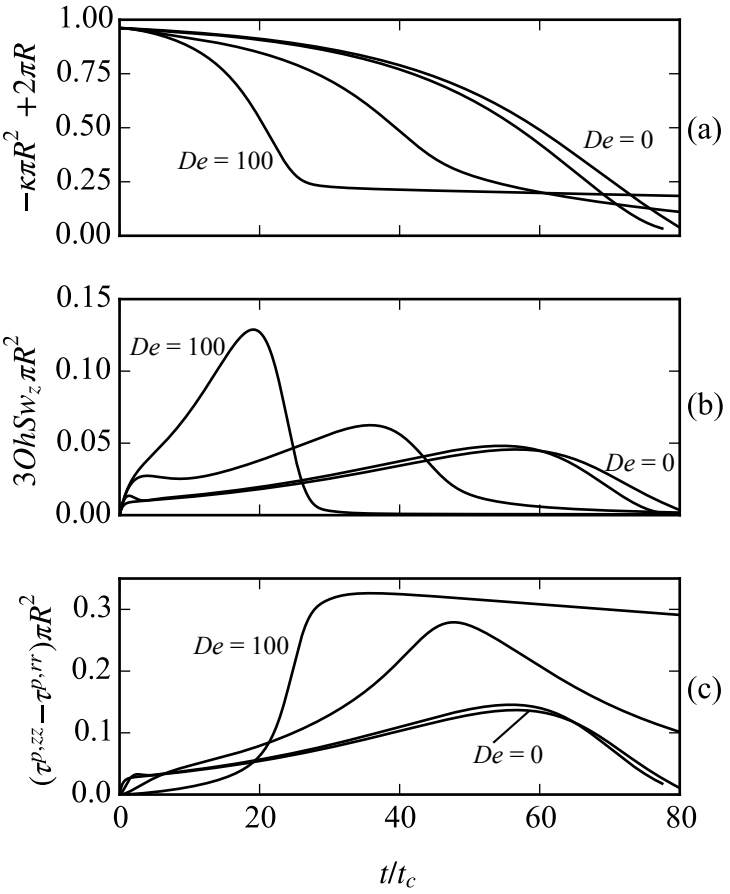

Figure 3.5: Evolutions of dimensionless (a) capillary $-\kappa\pi R^2 + 2\pi R$; (b) viscous solvent $3OhSw_z\pi R^2$; and (c) elastic $(\tau^{p,zz} - \tau^{p,rr})\pi R^2$ terms in the mid-filament force balance (3.8) as functions of dimensionless time t/t_c for $Oh = 3.16, S = 0.25$ and $De = 0, 1, 10$, and 100.

$(t/t_c = 80)$. The filament profiles for $De = 100$ also initially resemble hourglasses. However, as the elastic term grows and the viscous solvent term decays significantly at the end of the visco-capillary phase, axial variations in $R(z)$ between the reservoirs decay rapidly. Although not shown, values of α^* for $De > 0$ approach zero during the middle elastic regime because of decreasing axial variations in $R(z)$ due to elasticity. In particular, the dominant terms in the numerator and denominator in (3.16) are R_{zz} and R_{zzzz} (contained in κ_{zz}), respectively. As the free surface profile become increasingly flat with time, R_{zz} decays faster than R_{zzzz}.

We also evaluate the impact of S on the differential method (3.16) for charac-

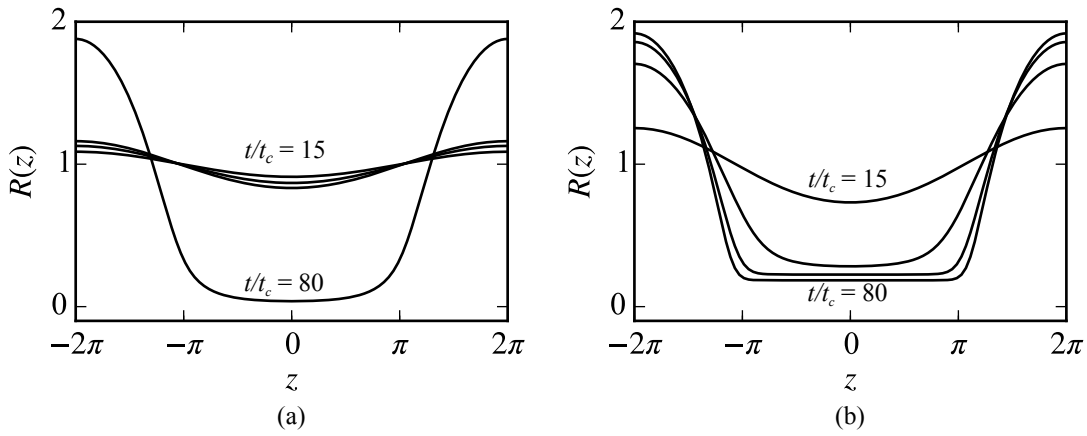

Figure 3.6: Dimensionless filament free surface profiles $R(z)$ predicted by the 1D viscoelastic model (3.12) for $Oh = 3.16, S = 0.25$ and (a) $De = 0$ (a Newtonian limit with $\mu = \mu_0$); and (b) $De = 100$. Profiles are shown for $t/t_c = 15, 25, 31$, and 80. These specific profiles are selected to match key features in the results for α^* and the stresses shown in figure 3.5. The initial filament evolution for $De = 0$ is slow compared to the evolution for $De = 100$.

terizing the early viscous regime. Figure 3.7a presents the filament midpoint evolution plotted with t/t_c in a semilogarithmic frame for evolving viscoelastic filaments ($Oh = 3.16, De = 94.9$) with $0 \leq S \leq 1$ predicted by the 1D model (3.12). The transition between the initial viscous phase and middle elastic regime shifts to earlier times as the viscous solvent contribution decreases (decreasing S). This is similar to the trend observed in figure 3.3 for increasing De and confirms the transition time between the initial viscous and middle elastic regimes is not a simple function of λ. Unlike the results for varying De, the cross-over between the two phases occurs at larger values of R/R_p at the filament waist as S decreases. This is likely because the filament evolution (deformation) driven by capillarity is less hindered as the viscous solvent contribution diminishes and thus enables elastic stresses to grow faster. This trend in S is consistent with Wagner *et al.* (2015). Additionally, the filament midpoints all decay at a similar exponential rate for $0 < S < 1$, as expected since De is fixed. The midfilament evolution for $S = 1$ does not exhibit a period of exponential decay but resembles the evolution seen in the Newtonian limit $De \to 0$ (figure 3.3).

The result for $S = 0$ is limited to a short period of time because of challenges with our numerical methods as described in the previous section.

The results for α^* determined by (3.16) applied to the visco-capillary regime for $0 \leq S \leq 1$ are shown in figure 3.7b. The differential method (3.16) accurately predicts $\alpha^* = 1$ for $S = 1$, indicating that $\tau_{ij}^p = 0$ is a solution to (3.12c-d) when there is no viscous polymer contribution ($\mu_p = 0$). This result also indicates $S \to 1$ is another Newtonian limit of the 1D viscoelastic model (3.12) and therefore the filament midpoint is not expected to decay exponentially. The case when $S \to 1$ corresponds to a Newtonian fluid with a shear viscosity $\mu = \mu_s$. The results determined by (3.16) for $S < 1$ deviate rapidly from an initial (and expected) value $\alpha^* = 1$. The deviations increase with decreasing S. Following a rapid rise, values of α^* for $0 < S < 1$ are relatively constant before a sharp decline leading to $\alpha^* < 0$. A region of relatively constant α^* is not observed in the result for $S = 0$; instead, the initial rise in α^* is followed by a rapid decrease.

Figure 3.8 shows the evolution of the dimensionless capillary, viscous solvent, and elastic terms in the local force balance at the fluid midpoint (3.8) throughout the initial viscous regime and into the elasto-capillary phase for $Oh = 3.16, De = 100$ and $0 \leq S \leq 1$. Like the results for variable De (figure 3.5), the capillary terms generally resemble the corresponding midfilament evolutions shown in figure 3.7a and are the largest terms throughout the initial viscous regime. The viscous solvent terms for $S > 0$ exhibit rapid growth at early times before transitioning to a modest growth rate. The initial (large) growth rate in the viscous solvent terms decreases as the viscous polymer contribution grows (decreasing S). Like the varying De results (figure 3.5), the peak values of the viscous solvent terms also shift to earlier times as the polymer contribution increases. A delay between the initial growth in the viscous solvent terms and the corresponding elastic terms is observed for $0 < S < 1$. The initial growth rate in the elastic terms decreases as S increases. The elastic contributions

for $S = 0.75$ and $S = 0.95$ in figure 3.8c do not show a clear maximum due to the limited time period shown. However the growth rates for these two cases decreases near the end of the period considered and suggests the elastic terms are approaching local maximums. The overall growth in the elastic terms decrease with growing S. Maximum values of the viscous solvent terms also occur before the corresponding elastic terms approach their peak values.

Figure 3.8 confirms $\tau_{ij}^{p} = 0$ when $S \to 1$. Additionally, the viscous solvent and capillary terms resemble the corresponding results in the Newtonian limit $De \to 0$ (figure 3.4). Therefore, the differential method (3.16) accurately determines α^* for $S \to 1$. The initial deviations from the expected value $\alpha^* = 1$ for $S < 1$ are also related to the delay in growth between the viscous solvent and elastic contributions. The subsequent plateau in α^* for $0 < S < 1$ is due to relatively constant growth in the elastic terms. For $S = 0$ there is no viscous solvent contribution and no relatively constant growth rate is observed in the early evolution of the elastic contributions. Therefore, deviations from the expected value α^* are related to the onset of non-linear elastic effects before the initial unsteady effects in the polymer contribution decay. The rapid decrease in the differential method results leading to $\alpha^* < 0$ is generally related to the decay in the viscous solvent terms and growth of the elastic contributions resulting in the balance of elastic and capillary terms at longer times.

3.3.5 Characterizing the early viscous regime – low-viscosity (small Oh)

We also evaluate the accuracy of the differential analysis (3.16) in the initial phase of filament evolution for low-viscosity viscoelastic fluids. We consider values of De, S and Oh representative of healthy saliva. As in the previous section, we investigate the impact of De and S on the accuracy of (3.16) in the low Oh regime. Our simulations for $Oh = 0.002, 0 \leq De \leq 100$ and $0 \leq S \leq 1$ are limited to a short initial period because the numerical simulations in this parameter space break down when R/R_p

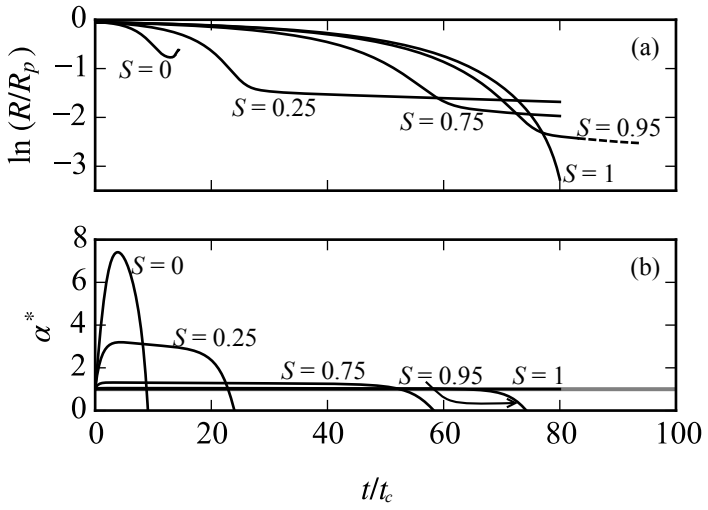

Figure 3.7: Dimensionless (a) midfilament evolution R/R_p; and (b) differential method results for α^* (3.16) for $S = 0, 0.25, 0.75, 0.95$ and 1 ($Oh = 3.16, De = 94.9$). The results are plotted as a function of dimensionless time t/t_c throughout the initial viscous phase.

at the waist is approximately half its initial value. Increasing the spatial and/or temporal resolution do not delay the numerical instabilities to later times. Since we are primarily interested in evaluating the performance of the differential analysis (3.16) in the initial period, we proceed to analyze the results generated by the 1D model (3.12) before our numerical scheme breaks down.

The 1D model results for $Oh = 0.002, S = 0.98$ and $0 \leq De \leq 100$ are summarized in figure 3.9 where the filament midpoint evolutions R/R_p and results for α^* determined by (3.16) are plotted with dimensionless time t/t_c. The predicted curves for R/R_p and α^* are indistinguishable indicating the filament dynamics in the low Oh regime are independent of the De range considered here. The curves for R/R_p in figure 3.9a are qualitatively similar to those observed during the early viscous regime for larger Oh (figure 3.3). However, the filament midpoints decay faster at low Oh ($R/R_p = 0.55$ for low Oh and $R/R_p = 0.85$ for $Oh = 3.16, S = 0.25, De = 100$ at $t/t_c = 10$). The filament midpoint evolutions for low Oh appear to slow near the end of the period shown, resembling the transition to the elasto-capillary regime for

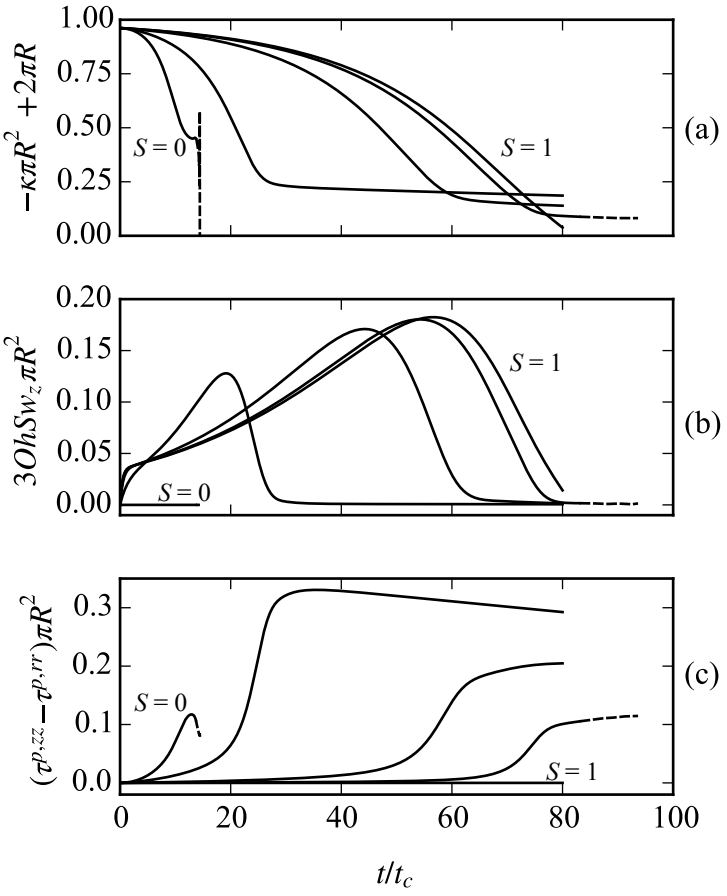

Figure 3.8: Evolutions of dimensionless (a) capillary $-\kappa\pi R^2 + 2\pi R$; (b) viscous solvent $3OhSw_z\pi R^2$; and (c) elastic $(\tau^{p,zz} - \tau^{p,rr})\pi R^2$ terms in the mid-filament force balance (3.8) as functions of dimensionless time t/t_c for $Oh = 3.16, De = 100$ and $S = 0, 0.25, 0.75, 0.95$ and 1. Dashed lines near the end of the results for $S = 0$ and $S = 0.95$ indicate regions when our implicit Euler-Chebyshev numerical scheme is beginning to fail. The elastic contribution is zero in the Newtonian limit $S \to 1$. The viscous solvent term is zero for $S = 0$.

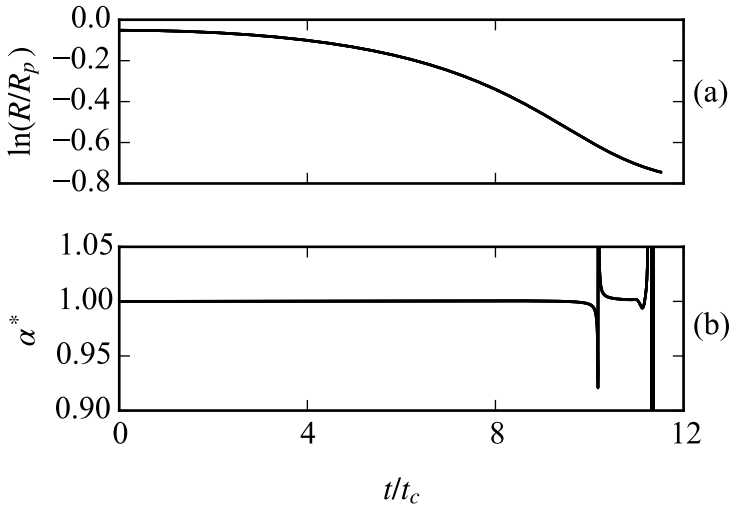

Figure 3.9: Dimensionless (a) midfilament evolution R/R_p; and (b) differential method results for α^* (3.16) for $Oh = 0.002, S = 0.98$ and $De = 0, 1, 10,$ and 100. The results are plotted as a function of dimensionless time t/t_c. The results for varying De are indistinguishable from the Newtonian limit $De \to 0$.

$De > 0$ and high Oh. However, since this result is independent of De, this transition is most likely due to inertial effects in this nearly inviscid regime.

The differential method results in figure 3.9b deviate from $\alpha^* = 1$ by less than 0.1% before a singularity occurs around $t/t_c = 10$. Values of α^* determined by (3.16) are also accurately predicted to within 0.1% between discontinuities.

Figure 3.10 shows the dimensionless time-varying capillary, viscous solvent, and elastic terms in the local force balance at the filament waist (3.8) for $Oh = 0.002, S = 0.98$ and $0 \leq De \leq 100$. The capillary and viscous solvent terms for all De are indistinguishable. The effects of De are only discernible in the results for the elastic contributions. The early growth rate in the elastic terms generally follows the same trend of decreasing with increasing De as observed for high-viscosity filaments (figure 3.5). However, elastic terms in addition to viscous solvent terms are relatively insignificant compared with the capillary contributions throughout the period shown.

The cause for the discontinuities observed in α^* is related to the temporal evolu-

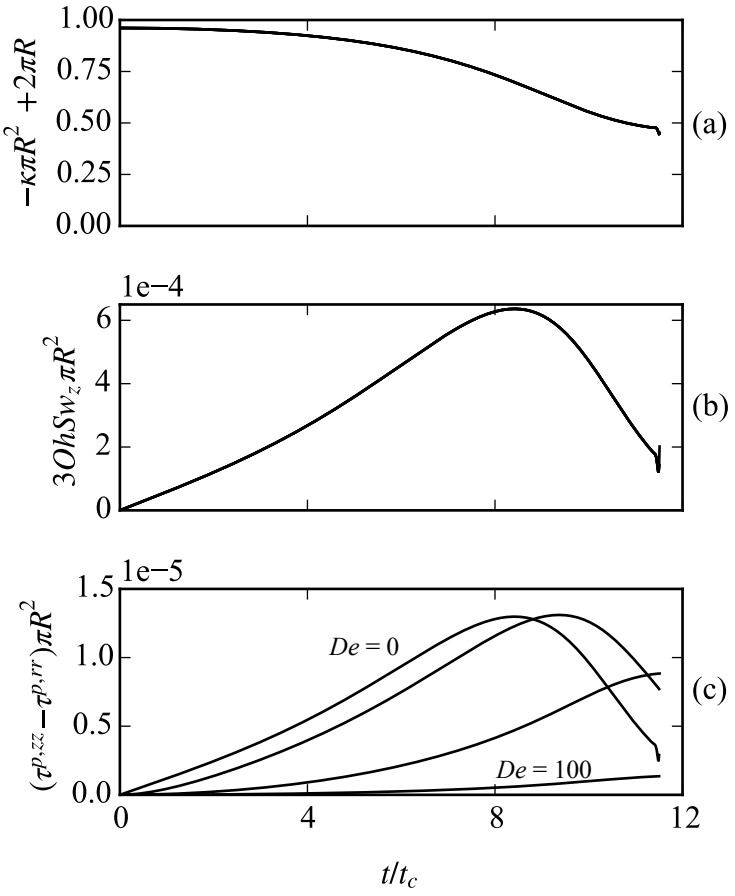

Figure 3.10: Evolutions of dimensionless (a) capillary $-\kappa\pi R^2 + 2\pi R$; (b) viscous solvent $3OhSw_z\pi R^2$; and (c) elastic $(\tau^{p,zz} - \tau^{p,rr})\pi R^2$ terms in the mid-filament force balance (3.8) as functions of dimensionless time t/t_c for $Oh = 0.002, S = 0.98$ and $De = 0, 1, 10$, and 100. Capillary and viscous solvent contributions are relatively insensitive to changes in De. The effect of varying De is only obvious in the relatively small elastic contributions.

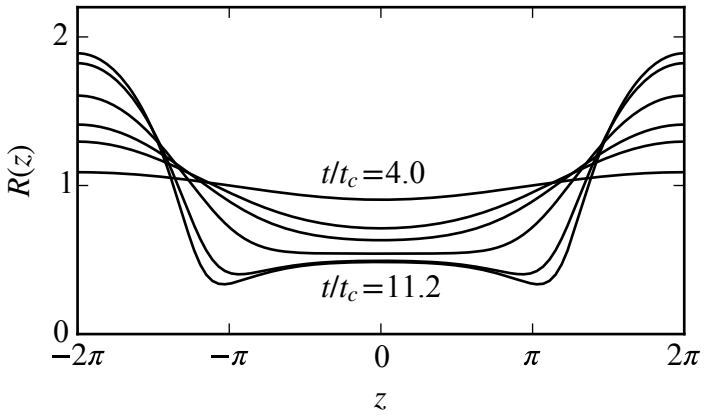

Figure 3.11: Dimensionless filament free surface profiles $R(z)$ for $Oh = 0.002, S = 0.98$, and $De = 0$ at $t/t_c = 4, 8, 9, 10.2, 11$, and 11.2 corresponding to features in the differential method results for α^* shown in figure 3.9.

tion of $R(z)$ and consequently κ_{zz} at the midpoint. Figure 3.11 shows $R(z)$ for the Newtonian limit ($De \to 0$) at several times throughout the evolution. The shape of the filament free surface for $t/t_c < 9$ qualitatively resembles an hourglass with an increasingly pronounced waist as t/t_c increases. For $t/t_c \geq 9$, the filament waist becomes less distinct as $R(z)$ near the midpoint begins to flatten out. By $t/t_c = 10.2$, $R(z)$ may essentially be represented as a straight line from $-\pi/2 < z < \pi/2$ and thus $\kappa_{zz} = 0$. The value of κ_{zz} changes sign due to the formation of a large bead in the filament at $t/t_c > 11$. The bead develops due to two pinch points forming near the reservoirs. The bead becomes more distinct as R at the pinch points continues to decrease. The filament midpoint also decreases (also seen figure 3.9a) as the bead becomes more pronounced. This is different from bead formation due to growth at the midpoint for more viscous viscoelastic fluids (see figure 3 in Bhat *et al.* (2010) and figure 3.1a).

Figure 3.12 presents the 1D model results for $Oh = 0.002, De = 100$, and $0 \leq S \leq 1$. The results for the midfilament evolution and values of α^* determined by (3.16) are very similar to the results for varying De (figure 3.9). The 1D model for low Oh shows slightly more sensitivity to varying S (compared to variable De), best seen by

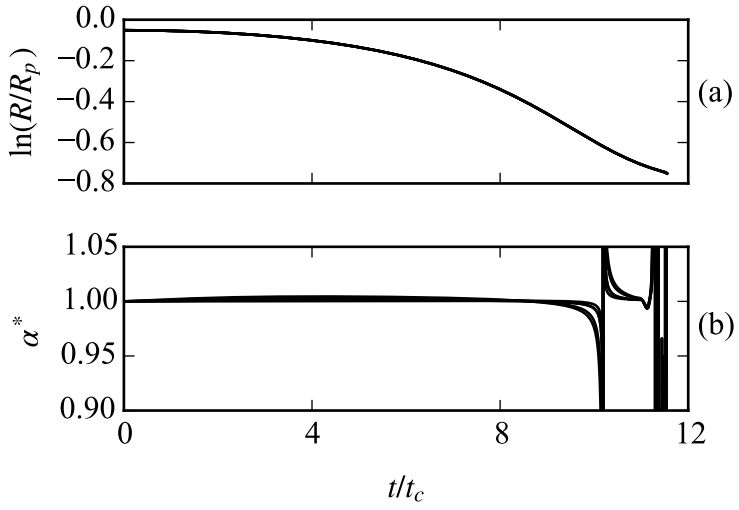

Figure 3.12: Dimensionless (a) midfilament evolution R/R_p; and (b) differential method results for α^* (3.16) for $Oh = 0.002, De = 100$ and $S = 0, 0.25, 0.75, 0.98$, and 1. The results are plotted as a function of dimensionless time t/t_c. The results for varying S are generally indistinguishable from the Newtonian limit $S \to 1$.

the separation of the differential method results for α^* just before $t/t_c = 10$. Like the variable De results, values of α^* determined by (3.16) for $0 \leq S \leq 1$ deviate from the expected value $\alpha^* = 1$ by less than 0.1% for $t/t_c < 9$ and after the discontinuity around $t/t_c = 10$. Deviations from unity are smallest for $S \to 1$ (a Newtonian limit). The discontinuity also occurs due to the formation of a bead (from pinching near the reservoirs).

The dimensionless time-varying capillary, viscous solvent, and elastic terms in the midfilament force balance (3.8) for $Oh = 0.002, De = 100$ and $0 \leq S \leq 1$ are shown in figure 3.13. The spike in the results at the end of the period shown is related to the failure of our numerical scheme. The capillary terms remain the largest contribution of the three terms considered. Variations in S are not discernible in the capillary contributions but more obvious in the viscous solvent and elastic terms. Unlike the results for high Oh (figure 3.8), peak values in the viscous solvent terms do not shift to earlier times as S decreases. However, the overall viscous solvent and

elastic contributions do decrease and increase, respectively, as the viscous polymer contribution increases (decreasing S). These are consistent with the trends observed for high Oh. Even still, the viscous solvent and elastic contributions remain relatively inconsequential compared with the capillary terms.

3.3.6 Discussion

We investigate the impact of viscoelasticity in high- and low-viscosity filament dynamics with a single-mode 1D Oldroyd-B model to evaluate the performance of our 1D differential analysis (2.7) during the early viscous phase of non-Newtonian filament evolution. Figures 3.4, 3.7b, 3.9b and 3.12b show the differential method (3.16) accurately predicts $\alpha^* = 1$, and therefore μ_0, in the Newtonian limits of the 1D viscoelastic model (3.12), $De \to 0$ or $S \to 1$. Furthermore, the differential method (3.16) initially predicts $\alpha^* = 1$ for $De > 0$ and $S < 1$ indicating that μ_0 is accurately characterized in the limit of small deformations, another Newtonian limit.

The filament dynamics and consequently the differential method results for α^* are sensitive to variations in the polymer relaxation time (De) and viscous polymer contribution (S) for high-viscosity viscoelastic filaments (figures 3.3, 3.4, and 3.7). In particular, deviations from the expected value $\alpha^* = 1$ grow with increasing viscoelastic effects such as increasing De and decreasing S. The deviations in α^* from unity for $De > 0$ and $S < 1$ are related to the initial elastic contribution relative to the viscous solvent contribution. At early times in the viscous regime for $De > 0$ or $S < 1$, the viscous solvent terms grow faster than the elastic terms and lead to overpredicted values of α^* determined by (3.16). The initial elastic growth rate decreases with increasing De and thus the early plateaus in the differential method results shift slightly to later times when De increases. In comparison, the initial elastic growth rate increases as S declines and therefore shifts the start of the plateau to earlier times as viscous polymer contributions increase. For both De and S, values of α^*

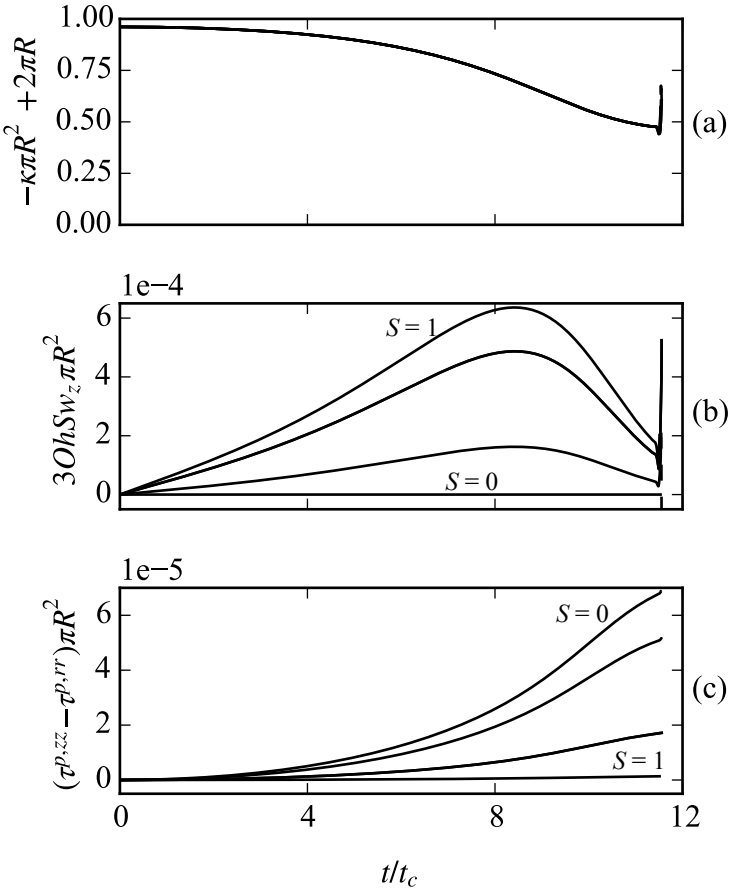

Figure 3.13: Evolutions of dimensionless (a) capillary $-\kappa\pi R^2 + 2\pi R$; (b) viscous solvent $3OhSw_z\pi R^2$; and (c) elastic $(\tau^{p,zz} - \tau^{p,rr})\pi R^2$ terms in the mid-filament force balance (3.8) as functions of dimensionless time t/t_c for $Oh = 0.002$, $De = 100$ and $S = 0, 0.25, 0.75, 0.98$ and 1. Capillary terms are relatively insensitive to changes in S. Viscous solvent terms grow and elastic terms decrease with increasing S. However, both viscous solvent and elastic terms are negligible compared with capillary terms.

determined by (3.16) are relatively constant when the elastic terms grow at a relatively steady rate after the initial unsteady effects decay. The differential method results decline sharply and become unphysical once the viscous solvent terms decay and the elastic terms grow to balance the capillary terms. Although the differential method results for varying De and S are similar, the effect of De is distinguishable by a sharp rise and decline in α^* observed at early times during the visco-capillary phase, particularly for smaller De.

The same trends in the capillary, viscous solvent, and elastic terms are generally observed in the low-viscosity results (figures 3.10 and 3.13) when De and S are varied. However, the viscous solvent and elastic contributions are relatively insignificant compared to the capillary term in this nearly inviscid regime. Therefore, the filament dynamics and differential method results for α^* are also relatively insensitive to De and S (figures 3.9 and 3.12). Values of α^* (3.16) are accurately predicted to within 0.1%, implying μ_0 is accurately characterized even after the formation of a bead at later times. However, this also implies no information regarding the viscoelastic nature (or lack thereof) of the filament may be discerned from the differential method (3.16) applied to the early viscous phase for nearly inviscid fluids.

Viscosity, the polymer relaxation time, and the viscous polymer contribution (Oh, De, and S, respectively) all affect the filament dynamics, specifically the initial growth in the elastic terms. Hence, α^* determined by the differential analysis (3.16) during the early viscous phase cannot be expected to scale according to a single parameter. Therefore, no universal curve for α^* is expected and a family of curves is beyond the scope of this study.

3.4 Conclusions

Saliva's non-Newtonian behavior is attributed to its surface active and protein content. Therefore we have investigated the role of surfactants and viscoelasticity

in 1D filament dynamics to evaluate the performance of the 1D differential method developed in chapter II for characterizing non-Newtonian fluids. Our simple experiments with a soap-and-water mixture indicate surfactants do not significantly improve filament forming capabilities in low-viscosity fluids like saliva. Saliva's surface active components do contribute to biofilms that perform protective functions in the oral cavity. However, the surface rheology of saliva is beyond the scope of this work.

We have studied 1D high- and low-viscosity viscoelastic filament dynamics with a 1D Oldroyd-B model and the typical problem formulation for the development of CBR analyses. Specifically, we have assumed a long, unstable fluid filament with zero initial polymer stresses. We apply the 1D differential analysis (3.16) to the early viscous regime predicted by the 1D model (3.12) because the established method for determining the polymer relaxation time (3.11) works well.

The differential method results suggest additional material parameters beyond the commonly characterized polymer relaxation time may be measured from the early evolution of a viscoelastic filament. Our results show the differential method accurately characterizes μ_0 in the Newtonian limits of the 1D model (3.12) ($De \to 0, S \to 1$, and small deformations) for high- and low-viscosity filaments.

Values of α^* determined by (3.16) are overpredicted when $De > 0$ and $S < 1$ for high-viscosity viscoelastic filaments. The deviations are related to slow and unsteady initial growth in the elastic contribution at early times in the viscous phase. The differential method results when $De > 0$ and $S < 1$ plateau at a value $\alpha^* > 1$ when relatively constant growth in the elastic contributions is observed. The value of α^* during the plateau is sensitive to variations in De and S and may be useful for characterizing the individual parameters.

The relationships between the initial elastic behavior with De and S are also generally true for low-viscosity filaments. However, the elastic and viscous solvent contributions for the low Oh cases considered here are 3-4 orders of magnitude smaller than

the capillary contributions. Therefore, the filament dynamics at $Oh = 0.002, De > 0$ and $S < 1$ are not distinguishable from a nearly inviscid Newtonian fluid. Hence, the differential method results are also insensitive to non-zero viscoelastic effects.

We recommend characterizing μ_0 from the differential methods results for α^* at the start of the filament evolution when deformations are small. Furthermore, the sensitivity of the differential method results to Oh, De, and S, suggests the effects of De and S may be distinguishable, particularly for high-viscosity filaments. Therefore, future work should map the performance of the differential method (3.16) within the $Oh-De-S$ space to facilitate multiple parameter characterizations from the evolution of a viscoelastic filament during the early viscous phase.

It is important to re-emphasize the viscoelastic filament dynamics studied here are based on slender filaments with zero initial polymer stresses. This assumptions simplifies the 1D viscoelastic analysis, enabling trends in the filament evolution caused by varying viscoelastic parameters to be determined. However, this assumption may not accurately represent physical viscoelastic filaments after an imposed deformation. Therefore we investigate viscoelastic filament dynamics during deformation in the next chapter.

CHAPTER IV

Expanding the CBR Method

4.1 Introduction

The 1D CBR analyses presented by Entov & Hinch (1997) and in the previous two chapters are based on long, slender fluid filaments where the initial stresses are assumed to be negligible. This assumption does not affect Newtonian fluids where the material properties are independent of the deformation history, although the filament shape at the end of stretch (start of conventional CBR measurement) depends on the deformation history as capillarity acts before the stretching is finished. However, the assumption of zero stresses at the end of the stretching process is problematic for non-Newtonian filaments where the extra stress is nonlinearly related to the strain-rate. Anna & McKinley (2001) shows non-zero initial conditions for the polymer stresses at the start of the conventional CBR measurement regime is important for accurately modeling the midfilament evolution of a viscoelastic fluid. Additionally, the numerical and experimental results in Anna & McKinley (2001) show the polymer stresses may become significant during the initial deformation such that the early viscous dominated phase is past before the plates come to rest. The initial viscous phase is therefore not observed during the standard CBR measurement regime and thus difficult to characterize.

In our preliminary CBR experiments with saliva, we observe the presence (or

absence) of an initial viscous regime after stretching is affected by small variations in the imposed deformation. Figure 4.1 shows saliva midfilament evolutions for two different imposed strains, $L_f/L_0 = 2.66$ and $L_f/L_0 = 2.33$, in a semilogarithmic frame. Results are shown for the typical CBR measurement regime where $t = 0$ corresponds to the end of stretch and therefore $\ln(R/R_p)$ is initially non-zero. Prior to the stretching process, each saliva sample is constrained between two circular plates (radius $R_p = 1$ mm) separated by a small gap $L_0 = 0.75$ to form a squat cylinder with an initial aspect ratio $\Lambda_0 = L_0/R_p$. Each strain is imposed in 0.25 s. An initial region of rapid decay characteristic of the early viscous regime is absent in the saliva midfilament evolution for the larger strain $L_f/L_0 = 2.66$. This may be due to the limited recording rate of the imaging set-up (60 frames/s). However, the exponential decay indicative of the elasto-capillary regime is observed for approximately 35 ms after the plates come to rest at $t = 0$. In contrast, a long viscous regime is observed for 107 s followed by a short phase of exponential decay (< 2 s) when the imposed strain is reduced to $L_f/L_0 = 2.33$. These preliminary results indicate the elastic stress growth (and thus the onset of the elastic phase) may be controlled by varying the imposed strain. Delaying the onset of the elastic phase will enable measurements during an early viscous regime. This may be particularly useful for facilitating multiple parameter characterization from a single sample and is therefore one way of expanding the measurement capabilities of the traditional CBR implementation.

In this chapter we investigate methods to extend the measurement range of traditional capillary break-up rheometry. In particular, we study 1D filament dynamics with a 1D Oldroyd-B model to evaluate the performance of the differential analysis (2.7) during the deformation process. We consider cases when the fluid sample is initially at rest and therefore zero polymer stresses are an appropriate initial condition. We first consider a deformation history similar to the approximate step-strain imposed in conventional CBR set-ups. We also model the filament dynamics due to

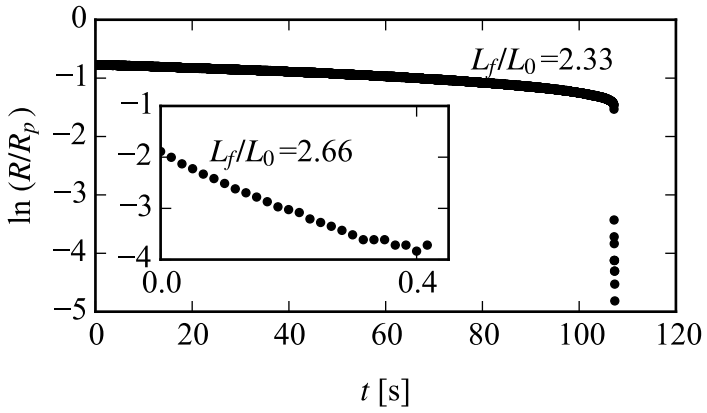

Figure 4.1: Dimensionless filament midpoint evolutions R/R_p for saliva filaments after imposed strains of $L_f/L_0 = 2.33$ and $L_f/L_0 = 2.66$ (inset). The results are shown as a function of dimensional time t in a semilogarithmic plot. An initial viscous regime is difficult to observe from the midfilament evolution for $L_f/L_0 = 2.66$, however, the following middle elastic regime is easily identified by the exponential decay in R/R_p for 35 ms. A significantly longer (107 s) initial viscous regime is observed when a smaller strain $L_f/L_0 = 2.33$ is imposed. However, the period of exponential decay in R/R_p is shorter for $L_f/L_0 = 2.33$ (< 2 s) than $L_f/L_0 = 2.66$.

oscillating boundary motion to investigate a deformation profile that avoids filament break-up. Low-viscosity fluids ($\mu < 70$ mPa·s) are currently difficult to characterize with a standard CBR set-up because the filament ruptures before the plates come to rest (Rodd *et al.* 2005). Thus, a deformation history that avoids break-up would be advantageous for extending the viscosity range of traditional CBR.

4.2 1D Model and Simulation

We model various deformation histories imposed on a viscoelastic filament with a single-mode (single relaxation time) 1D Oldroyd-B constitutive model to evaluate the performance of the differential Newtonian analysis (2.7) in the early regime before the onset of elastic effects and finite extensibility. This is the same model considered in chapter III and also considered by Tembely *et al.* (2012) to model stretching for a weakly elastic low-viscosity fluid. The 1D model scaled by the plate radius R_p,

the surface tension σ and an inertio-capillary time $t_c = \sqrt{\rho R_p^3/\sigma}$ where ρ is the fluid density, are repeated here for convenience

$$(R^2)_t + (wR^2)_z = 0 \tag{4.1a}$$

$$(w_t + ww_z)R^2 = -\kappa_z R^2 + 3OhS(w_z R^2)_z + ((\tau^{p,zz} - \tau^{p,rr})R^2)_z \tag{4.1b}$$

$$\tau^{p,zz} + De(\tau_t^{p,zz} + w\tau_z^{p,zz} - 2w_z\tau^{p,zz}) = 2Oh(1-S)w_z \tag{4.1c}$$

$$\tau^{p,rr} + De(\tau_t^{p,rr} + w\tau_z^{p,rr} + w_z\tau^{p,rr}) = -Oh(1-S)w_z \tag{4.1d}$$

$$\kappa = \frac{1}{R(1+R_z^2)^{1/2}} - \frac{R_{zz}}{(1+R_z^2)^{3/2}}, \tag{4.1e}$$

where κ is twice the mean curvature of the filament free surface $R(z)$. The scaled 1D viscoelastic model (4.1) contains three dimensionless parameters, the Deborah number $De = \lambda/t_c$, the Ohnesorge number $Oh = \mu_0/\sqrt{\rho\sigma R_p}$, and $S = \mu_s/\mu_0$, to characterize the contributions of the polymer relaxation time λ, the solvent viscosity μ_s, and the polymer viscosity μ_p. We note here that another time scale, such as the average strain-rate or the stretching time t_s may be more appropriate for studying filament dynamics driven by plate motion.

The 1D viscoelastic model (4.1) is solved by a pseudospectral approach consisting of an implicit backward Euler temporal integration scheme and a Chebyshev spatial mesh also employed in chapter III. In addition, we implement the arbitrary Lagrangian-Eulerian (ALE) technique to model the time-dependent length $L(t/t_s)$ of the spatial domain. The ALE technique enables the spatial nodes to move with a velocity v_n proportional to the prescribed plate velocity $V_p(t/t_s)$. All partial derivatives in time are then expressed as $\frac{\partial}{\partial t} = \frac{d}{dt} - v_n\frac{\partial}{\partial z}$ (Donea *et al.* 1982; Vadillo *et al.* 2012).

The filament is initially a static cylinder spanning the axial domain $-L(0)/2 \leq z \leq L(0)/2$ and is described by $R(z,0) = 1$ and $w(z,0) = \tau^{p,zz}(z,0) = \tau^{p,rr}(z,0) = 0$. Unlike the 1D model considered in chapter III, the filament is pinned at the boundaries

such that $R(-L/2, t/t_s) = R(-L/2, t/t_s) = 1$. Dirchlet boundary conditions also apply to w such that $w(-L/2, t/t_s) = -V_p(t/t_s)$ and $w(-L/2, t/t_s) = V_p(t/t_s)$. The Chebyshev spatial scheme is particularly advantageous here for enforcing these non-periodic boundary conditions.

Determining the appropriate boundary conditions to impose on $\tau^{p,zz}$ and $\tau^{p,rr}$ remains a challenge for the 1D viscoelastic model (4.1). As discussed in chapter III, boundary conditions for $\tau^{p,zz}$ and $\tau^{p,rr}$ require knowledge of the fluid deformation history at all times. Therefore, we examine the various Newtonian limits of (4.1) where we understand the behavior of τ^p_{ij} to inform our choice of boundary conditions. The 1D viscoelastic model (4.1) contains several Newtonian limits: $S \to 1$ corresponding to a fluid with $\mu = \mu_s$, $De \to 0$ corresponding to a fluid with viscosity $\mu = \mu_s + \mu_p$, and small deformations. When the fluid is pinned ($R = 1$ at the boundaries), the no-slip condition requires $w_z = 0$ to satisfy the no-slip boundary condition and continuity (4.1a). For $De \to 0$ and small deformations, (4.1c-d) reduces to $\tau^{p,zz} = 2Oh(1-S)w_z$ and $\tau^{p,rr} = -Oh(1-S)w_z$ and therefore $\tau^{p,zz} = 0$ and $\tau^{p,rr} = 0$ should be applied at the boundaries to satisfy (4.1a). For $S \to 1$, $\tau^{p,zz} = 0$ and $\tau^{p,rr} = 0$ are solutions to (4.1c-d) (figures 3.8 and 3.12) and therefore naturally satisfy the no-slip condition and (4.1a). We seek a general approach to the boundary conditions for the polymer stresses rather than enforcing specific boundary conditions for individual limits of the 1D viscoelastic model (4.1). Fortunately, $w_z = 0$ is naturally satisfied at the plates. Therefore, we do not apply boundary conditions to the polymer stresses because $\tau^{p,zz} = 0$ and $\tau^{p,rr} = 0$ are also naturally satisfied at the plates and gives the correct solutions for all Newtonian limits of (4.1).

The procedure for solving the 1D model (4.1) at every time step is the same as described in section 3.3.3 with an additional step to determine the velocities at every node. A smaller dimensionless time step (typically $\Delta t = 0.0005$) is required to converge due to the transient boundary motion. However, the spatial mesh remains

the same as in chapter III ($N = 129$ nodes corresponding to $n = N$ modes). The spatial and temporal mesh are refined until changes in $R(z)$ are less than 0.5%.

As in chapter III, the quality of the results generated by our numerical scheme applied to (4.1) is monitored through the temporal evolution of $\hat{r}_n$, the Chebyshev coefficients for $R(z)$. In particular, we track the growth of $|\hat{r}_n|$ in time and with increasing n. The simulation is considered to be failing when $|\hat{r}_n|$ increases at large n.

We first model low-viscosity viscoelastic filament evolution driven by an approximate axial step-strain to compare the results determined by our numerical approach applied to (4.1) with the experimental and 1D model results presented in Tembely *et al.* (2012). Symmetry about the filament waist (where $R_z = 0$) is enforced by neglecting gravity and moving the top and bottom plates apart with equal but opposite piecewise continuous velocities given by

$$V_p\left(\frac{t}{t_s}\right) = \begin{cases} \frac{(L_f - L_0)}{2t_s}\left(1 - \cos\left(\frac{2\pi t}{t_s}\right)\right), & 0 < t/t_s < 1 \\ 0, & t/t_s > 1 \end{cases} \tag{4.2}$$

where t_s is the stretching time. Equation (4.2) corresponds to a piecewise continuous time-varying plate separation length (and thus the piecewise continuous time-varying length of the spatial domain) given by

$$L\left(\frac{t}{t_s}\right) = \begin{cases} \frac{(L_f - L_0)t}{t_s} - \frac{(L_f - L_0)}{2\pi}\sin\left(\frac{2\pi t}{t_s}\right) + L_0, & 0 < t/t_s < 1 \\ L_f, & t/t_s > 1 \end{cases} \tag{4.3}$$

where the initial and final plate separations are L_0 and L_f, respectively, resulting in an imposed strain L_f/L_0. The velocity profile (4.2) is qualitatively similar to the one used in Tembely *et al.* (2012) and is specifically constructed to gradually accelerate and decelerate at the beginning and end of the stretching process. Additionally, (4.3) is similar to the piston position profile modeled by a hyperbolic tangent function in

Tembely *et al.* (2012). The plate velocity and separation length profiles are shown in figure 4.2.

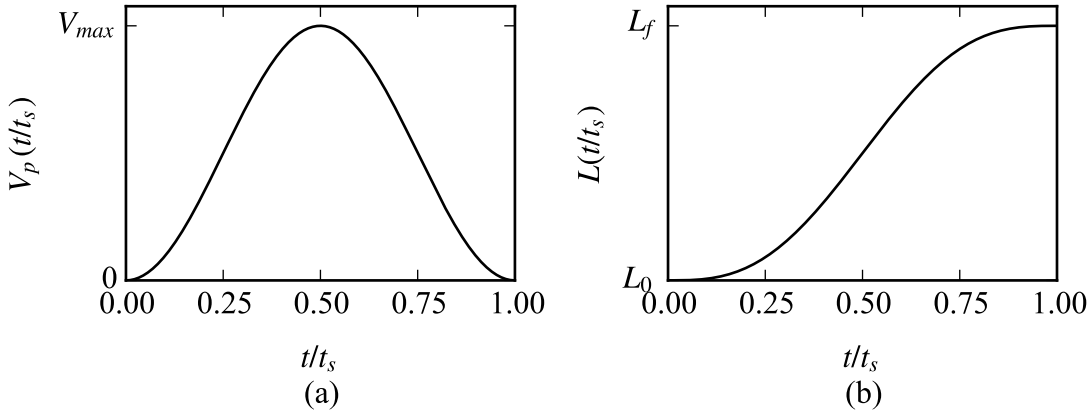

Figure 4.2: (a) Dimensionless velocity V_p (4.2) applied at the boundaries to model an approximate step-strain; and (b) the corresponding dimensionless spatial domain length L (4.3) plotted with dimensionless time t/t_s. The maximum velocity V_{max} is determined by the initial and final plate separations, L_0 and L_f, respectively, and the stretching time t_s

We model the same fluid investigated in Tembely *et al.* (2012), a weakly elastic low-viscosity solution of monodisperse polystyrene (PS110) at 2.5 weight percent dissolved in Newtonian diethyl phthalate (DEP). The dimensionless parameters for this fluid are $Oh = 0.2, De = 0.47$ and $S = 0.44$. We match the stretching time, initial aspect ratio, and imposed strain ($t_s = 5.4$ ms, $\Lambda_0 = 1$, $L_f/L_0 = 2.3$, respectively, where $R_p = 0.6$ mm) used in the experiments and 1D modeling in Tembely *et al.* (2012). We apply our piecewise continuous velocity profile (4.2) to the boundaries. Additionally, we consider two initial free surface profiles, $R(z,0) = 1$ and $R(z,0) = 1-\cos(\pi z/L_0)$, corresponding to an initially cylindrical fluid sample and a cylindrical sample with a 5% perturbation at the midpoint, respectively. The latter profile is similar to the nearly cylindrical fluid sample with a slighty concave profile prescribed in the experiments and 1D model in Tembely *et al.* (2012). It is important to note the exact initial condition for R prescribed by Tembely *et al.* (2012) is not given. It is also unclear if the velocity profile in Tembely *et al.* (2012), described by a hyperbolic

trigonometric function, is terminated at the cessation of stretch like our piecewise continuous description (4.2) or if the velocities are so small the plate movement is imperceptible for $t > t_s$. This may affect the 1D model results at longer times after stretch.

The dimensional midfilament diameter evolutions predicted by our implicit Euler-Chebyshev numerical scheme applied to the 1D Oldroyd-B model (4.1) for initially cylindrical and nearly cylindrical R profiles are shown in figure 4.3a. Dimensional results are shown to facilitate comparisons with experimental and 1D model results for the same fluid in Tembely *et al.* (2012) (figure 4.3b). The 1D Oldroyd-B model (4.1) in Tembely *et al.* (2012) is solved numerically by a commercial finite element package (COMSOL). The midfilament evolutions predicted by our numerical scheme applied to (4.1) are comparable to the experimental and 1D model results in Tembely *et al.* (2012) only during the stretching process. At the cessation of stretching, R/R_p for the initially cylindrical and nearly cylindrical R profiles are 6% larger and 7% smaller, respectively, than that observed experimentally and numerically in Tembely *et al.* (2012). These discrepancies are likely due to small differences between the initial conditions and prescribed boundary velocity profile. After the stretching process, the decays in R/R_p predicted by our numerical method applied to (4.1) for both initial conditions are significantly smaller than the experiments and 1D model results of Tembely *et al.* (2012), particularly for the initially cylindrical fluid sample. Large differences are observed between our 1D model results for each initial filament configuration after stretch. This suggests the 1D model (4.1) solved by our numerical approach is fairly sensitive to small changes in the initial condition. Additionally, when a nearly cylindrical initial condition for R is considered, like Tembely *et al.* (2012), our 1D model results for R/R_p decay faster and is more realistic. This indicates the initial condition must be carefully characterized to improve the accuracy of the 1D modeling. We note the 1D model results in Tembely *et al.* (2012) also

do not adequately match the experimental results after stretching and suggests a single-mode 1D Oldroyd-B model may not accurately describe the filament evolution at longer times after stretch.

The comparison with Tembely *et al.* (2012) suggest our numerical method applied to (4.1) correctly models the filament dynamics during the initial stretching process but breaks down at longer times. We observed similar difficulties in chapter III for the low Oh simulations. This is an indication that our numerical scheme is not robust for low Oh regimes, especially when elastic effects become important. This model break down is a matter of continuing research. Our preliminary efforts (not shown) indicate the prescribed boundary motion (and its piecewise nature) and imposed strains in addition to the initial conditions (figure 4.3a) may affect the accuracy of the 1D model (4.1) at longer times after stretch. Further investigations must also consider the challenges associated with the stress boundary conditions and may require modifications to our numerical approach.

We proceed to investigate viscoelastic filament evolution throughout the stretching process since we have shown our numerical scheme applied to (4.1) works well in this regime. We model the fluid dynamics driven by two different plate motions to evaluate the performance of our 1D differential analysis (2.7) during the deformation process.

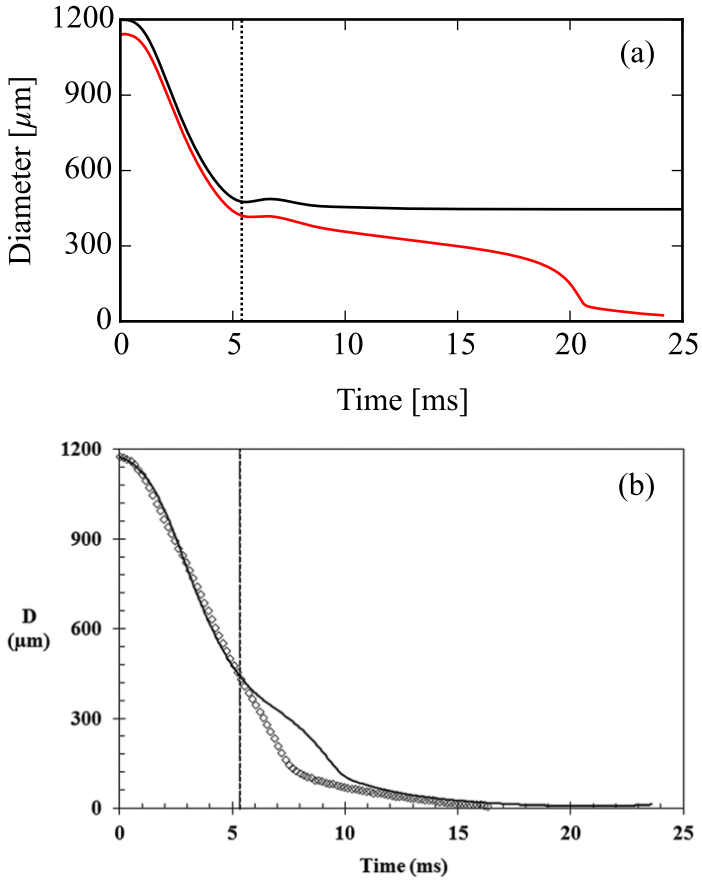

Figure 4.3: Dimensional midfilament diameter evolution during and after an approximate axial step-strain for a low-viscosity weakly elastic solution (2.5 wt.% PS110 in DEP, $Oh = 0.2, De = 0.47, S = 0.44$) (a) predicted by our implicit Euler-Chebyshev numerical scheme applied to the 1D Oldroyd-B model (4.1) when two different initial fluid sample configurations are considered: a cylindrical sample (–) and a nearly cylindrical sample (–); and (b) experimental ($\diamond$) and 1D Oldroyd-B model (4.1) (–) results in Tembely *et al.* (2012). Vertical lines in (a) and (b) indicate the end of stretching. The implicit Euler-Chebyshev scheme applied to (4.1) correctly models the stretching process but R/R_p does not decay at longer times.

4.3 Approximate Axial Step-strain

We first investigate the impact of varying De and S on viscoelastic filament evolution throughout an approximate step-strain. We select values of $L_0 = 0.733$ and $L_f = 2.6$ to match or produce comparable initial and final aspect ratios, $\Lambda_0 = L_0/R_p$ and $\Lambda_f = L_f/R_p$, respectively, as those of our Newtonian silicone oil experiments

(c.f. chapter II). Yao & McKinley (1998) shows radial variations in $\tau^{p,zz}$ become increasingly important when Λ_0 decreases below unity. However, the initial aspect ratio varies from $0.71 \leq \Lambda_0 \leq 1$ in previous investigations (Kolte & Szabo 1999; Anna & McKinley 2001; Tembely *et al.* 2012; Vadillo *et al.* 2012).

The prescribed stretching time is $t_s = 4$ ms. For context, the stretching process in the Newtonian silicone oil experiments (c.f. chapter II) varies from 30 - 50 ms and is similar to other CBR studies (Rodd *et al.* 2005; Anna & McKinley 2001; Wagner 2015). The stretching time in Tembely *et al.* (2012), $t_s = 5.4$ ms, is considerably faster than most CBR studies because the fluid sample's viscous time scale must be larger than the stretching time to avoid break-up before the end of stretch (Rodd *et al.* 2005). Thus, t_s must be much smaller for low-viscosity fluids than for the higher-viscosity fluids considered in our Newtonian experiments in chapter II and previous studies (Rodd *et al.* 2005; Anna & McKinley 2001; Wagner 2015).

The differential Newtonian analysis (2.7) scaled by t_c, R_p, and σ is

$$\alpha^* = 1 = 6\left(Oh\frac{(3R_tR_{zz} - RR_{zzt})}{\kappa_{zz}R^2} - \frac{(3R_t^2 - RR_{tt})}{3\kappa_{zz}R^2}\right), \text{ at } R_z = 0. \tag{4.4}$$

Figure 4.4a shows the dimensionless midfilament evolution R/R_p predicted by the 1D viscoelastic model (4.1) throughout the stretching process for $Oh = 0.2$ with varying De and S. The results are presented as functions of t/t_s in a semilogarithmic plot. Values for R/R_p at $S = 0.98$ for $De = 1$ and $De = 100$ are indistinguishable throughout the stretching process. The decay in R/R_p for both cases at $S = 0.98$ generally resembles the inverted shape of $L(t/t_s)$ in figure 4.2. The initial evolution for $S = 0.25$ and $De = 100$ is very similar to the results for $S = 0.98$ but diverges and decays at a faster rate around $t/t_s = 0.5$. This deviation in R/R_p observed for $S = 0.25$ suggests elastic contributions are becoming significant and altering the filament evolution that is otherwise driven by the external forcing at the boundaries.

The differential method results for α^* (4.4) plotted with t/t_s for $Oh = 0.2$ with

varying De and S are shown in figure 4.4b. All results are generally noisy at the start of stretch due to the initial cylindrical filament profile and thus small κ_{zz}. Prior to the end of stretch, values of α^* (4.4) for $S = 0.98$ are relatively constant after the initial noise and deviate by roughly 2% from the expected value $\alpha^* = 1$. The $De = 1$ result decreases very modestly with increasing time whereas the $De = 100$ result grows modestly with time. The result for α^* when $S = 0.25$ and $De = 100$ increases rapidly early in the stretching process after the noise associated with the initial filament configuration. After the overshoot, values of α^* (4.1) are relatively constant for $0.20 < t/t_s < 0.75$ and then increase briefly near the end of the stretching process.

The evolution of the dimensionless capillary, viscous solvent, and elastic terms in the midfilament force balance (3.8) are plotted with t/t_s in figure 4.5. The capillary and viscous solvent contributions are generally the largest and second largest terms, respectively, throughout the stretching process and are qualitatively similar for the three cases. Additionally, the viscous solvent contributions grow faster than the elastic contributions initially. The capillary and viscous solvent terms at $S = 0.98$ for $De = 1$ and $De = 100$ are almost identical. The capillary term is initially non-zero and increases to a maximum around $t/t_s = 0.27$. The viscous solvent term initially increases from zero and passes through a maximum around $t/t_s = 0.27$. The two cases at $S = 0.98$ are distinguishable by their elastic contributions. The elastic term is larger for $De = 1$ and generally grows at a relatively constant rate. The elastic term is roughly 13% of the final viscous solvent contribution at the end of stretch. Although difficult to see on the scale shown in figure 4.5c, the elastic term for $De = 100$ grows with time and is therefore a small, non-zero value roughly 0.2% of the viscous solvent term at the end of stretch.

The capillary term for $S = 0.25$ and $De = 100$ grows to a larger maximum value around $t/t_s = 0.27$. At longer times during the stretching process the capillary term

for $S = 0.25$ decreases at a faster rate than the corresponding result at $S = 0.98$. The viscous solvent term for $S = 0.25$ is up to four times smaller than the result for $S = 0.98$. Finally, the elastic term for $S = 0.25$ and $De = 100$ grows rapidly from zero and is of the same order as the viscous solvent term at the end of the stretching process. It is 43% of the final viscous solvent contribution.

The trends in the capillary, viscous solvent, and elastic terms with respect to De and S during the initial deformation are generally the same as the results shown in chapter III for low-viscosity fluids. In particular, increasing the viscous polymer contribution (decreasing S) does not shift the peak viscous solvent term to earlier times but does reduce its overall contribution to the midfilament force balance (3.8). Additionally, the overall elastic contributions grow and its peak values shift to earlier times with decreasing S. The initial elastic growth rate decreases and peak values are smaller and shift to later times when De increases. However, no noticeable changes in the viscous solvent contributions are observed for increasing De when $S = 0.98$.

4.4 Oscillatory Boundary Motion

We also model the filament dynamics when the plates oscillate in time to evaluate the performance of the differential method (4.4) for an imposed deformation that avoids break-up. This deformation history may be particularly advantageous for characterizing low-viscosities fluids. Rodd *et al.* (2005) reports the standard CBR implementation with an axial step-strain is limited to viscosities greater than 70 mPa·s corresponding to $Oh > 0.1$. Therefore we model the filament evolution for two values of Oh above and below this critical limit of the standard CBR approach.

The velocity applied to both plates is

$$V_p\left(\frac{t}{t_c}\right) = \frac{\pi f(L_f - L_0)}{2}\sin\left(\frac{2\pi f t}{t_c}\right), \tag{4.5}$$

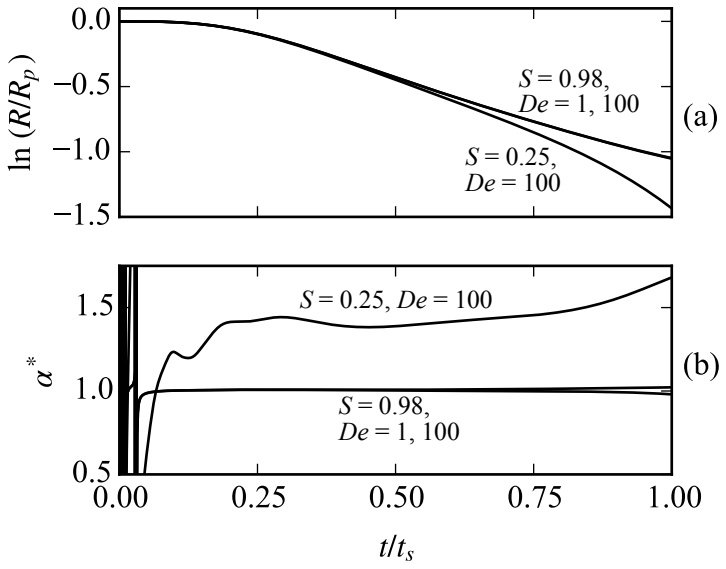

Figure 4.4: Dimensionless (a) filament midpoint evolutions R/R_p; and (b) differential method results for α^* determined by (4.4) as functions of dimensionless time t/t_s for $Oh = 0.2$ and various De and S during an approximate axial step-strain. The midfilament evolution is shown in a semilogarithmic plot. The results for $S = 0.98$ when $De = 1$ and $De = 100$ are generally indistinguishable.

where f is the dimensionless frequency scaled by t_c. The initial and final plate separations are $L_0 = 0.733$ and $L_f = 2$, respectively.

The 1D model (4.1) results for a low-viscosity Newtonian filament ($Oh = 0.05$, $De = 0$) evolving due to oscillatory boundary motion are summarized in figure 4.6. The boundaries oscillate at $f = 0.5$ which corresponds to a physical frequency of 125 Hz for an initially cylindrical fluid sample ($R_p = 1$ mm) with a density and surface tension similar to water. The plates oscillate for ten cycles ($0 \leq t/t_c \leq 20$) although only five cycles are shown for clarity. The temporal evolutions of R/R_p, α^*, and κ_{zz} show the results have reached stable limit cycles. The plate separation L resulting from the prescribed plate velocity (4.5) is shown with the midfilament evolution in figure 4.6a and both are plotted with ft/t_c or cycles. The local minimums (maximums) in R/R_p do not match the local maximums (minimums) in L because the filament midpoint continues to thin (thicken) due to inertia just after the plates reverse directions. The

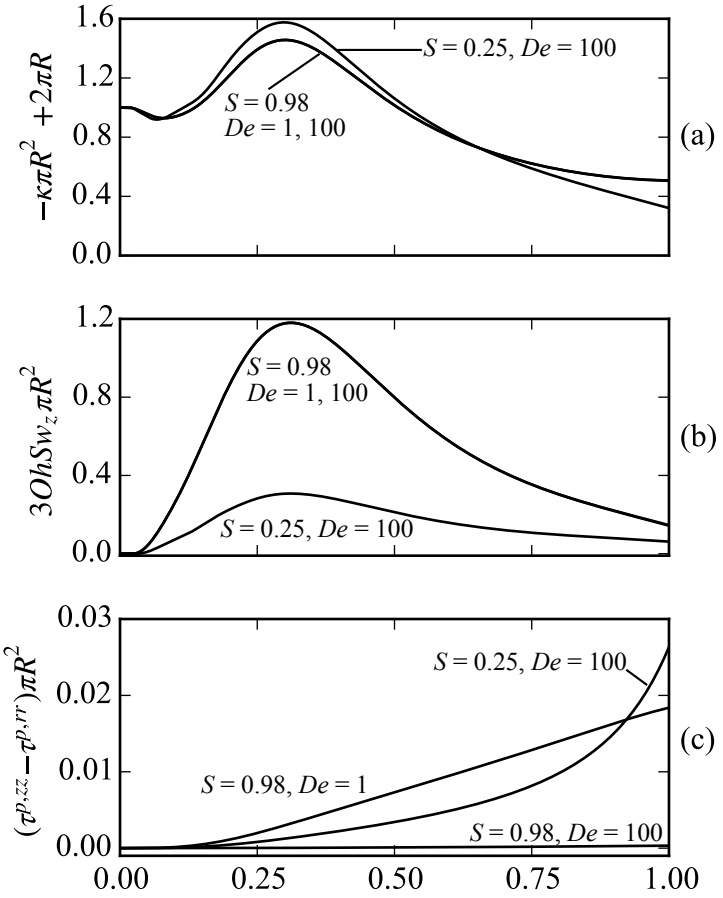

Figure 4.5: Evolution of dimensionless (a) capillary $-\kappa\pi R^2 + 2\pi R$; (b) viscous solvent $3OhSw_z\pi R^2$; and (c) elastic $(\tau^{p,zz} - \tau^{p,rr})\pi R^2$ force terms at the filament midpoint (3.8) as functions of dimensionless time t/t_s for $Oh = 0.2$ and various De and S during the stretching process. Results at $S = 0.98$ for $De = 1$ and $De = 100$ have very similar capillary and viscous solvent contributions but are distinguishable by their relatively insignificant elastic contributions.

delay between the local minimums in R/R_p and the maximums in L are $\Delta_1 = 0.02$ and are larger than the delay between the local maximums in R/R_p and minimums L ($\Delta_2 = 0.004$).

The differential method results for α^* (4.4) as a function of ft/t_c are shown in figure 4.6b. Equation (4.4) accurately predicts α^* to within 0.1% during the initial portion of each cycle. Several discontinuities in α^* are observed at later times in each cycle but the differential analysis (4.4) accurately predicts α^* between discontinuities. The cause for discontinuities is related to the filament shape and manifests in the temporal evolution of κ_{zz} evaluated at the midpoint as shown in figure 4.6c. Values of κ_{zz} are initially negative at the beginning of each cycle but grow and oscillate above and below zero at later times. Each discontinuity for α^* observed in figure 4.6b occurs when the value of κ_{zz} changes sign. Typically sign changes in κ_{zz} are associated with alterations in the concavity of $R(z)$ at the filament waist as in the case when a bead forms in the filament (i.e. figure 3.11). However, κ_{zz} also passes through zero when the terms that define it, consisting of higher-order derivatives of the free surface R_{zz} and R_{zzzz}, grow at different rates and coincidently cancel out. This is the case when κ_{zz} passes through zero in the middle of a cycle. However, as the plates return to their initial positions, variations in the sign of κ_{zz} are related to changes in the concavity of the free surface.

We also model the filament dynamics at $Oh = 0.05$ and $De = 0$ for $f = 1$. The results for R/R_p, α^*, and κ_{zz} are noisier when the frequency is doubled but qualitatively similar to the lower frequency results (figure 4.6) and are therefore not shown. The minimum values of R/R_p are 14% smaller than in $f = 0.5$. Values of Δ_1 and Δ_2 are 5 and 2.5 times larger, respectively, than those observed for $f = 0.5$. These results are caused by increased inertial effects due to higher accelerations when the frequency is increased. Additionally, the accuracy of the differential method (4.4) is slightly diminished compared to $f = 0.5$ but the results for α^* are still accurate to

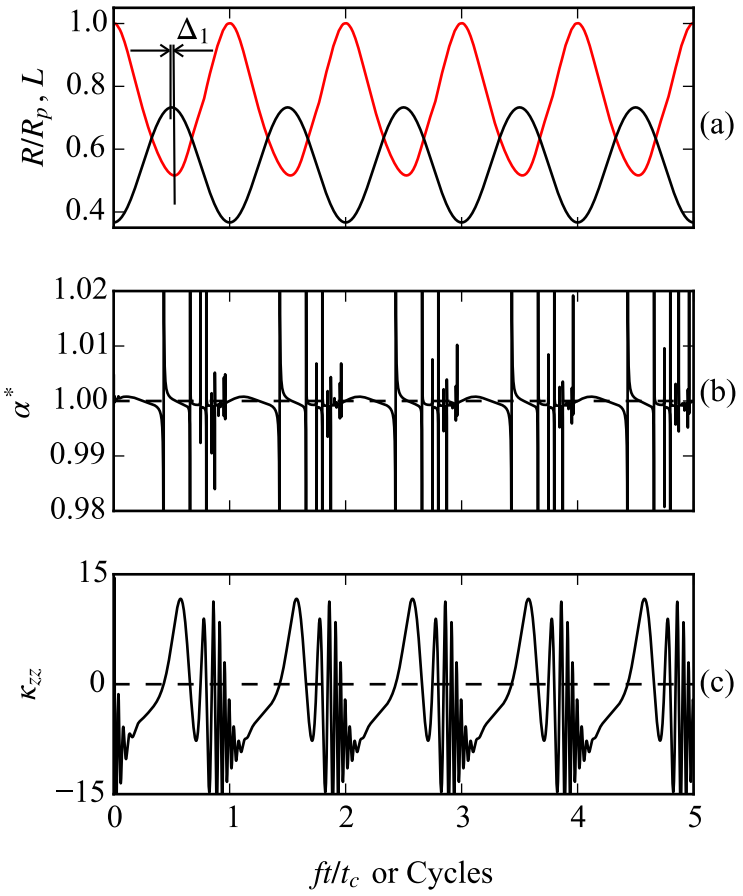

Figure 4.6: Dimensionless results for (a) the midfilament evolution R/R_p (–) and the plate separation L (–); (b) values of α^* determined by (4.4); and (c) κ_{zz} evaluated at the filament midpoint for a low-viscosity Newtonian filament ($Oh = 0.05, De = 0$) evolving due to boundaries oscillating at a dimensionless frequency $f = 0.5$. Results are plotted with dimensionless time ft/t_c or cycles. Only five of the ten cycles are shown for clarity. A delay Δ_1 between the local minimums in R/R_p and the local maximums in L is small but visible in (a). The delay between local maximums in R/R_p and local minimums in L is too small to be seen.

within 0.5%.

Figure 4.7 shows the same results as figure 4.6 for a more viscous Newtonian fluid ($Oh = 1, De = 0$). The boundaries also oscillate at $f = 0.5$ for ten cycles although only five cycles are shown. The results are also repeatable over multiple cycles. The minimum values of R/R_p are larger than those for $Oh = 0.05$ indicating a viscous filament thins slower as expected. Values of Δ_1 and Δ_2 are larger than the corresponding values for $Oh = 0.05$ and $f = 0.5$ but smaller than those for $Oh = 0.05$ and $f = 1$. The differential method results for α^* are less noisy than the results for $Oh = 0.05$ and also predict values within 0.1% of the expected value $\alpha^* = 1$. The discontinuities observed in α^* for $Oh = 1$ is also caused when κ_{zz} at the midpoint passes through zero. Discontinuities observed in the middle of the cycle are related to the growth rates in R_{zz} and R_{zzzz} whereas the discontinuities when the plates return to their initial positions are related to changes in the concavity of $R(z)$ at the filament midpoint.

4.5 Discussion

We model 1D filament dynamics driven by boundary motion with a single-mode Oldroyd-B model (4.1) to evaluate the performance of the differential method (4.4) during stretch where standard CBR analyses (2.4 and 3.11) are not typically applied. We first consider an approximate axial step-strain like the one imposed in traditional CBR experiments. Figure 4.4b shows determinations of α^* by (4.4) are more accurate near the Newtonian limit $S \to 1$ of the 1D model (4.1) during the stretching process. Additionally, the performance of the differential analysis (4.4) is relatively insensitive to the polymer relaxation time (De) near the Newtonian limit $S \to 1$. The differential method results do not increase from $\alpha^* = 1$ at the start of stretch but are noisy due to the initial condition for the free surface profile $R = 1$ and relatively slow early evolution around the filament midpoint. Thus terms in the numerator and

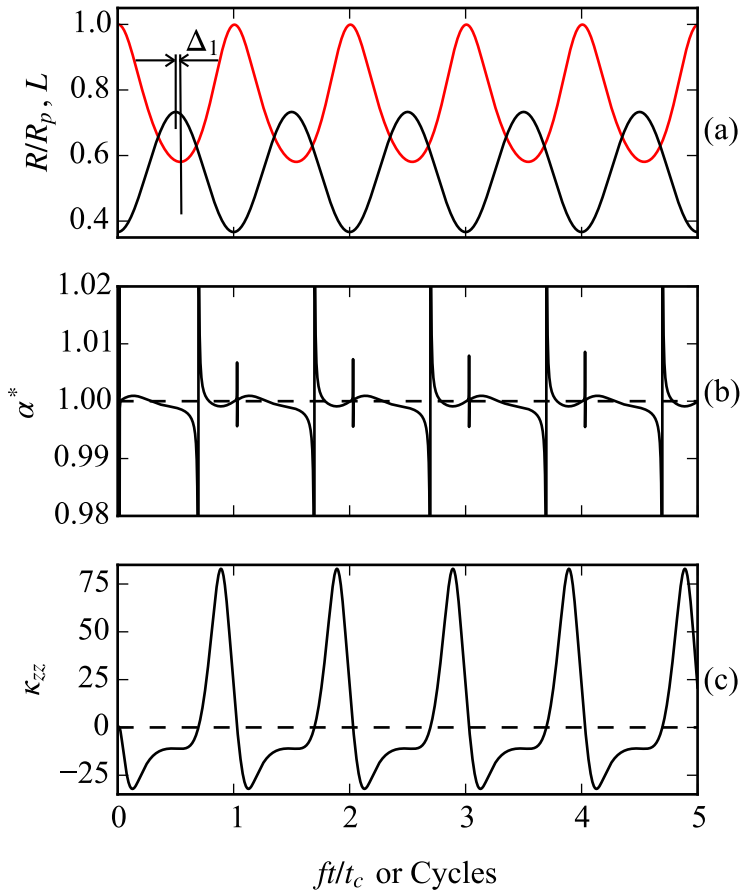

Figure 4.7: Dimensionless results for (a) the midfilament evolution R/R_p (–) and the plate separation L (–); (b) values of α^* determined by (4.4); and (c) κ_{zz} evaluated at the filament midpoint for a higher viscosity Newtonian filament ($Oh = 1, De = 0$) evolving due to boundaries oscillating at a dimensionless frequency $f = 0.5$. Results are plotted with dimensionless time ft/t_c or cycles. Only five of the ten cycles are shown for clarity. The delay Δ_1 between the local minimums in R/R_p and the local maximums in L observed in (a) are larger than Δ_1 for low-viscosity results shown in figure 4.6a. The delay between local maximums in R/R_p and local minimums in L is too small to be seen.

denominator of (4.4) are small, resulting in noisy and indeterminate values at the start of stretch. Following a brief noisy period, values of α^* are overpredicted with increasing viscoelastic effects, as best shown here for decreasing S. In particular, an early overshoot followed by a plateau is observed in the differential method results for α^* at $S = 0.25$ and $De = 100$ during the stretching process.

The overshoot in α^* (4.4) at $S = 0.25$ and $De = 100$ is caused by faster growth in the viscous solvent contribution than the polymer contribution at early times. This delay between the viscous solvent and polymer contributions also occurs in the $S = 0.98$ cases but leads to a smaller overshoot in α^* determined by (4.4) due to relatively small elastic effects compared with capillary and viscous solvent terms. Differential method results at $S = 0.98$ during the stretching process are also relatively insensitive to De because of small elastic effects. Finally, the results for α^* plateau during the deformation process when the elastic contributions grow at a relatively constant rate. This is best demonstrated by comparing the differential method results for $S = 0.25$ and $De = 100$ in figure 4.4b with the corresponding elastic contributions in figure 4.5c when $0.20 < t/t_s < 0.75$.

One small difference between the low-viscosity results in chapter III and the results shown here is observed in the initial growth and decay of the viscous solvent terms. The magnitude of the initial growth rate is larger than the magnitude of the decay rate for the viscous solvent terms when the stretching process is considered. In contrast, the initial growth in the the viscous solvent contributions for low Oh in chapter III is more gradual than the subsequent decay. This small but notable difference may cause the slight increase in α^* from its plateau. This is best seen in the results for $S = 0.25$ and $De = 100$ near the end of stretch $t/t_s = 1$.

In addition to modeling the axial step-strain, we also consider Newtonian filament evolution driven by oscillatory plate motion. The results in figures 4.6b and 4.7b demonstrate that the differential method (2.7) accurately characterizes material

parameters for low- and high-viscosity Newtonian filaments evolving due to oscillating boundary motion. This deformation is particularly advantageous for characterizing low-viscosity filaments because it avoids break-up. The result shown in figure 4.6b corresponds to a filament with a viscosity below the lower limit of the conventional CBR set-up (Rodd *et al.* 2005). Therefore the differential analysis (2.7) coupled with filament evolution driven by oscillating boundary motion can extend the measurement capabilities of standard CBR to lower viscosities. Values of α^* (4.4) for low-viscosity filament dynamics driven by oscillating boundary motion are noisier and slightly less accurate due to inertial effects when the frequency of the external forcing increases. Therefore, we suggest characterizing low-viscosities fluids at smaller frequencies $f < 0.5$ to improve the accuracy and quality of the measurement.

4.6 Conclusions & Future Work

We investigate 1D filament dynamics of initially squat fluid cylinders driven by boundary motion with a single-mode, 1D Oldroyd-B model (4.1). Unlike the typical development of CBR analyses and the work presented in chapter III, zero polymer stresses are realistic initial conditions representative of the original state of the physical fluid sample here. We apply the differential analysis (4.4) to the 1D model (4.1) results to evaluate its performance throughout the deformation process.

We first model an approximate axial step-strain similar to the deformation imposed on a fluid sample in a conventional CBR experiment. The differential method results for α^* (4.4) are relatively constant after an early overshoot during the stretching process when $De > 0$ and $S < 1$. Deviations from the expected value $\alpha^* = 1$ in the differential method results during the early plateau increase with growing viscoelastic effects, best demonstrated here by larger viscous polymer contributions (decreasing S). The overshoot in the results for α^* (4.4) occur due to slower initial growth in the elastic polymer contributions relative to the viscous solvent contributions. Addition-

ally, the differential method results plateau when the elastic contributions increase at relatively constant rate. The sensitivity of the differential method results during the early plateau to changes in the viscoelastic parameters may be useful for characterizing De and S. These results are consistent with the trends observed in chapter III. Furthermore, our results show the polymer stresses are non-zero and important relative to viscous solvent stresses at the end of the imposed deformation and start of the traditional CBR measurement regime. Therefore, we recommend applying the 1D differential analysis (4.4) throughout the deformation process to characterize material parameters from the early viscous phase.

Comparisons with experimental and numerical results for a weakly elastic low-viscosity fluid in Tembely *et al.* (2012) indicate our numerical approach applied to the 1D model (4.1) captures the filament dynamics during stretching reasonably well. However, our 1D model (4.1) predicts unrealistic results for R/R_p compared with the results in Tembely *et al.* (2012) following the end of the axial step-strain. Our preliminary efforts indicate the prescribed deformation profiles, strains, and initial conditions affects the accuracy of our 1D model results at longer times after stretch. We experienced similar difficulties in modeling low-viscosity filament evolution at longer times, particularly when elastic effects become important, in chapter III. Thus, future work will consider numerical modifications for addressing the viscoelastic filament evolution for low-viscosity fluids.

We also model the 1D filament evolution driven by oscillating boundaries for Newtonian fluids with viscosities above and below the lowest viscosity currently resolved by the standard CBR implementation (Rodd *et al.* 2005). The results for α^* demonstrate the differential analysis (4.4) coupled with a deformation history that avoids break-up can extend the range of the conventional CBR technique to lower viscosities. However, the differential method results become noisier for low-viscosity filaments. Additionally, values of α^* for the low-viscosity filament become noisier and slightly

less accurate with increased frequency of the external boundary motion. For now, we recommend characterizing low-viscosity Newtonian fluids by (4.4) when the boundaries oscillate at small frequencies $f < 0.5$. Continuing work will also consider other means of reducing noise in the differential method results for low-viscosity fluids such as imposing smaller strains and beginning with non-cylindrical filament samples to avoid the discontinuity observed in α^* when the boundaries return to their initial positions.

Ongoing work will also evaluate the performance of the 1D differential analysis (4.4) applied to 1D viscoelastic filament evolution driven by oscillatory boundary motion. Large amplitude oscillatory extension (LAOE) measurements have previously been demonstrated in a filament stretching device (Bejenariu *et al.* 2010) and a cross-slot device (Zhou & Schroeder 2016). However, the filament stretching device requires a force measurement that is difficult for low-viscosity fluids and the cross-slot device imparts shear into the planar extensional flow due to the channel walls (Galindo-Rosales *et al.* 2013). Therefore, we seek to characterize viscoelastic material parameters from the filament evolution driven by oscillatory boundary motion with a 1D differential approach in our future work.

CHAPTER V

Conclusions & Future Work

5.1 Summary and Key Findings

The primary motivation for our work is to develop a suitable technique for characterizing extensional saliva rheology for potential health applications. Since saliva is a low-viscosity, non-Newtonian fluid, we have focused on re-examining an existing rheometric method, capillary break-up rheometry, because it does not require a force measurement to characterize fluid samples. This is an advantageous feature for low-viscosity fluids where forces are difficult to measure accurately. Whereas standard 1D CBR analyses (Bazilevsky *et al.* 1990; Entov & Hinch 1997; McKinley & Tripathi 2000) apply additional approximations to preclude a force measurement, the objective of our work is to develop an alternative analysis that does not require any additional assumptions beyond the 1D, rectilinear flow description. We also seek to expand the operating range of conventional CBR to facilitate the characterization of multiple rheological parameters from a single sample.

Chapter II developed a 1D differential Newtonian analysis (2.7) for CBR to determine the surface tension to viscosity ratio α. Our analysis is based on the 1D differential forms of the governing equations for mass and momentum. Our local differential analysis did not require specific assumptions for the axial force F to preclude its measurement. Our analysis indicated that measuring gradients in filament

curvature is necessary to accurately determine α when F is not measured. From our experimental and numerical results for viscous Newtonian filament evolution, we found axial symmetry about the midfilament (where $R_z = 0$) is a major requirement to maintain an accurate and purely geometric approach (i.e. avoiding velocity measurements) for determining α^* by the differential analysis (2.7) (figure 2.2). We have therefore constructed a time-varying asymmetry measure $\Omega(t)$ (2.9). We recommend applying the differential analysis (2.7) when $\Omega(t)$ is small relative to the initial asymmetry and $d\alpha^*/d\Omega \to 0$ (figure 2.5).

In chapter III, we investigated the role of surfactants and viscoelasticity on 1D filament dynamics. Our experiments with a simple soap-and-water mixture supported our conjecture that saliva's surface active constituents do not play a significant role in its ability form filaments. There is evidence that saliva's surface active constituents play an important role in forming protective films on soft tissues and teeth in the oral cavity, however this is beyond the scope of this work. Thus we investigated viscoelastic effects on 1D filament evolution with a 1D Oldroyd-B model for high- and low-viscosity fluids. We followed the typical development of CBR analyses that assume the viscoelastic filaments are initially long and unstable with zero polymer stresses. This is an unrealistic representation of the physical fluid sample after the imposed deformation process (start of CBR measurement) because viscoelastic filaments have memory and are therefore affected by the stretch history. However, this assumption used by almost all previous studies (Bazilevsky *et al.* 1990; Entov & Hinch 1997; Bousfield *et al.* 1986; Renardy 1994; Clasen *et al.* 2006*a*) simplified the analysis and is useful for investigating trends in the filament evolution due to varying viscoelastic parameters.

We emphasize applying the (dimensionless) differential method (3.16) to the early viscous phase of 1D viscoelastic filament evolution because the current CBR approach (3.11) for characterizing the polymer relaxation time λ from the middle elastic regime

works well. For high- and low-viscosity filaments ($Oh = 3.16$ and $Oh = 0.002$, respectively), the differential analysis (3.16) accurately determined α^* in the Newtonian limits of the 1D model (3.12): $De \to 0$, $S \to 1$, or small deformations (figures 3.4, 3.7b, 3.9b and 3.12b). For high-viscosity filaments when $De > 0$ and $S < 1$, $\alpha^* = 1$ initially (for gradual startups) but rapidly increased and then plateaued. The initial overshoot is caused by slow, unsteady growth in the elastic contribution at early times in the viscous regime. Following the initial unsteady growth, elastic contributions increased at a relatively constant rate for a brief period corresponding to the plateaus observed in the results for α^* (3.16) (figures 3.5c and 3.8c). The differential method results during the plateau deviated from the expected value $\alpha^* = 1$ and deviations increased with growing viscoelastic effects (increasing De, decreasing S).

Varying De and S for the low-viscosity case considered here produced similar trends in the growth of the elastic contributions. However, both elastic and viscous solvent contributions were relatively insignificant compared with the capillary contributions during the initial viscous phase (figures 3.10 and 3.13). Thus the filament dynamics during the early viscous regime when viscoelastic effects are non-zero were indistinguishable from a nearly inviscid Newtonian fluid at $Oh = 0.002$ (i.e. water). Consequently, the differential method results (3.16) were also relatively insensitive to variations in De and S and predicted $\alpha^* = 1$ (figures 3.9 and 3.12).

Based on the model results for high- and low-viscosity viscoelastic fluids, we recommend characterizing the total viscosity μ_0 of the fluid sample from the differential method results for α^* when deformations are small at the start of the measurement. The sensitivity of the differential method results (3.16) during the early plateau to variations in Oh, De and S, particularly for high-viscosity fluids, suggests the effects of De and S may also be separately characterized.

In chapter IV we studied 1D filament evolution driven by boundary motion with a single-mode, 1D Oldroyd-B model (4.1). We considered cases of initially stable

fluid samples at rest. Thus, zero polymer stresses were appropriate initial conditions here. The first deformation history we modeled is an approximate axial step-strain to represent the typical deformation imposed in a CBR experiment. Results for α^* determined by (4.4) and the capillary, viscous solvent and elastic contributions to the midfilament force balance (3.8) generally followed the same trends for De and S observed in chapter III. In particular, an initial overshoot followed by a plateau was also observed in the differential method results during the stretching process for the low-viscosity fluid considered ($Oh = 0.2$). The initial overshoot and following plateau corresponded to slow, initial growth in the elastic contribution followed by a period of relatively constant growth (figures 4.4 and 4.5). Furthermore, values of α^* (4.4) during the early plateau deviated from the expected value $\alpha^* = 1$ with increasing viscoelastic effects. The results of the 1D model (4.1) with the approximate step-strain also showed the polymer stresses and viscous solvent stresses were comparable at the end of the imposed deformation and start of the traditional CBR measurement regime. Therefore, we recommend applying the 1D differential analysis (4.4) to characterize material parameters such as μ_0 during the initial deformation process before the onset of elastic effects.

We also modeled the 1D filament dynamics due to oscillatory boundary motion for low- and high-viscosity Newtonian filaments to consider a deformation history that avoids filament break-up. In particular, we modeled Newtonian filaments with viscosities above and below the lowest viscosity currently resolved by the standard CBR set-up (Rodd *et al.* 2005). The results for α^* (4.4) for the low-viscosity filament (figure 4.6) showed the differential analysis (4.4) coupled with a deformation history that avoids break-up can extend the range of the conventional CBR technique to lower viscosities. However, the differential method results were noisier for low-viscosity filaments compared to high-viscosity filaments (figures 4.6 and 4.7). Additionally, the differential method results for the low-viscosity filament were adversely affected when

the frequency of the oscillating boundaries increased. Thus, we suggest characterizing low-viscosity filaments by the differential method (4.4) with a low-frequency ($f < 0.5$) oscillatory deformation profile.

We verified our implicit Euler-Chebyshev numerical scheme applied to the 1D Oldroyd-B model (3.12) with literature (Clasen *et al.* 2006*a*) for high-viscosity viscoelastic fluids. We also verified our 1D modeling for low-viscosity viscoelastic fluids only during the stretching process by comparing with experimental and 1D model results in Tembely *et al.* (2012). However, modeling low-viscosity viscoelastic fluids at longer times, especially when elastic effects became significant relative to viscous solvent stresses, was a consistent challenge in chapters III and IV. Fortunately, this did not affect our analysis of the initial viscous phase but is an area of continuing research.

We must first evaluate the validity of the 1D approximation for low-viscosity fluids. Schultz & Davis (1982) shows adding inertia disrupts the 1D approximation. However, a 1D linear stability analysis predicts the maximum growth rate for a disturbance in a nearly inviscid fluid occurs at a wavenumber k_{max} that is within 2% of the value determined by Rayleigh (1879) and the 3D linear stability analysis by Chandrasekhar (1961). Therefore, it is currently uncertain if a 1D approximation is appropriate even when considering a modest amount of inertia.

Additionally, comparisons with other viscoelastic literature (Clasen *et al.* 2006*a*; Tembely *et al.* 2012) suggest we may need to consider modifications to our numerical approach, such as adaptive temporal and/or spatial schemes, to resolve the larger range of scales in low-viscosity viscoelastic fluid evolution. Our preliminary work also shows the 1D model results for low-viscosity viscoelastic fluids after the stretch are sensitive to the initial fluid sample configuration, imposed strain, and the prescribed deformation profile. Therefore, these parameters must be accurately modeled in ongoing efforts.

Overall we have demonstrated the performance of our 1D differential analysis (2.7) for characterizing Newtonian filaments and the early viscous phase of non-Newtonian filament evolution. Measurements of multiple rheological properties from a single fluid sample may be obtained by combining the differential analysis (2.7) during the early viscous regime with the current CBR method for determining the polymer relaxation time λ (3.11) during the middle elastic phase. This is advantageous for saliva studies, particularly when investigating patients with reduced salivary production. Additionally, we have demonstrated the differential method (2.7) is robust during the deformation process and may be used with stretch histories that avoid break-up to extend the measurement range of traditional CBR.

5.2 Future Work

The work presented in this dissertation demonstrates the potential of the 1D differential analysis (2.7) to expand the measurement capabilities of the current CBR technique. However, additional efforts are required to refine the 1D differential method before it can be used widely to characterize fluid samples. In the first two subsections, we discuss additional tasks necessary to improve the 1D differential method (2.7). In the final two subsections, we recommend investigations to further expand the capabilities of the 1D differential method.

5.2.1 Experiments

A set of complementary experiments for non-Newtonian filaments with varying viscoelastic effects must be performed to verify the trends observed in chapters III and IV. This will require a CBR device capable of prescribing the desired deformation histories. The latest version of our CBR device described in appendix B is limited to four deformation histories: a step-strain, triangular wave oscillations, ramp-strain, and sinusoidal oscillations. However, none of these deformations work particularly

well. This may be caused by the stepper motor providing accurate positioning but not smooth time-varying velocity at the boundaries. Therefore minor modifications to our current CBR device are required.

Additional efforts must also focus on optimizing the post-processing routine to analyze experimental images of the filament evolution. In particular, the accuracy and error in the differential analysis will improve by optimizing the least-squares polynomial fits of the filament free surface. Improving the radial resolution by developing an edge detection scheme that uses grayscale more effectively will aid the optimization of the the least-squares polynomial fits. Additionally, the domain size and the degree of the polynomial fit must also be optimized to minimize error in the differential approach (2.7).

5.2.2 1D modeling

We must first address the challenges encountered in modeling low-viscosity viscoelastic filament evolution, particularly when elastic contributions become comparable to viscous solvent contributions, to facilitate comparisons with experiments. A complete description of low-viscosity filament evolution predicted by a 1D model will be useful for investigating quantities that are difficult to measure experimentally, such as the axial velocity and individual stresses. Therefore, alternative numerical approaches must be considered to improve the current state of the 1D modeling. This may require implementing adaptive spatial and temporal meshes to resolve the large range of scales in viscoelastic filament dynamics. Additionally, we will also re-examine the appropriate boundary conditions for the polymer stresses.

After challenges with the numerical methods are addressed, other constitutive theories such as the generalized convected Jeffreys and FENE-P models may be considered. These models contain methods to avoid issues with the singularity at higher strain-rates and therefore will produce more physical results at longer times.

5.2.3 Characterizing the $Oh - De - S$ space

In chapters III and IV we showed the differential method results for α^* reach a plateau during the early viscous regime. Values of α^* during the plateau are sensitive to variations in Oh, De and S and thus may be useful for quantifying individual parameters. Therefore we recommend investigating the $Oh - De - S$ space to determine correlations to enable characterizations of additional material parameters from the early viscous regime.

5.2.4 Oscillatory boundary motion

In chapter IV we demonstrated the differential analysis (4.4) coupled with an oscillatory deformation profile yields accurate but noisy results for α^*. In addition to reducing the prescribed oscillation frequency, we propose investigating the impact of strain and the initial fluid sample free surface on reducing noise in low-viscosity results determined by (4.4).

Finally, we recommend investigating 1D viscoelastic filament evolution driven by oscillatory boundary motion to develop a 1D analysis for low-viscosity elastic fluids. Additionally, 1D viscoelastic multi-mode models should be considered to determine if multiple relaxation times may be characterized with oscillatory deformation profiles of varying frequencies in extension. In this regard, the experiments and analysis can be performed without break-up and its associative challenges. Then, this revised method should change its name from capillary break-up rheometry to capillarity rheometry.

APPENDICES

APPENDIX A

Probative Saliva Experiments

The purpose of these preliminary experiments is to inform the experimental design for larger scale investigations of saliva. We qualitatively investigated the impact of pH, salinity, dilution, and filtering on saliva filament dynamics. In particular, we observed the length and longevity of the saliva filament compared with an unadulterated sample. Saliva samples were collected from two healthy individuals, one female and one male both ∼30 years-old. We considered acids, bases, and salts commonly found in our diet, such as vinegar (acetic acid), lemon juice, baking soda, NaCl (table salt), and KCl. Additionally, we considered the impact of dilution (i.e. when we drink liquids) and filtering saliva.

Methods

Samples were collected by asking participants to expectorate into a cup until ∼10 - 15 mL (2 - 3 teaspoons) were collected. Resting saliva samples from both participants were collected without stimulation for 30 - 45 minutes. Additionally, stimulated saliva samples were produced by applying a lemon wedge to the female participant's tongue for 15 minutes. Samples were then divided into 2.5 mL (1/2

teaspoon) increments. The following were then added to individual "clean" samples of resting and/or stimulated salivas:

- $\sim$1 μL drop distilled white vinegar (Meijer, 5% acetic acid) (resting and stimulated salivas)
- $\sim$1 μL drop lemon juice (resting and stimulated salivas)
- $\sim$1/16 teaspoon baking soda (resting saliva)
- $\sim$1/16 teaspoon NaCl (resting and stimulated salivas)
- $\sim$1/16 teaspoon KCl (resting saliva)

Additionally, an individual sample of resting saliva was filtered (AeroPress coffee filter) and another was diluted with water at a 1:1 ratio.

The pH of unadulterated and altered samples were measured with pH indicator strips (Whatman Panpeha).

Finally, a $\sim$1 mm^3 drop of each sample was stretched between forefinger and thumb to observe the length (measured by a millimeter scale) and longevity of the filament. This procedure was performed three times with a fresh drop each time for all samples.

Results

The results of our qualitative study are summarized in table A.1. All comparisons are made with respect to the length and longevity of unadulterated resting and stimulated salivas samples. Unadulterated stimulated saliva filaments were comparable to resting saliva. Adding vinegar or lemon juice generally increased the filament length and lifetime although a larger difference was observed when acids were added to resting saliva. Shorter filaments with smaller lifetimes were observed when baking

soda was added to resting saliva. This was also observed when NaCl was added to resting and stimulated salivas. Filament formation was not affected by adding KCl to resting saliva. Finally, filaments were difficult to form with filtered (resting) saliva whereas filament formation was not affected by dilution.

Discussion

Zussman *et al.* (2007) shows saliva samples stimulated with an acid have larger polymer relaxation times than resting saliva samples and hypothesizes this is caused by increased salivary protein concentration. Our filtered saliva result is consistent with Zussman *et al.* (2007). However, our pH manipulation is generally performed outside the oral cavity unlike Zussman *et al.* (2007). Therefore, our results for ex-vivo saliva pH manipulation suggests increased viscoelasticity may also be due to conformational changes in the saliva proteins.

Since the results are similar for the two different acids, this suggests the type of acid is not important. However, our qualitative results for salts suggests the type of salt does matter. We recommend further studies on the impact of in-vivo and ex-vivo pH manipulation on saliva filament dynamics. In addition, we suggest a study to determine the effects of various salts on saliva filament dynamics.

Table A.1: Qualitative results for investigation of pH, salinity, filtering, and dilution on saliva filament formation

			Promotes formation	**Neutral**	**Hinders formation**
salts		NaCl			X
		KCl		X	
pH	~ 3.5	lemon juice or vinegar	X		
	~ 8.5	baking soda			X
		filtering			X
		1:1 dilution		X	

APPENDIX B

Experimental Apparatus

General Experimental Set-Up and Procedure

The experimental set-up consists of a CBR device, a camera with appropriate optics, a computer, and a lighting source. As described in chapter II, the CBR device has two parallel, circular plates of radius R_p initially separated by a distance L_0. The fluid sample is constrained by the initial gap geometry and forms a squat cylinder. For both versions of the CBR device developed throughout this work (discussed in the next couple sections), the top plate is held fixed while the bottom plate is free to move and its motion imposes the approximate axial step-strain (or alternate deformation history) on the fluid sample. The filament evolution is backlit with either simple flashlight or fiberoptic lightsource and then captured by a camera through a microscope objective to increase the spatial resolution near the filament midpoint. Typically a 10x Nikon microscope objective (numerical aperture $NA = 0.30$, magnification $M = 14$, 1.2 μm/pixel) is used when $R_p \leq 2$ and a 4x Nikon objective (NA =0.13, $M = 4.4$, 3.2 μm/pixel) is used for $R_p \geq 3$.

CBR Device "Alpha" Model

The first version of the CBR device, the "alpha" model, was used to perform the Newtonian silicone oil experiments in chapter II. It is constructed with optomechanical posts and plates typically used for mounting laser optics. The circular plates are polylactic acid (PLA) plastic and created using a 3D printer. Three different plate sizes are available ($R_p = 2, 3$ and 4 mm) to vary the fluid sample size. The alpha model is limited to imposing one deformation history: the approximate step-strain. The top plate is held fixed while the bottom plate falls due to gravity until a final plate separation of L_f. The bottom plate is attached to a stem with two collars to guide the vertical motion. The upper collar acts as a stop for the moving assembly and may be adjusted to vary L_f and consequently the strain L_f/L_0.

CBR Device "Beta" Model

A second version of the CBR device, the "beta" model, was constructed by a undergraduate senior design team and has not been used extensively in experiments yet. Several updates and useful features have been added in the "beta" model. The top plate still remains fixed while the lower plate position is driven by a stepper motor. The rotary motion of the stepper motor is converted to linear motion with a lead screw and nut. The downward motion of the lower plate is limited by a "hard-stop rail" to prevent the motor from driving the nut into itself. A contact switch is mounted to the hard-stop rail and is used to recalibrate the distance between the plates. An Arduino Uno controls the motion of the stepper motor and four different stretch histories have been programmed: a step-strain, triangular wave oscillations, ramp-strain, and sinusoidal oscillations.

The interchangeable plates ($R_p = 1, 2$ and 3 mm) are also constructed from aluminum. The top and bottom plates are mounted to pin alignment blocks. The top

pin alignment block has two thru holes and the bottom pin alignment block has two blind holes. The top plate and its pin alignment block are attached to a translation stage and mounted to the frame of the new CBR device. The bottom plate and its pin alignment block are attached to the stepper motor. The plates are aligned by adjusting the position of the top plate with the translation stage until two dowel pins can easily pass through the two thru holes in the top pin alignment block and fit easily in the corresponding blind holes in the bottom pin alignment block.

APPENDIX C

Numerical Methods

The purpose of this appendix is to describe the temporal and spatial schemes implemented to solve the 1D Newtonian and Oldroyd-B models in chapters II - IV. These numerical schemes are implemented in Python. The 1D models are repeated here for convenience and to enable a discussion about common features.

The dimensionless continuity equation integrated over the filament cross-section is the same for both the Newtonian and Oldroyd-B models despite different scalings

$$(R^2)_t + (wR^2)_z = 0. \tag{C.1}$$

The axial momentum equation scaled by a capillary velocity scale σ/μ and the plate radius R_p is

$$Re(w_t + ww_z)R^2 = (3w_zR^2)_z - \kappa_z R^2 - BoR^2. \tag{C.2}$$

Equations (C.1) and (C.2) form the viscous 1D Newtonian model.

The axial momentum equation scaled by R_p, σ, and an inertio-capillary time scale $t_c = \sqrt{\rho R_p^3/\sigma}$ is

$$(w_t + ww_z)R^2 = -\kappa_z R^2 + 3OhS(w_z R^2)_z + ((\tau^{p,zz} - \tau^{p,rr})R^2)_z \tag{C.3a}$$

$$\tau^{p,zz} + De(\tau_t^{p,zz} + w\tau_z^{p,zz} - 2w_z\tau^{p,zz}) = 2Oh(1-S)w_z \tag{C.3b}$$

$$\tau^{p,rr} + De(\tau_t^{p,rr} + w\tau_z^{p,rr} + w_z\tau^{p,rr}) = -Oh(1-S)w_z. \tag{C.3c}$$

Equations (C.1) and (C.3) form the 1D Oldroyd-B model.

The dimensionless mean curvature for both models is

$$\kappa = \frac{1}{R(1+R_z^2)^{1/2}} - \frac{R_{zz}}{(1+R_z^2)^{3/2}}. \tag{C.4}$$

The axial momentum equation (C.2 or C.3b) requires one spatial derivative of κ

$$\kappa_z = \frac{-R_z}{R^2(1+R_z^2)^{1/2}} - \frac{R_z R_{zz}}{R(1+R_z^2)^{3/2}} - \frac{R_{zzz}}{(1+R_z^2)^{3/2}} + \frac{3R_z R_{zz}^2}{(1+R_z^2)^{5/2}}. \tag{C.5}$$

1D Newtonian Model (without Stretch)

The symmetric and viscous ($Re = 0, Bo = 0$) 1D Newtonian model (C.1 and C.2) without stretch (c.f. chapter II) is solved with a 4th-order Runge-Kutta (R-K) temporal integration scheme and a 2nd-order centered finite difference scheme. The 4th-order R-K method is an explicit temporal integration scheme and is applied to the following evolution equation for R (derived from (C.1)) at every time step

$$R_t = \frac{-w_z R}{2} - wR_z = f(R, w, t). \tag{C.6}$$

The 4th-order R-K solution procedure to determine the solution to (C.6) at the next time step $m+1$ from the solution at the current time step m is

$$R^{m+1} = R^m + \frac{1}{6}k_1 + \frac{1}{3}(k_2 + k_3) + \frac{1}{6}k_4, \tag{C.7}$$

where Δt is the time step and

$$k_1 = \Delta t f(R^m, w^m, t^m) \tag{C.8a}$$

$$k_2 = \Delta t f(R^m + \frac{1}{2}k_1, w^m, t^m + \frac{\Delta t}{2}) \tag{C.8b}$$

$$k_3 = \Delta t f(R^m + \frac{1}{2}k_2, w^m, t^m + \frac{\Delta t}{2}) \tag{C.8c}$$

$$k_4 = \Delta t f(R^m + k_3, w^m, t^m + \Delta t). \tag{C.8d}$$

The symmetric and viscous 1D Newtonian model in chapter II considers $N = 513$ nodes on a uniform spatial mesh. Spatial derivatives determined by the 2nd-order finite difference stencils are applied to all interior nodes $i = 1...N-1$. Dirchlet boundary conditions for R and w are applied to the boundary nodes, $i = 0$ and $i = N-1$. For any dependent variable f, the first and second derivative at all interior nodes is determined according to the following stencils

$$f_z^i = \frac{f^{i+1} - f^{i-1}}{2\Delta z}, \text{for } i = 1...N-2, \tag{C.9}$$

and

$$f_{zz}^i = \frac{f^{i+1} - 2f^i + f^{i-1}}{(\Delta z)^2}, \text{for } i = 1...N-2, \tag{C.10}$$

where Δz is the spatial step. The third derivative stencil requires two nodes on either side of the i-th node. Therefore, a lopsided stencil must be applied to the two nodes immediately adjacent to the boundary nodes

$$f_{zzz}^{i=1} = \frac{f^3 - 3f^2 + 3f^1 - f^0}{(\Delta z)^3} \tag{C.11a}$$

$$f_{zzz}^{i=N-2} = \frac{f^{N-1} - 3f^{N-2} + 3f^{N-3} - f^{N-4}}{(\Delta z)^3}. \tag{C.11b}$$

The third derivative stencil for all other interior nodes is

$$f_{zzz}^{i} = \frac{f^{i+2} - 2f^{i+1} + 2f^{i-1} - f^{i-2}}{2(\Delta z)^3}, \text{for } i = 2...N-3. \tag{C.12}$$

1D Newtonian and Oldroyd-B models (with and without Stretch)

The 1D Oldroyd-B model (C.1 and C.3) in chapters III and IV are solved with an implicit backward Euler temporal scheme and Chebyshev spatial scheme. In addition, an arbitrary Lagrangian-Eulerian (ALE) scheme is employed to prescribe node velocities v_n proportional to the boundary velocity. All partial time derivatives in the 1D models (C.1, C.2, and C.3) are replaced by

$$\frac{\partial}{\partial t} = \frac{d}{dt} - v_n \frac{\partial}{\partial z}, \tag{C.13}$$

where $v_n = xV_p(t/t_s)$. Additionally, $z \in [-L/2, L/2]$ is mapped to the Chebyshev domain $x \in [-1, 1]$ with a linear scaling $x = \frac{2}{L}z$. Thus, the 1st, 2nd, and 3rd derivatives in z are

$$\frac{\partial}{\partial z} = \frac{\partial x}{\partial z}\frac{\partial}{\partial x} = \frac{2}{L}\frac{\partial}{\partial x} \tag{C.14a}$$

$$\frac{\partial^2}{\partial z^2} = \left(\frac{\partial x}{\partial z}\right)^2 \frac{\partial^2}{\partial x^2} = \frac{4}{L^2}\frac{\partial^2}{\partial x^2} \tag{C.14b}$$

$$\frac{\partial^3}{\partial z^3} = \left(\frac{\partial x}{\partial z}\right)^3 \frac{\partial^3}{\partial x^3} = \frac{16}{L^3}\frac{\partial^3}{\partial x^3}. \tag{C.14c}$$

We demonstrate the equations for the Newtonian limit $S \to 1$ of the 1D Oldroyd-B model, when $\tau^{p,zz} = \tau^{p,rr} = 0$, to simplify the example. Equations (C.6 and C.3a) rewritten according to (C.13) and (C.14) and rearranged in the form of evolution equations are

$$\begin{aligned} \frac{dR}{dt} &= \frac{-w_x R}{L} - \frac{2}{L} w R_x \\ &= f(R, R_x, w, w_x), \end{aligned} \tag{C.15}$$

$$\begin{aligned} \frac{dw}{dt} &= -\frac{2}{L}(w - v_n) w_x - \kappa_z + \frac{12}{R^2 L} OhS \left(w_x R^2 \right)_x \\ &= g(R, R_x, R_{xx}, R_{xxx}, w, w_x, w_{xx}). \end{aligned} \tag{C.16}$$

The evolution equations for R and w (C.15-C.16) must first be linearized according to a Taylor-series expansion where all dependent variables and their spatial derivatives are treated as individual variables. Additionally, the temporal derivatives $\frac{dR}{dt}$ and $\frac{dw}{dt}$ are discretized to give

$$\begin{aligned} \frac{R^{m,k} + \delta R - R^m}{\Delta t} = \\ f|^{m,k} + \frac{\partial f}{\partial R}\Big|^{m,k} \delta R + \frac{\partial f}{\partial R_x}\Big|^{m,k} \delta R_x + \frac{\partial f}{\partial w}\Big|^{m,k} \delta w + \frac{\partial f}{\partial w_x}\Big|^{m,k} \delta w_x, \end{aligned} \tag{C.17}$$

$$\begin{aligned} \frac{w^{m,k} + \delta w - w^m}{\Delta t} = \\ g|^{m,k} + \frac{\partial g}{\partial R}\Big|^{m,k} \delta R + \frac{\partial g}{\partial R_x}\Big|^{m,k} \delta R_x + \frac{\partial g}{\partial R_{xx}}\Big|^{m,k} \delta R_{xx} + \frac{\partial g}{\partial R_{xxx}}\Big|^{m,k} \delta R_{xxx} \\ + \frac{\partial g}{\partial w}\Big|^{m,k} \delta w + \frac{\partial g}{\partial w_x}\Big|^{m,k} \delta w_x + \frac{\partial g}{\partial w_{xx}}\Big|^{m,k} \delta w_{xx}, \end{aligned} \tag{C.18}$$

where k refers to the current iteration. The new iteration $R^{m,k+1}$ ($w^{m,k+1}$) is the sum of the current iteration $R^{m,k}$ ($w^{m,k}$) and some small change δR (δw). Please note R^m (w^m) refers to the solution at the current time step, not the current iteration!

Once the spatial scheme is applied, equations (C.17) and (C.18) form a $2N \times 2N$ system of equations. The system of equations can be rewritten as a partial differential equation for δx (containing δR and δw) in the form $\delta F(\delta x; x^{m,k}) = -F(x^{m,k}, x^m)$, where $x^{m,k}$ contains $R^{m,k}$ and $w^{m,k}$ at the current iteration and x^m contains R^m and w^m at the current time step

$$F = \frac{R^{m,k} - R^m}{\Delta t} - f|^{m,k} + \frac{w^{m,k} - w^m}{\Delta t} - g|^{m,k} \tag{C.19}$$

$$\begin{aligned}
\delta F = &\frac{\delta R}{\Delta t} - \left(\frac{\partial f}{\partial R}\Big|^{m,k} \delta R + \frac{\partial f}{\partial R_x}\Big|^{m,k} \delta R_x + \frac{\partial f}{\partial w}\Big|^{m,k} \delta w + \frac{\partial f}{\partial w_x}\Big|^{m,k} \delta w_x \right) \\
&\frac{\delta w}{\Delta t} - \left(\frac{\partial g}{\partial R}\Big|^{m,k} \delta R + \frac{\partial g}{\partial R_x}\Big|^{m,k} \delta R_x + \frac{\partial g}{\partial R_{xx}}\Big|^{m,k} \delta R_{xx} + \frac{\partial g}{\partial R_{xxx}}\Big|^{m,k} \delta R_{xxx} \right) \\
&+ \left(\frac{\partial g}{\partial w}\Big|^{m,k} \delta w + \frac{\partial g}{\partial w_x}\Big|^{m,k} \delta w_x + \frac{\partial g}{\partial w_{xx}}\Big|^{m,k} \delta w_{xx} \right).
\end{aligned} \tag{C.20}$$

The spatial derivatives of R and w in F and δF are determined by recurrence relations applied to Chebyshev coefficients (discussed in chapter III). These recurrence relations are easily found in references such as Shen *et al.* (2011). The terms $\delta R_x, \delta R_{xx}, \delta R_{xxx}, \delta w_x$ and δw_{xx} may be rewritten with δR and δw with Chebyshev differentiation matrices (Trefethen 2000). Please note these differentiation matrices are different from the recurrence relations. For example, D^1, D^2, and D^3 are the Chebyshev differentiation matrices to determine the 1st, 2nd, and 3rd derivatives, respectively. The terms $\delta R_x, \delta R_{xx}$, and δR_{xxx} are re-expressed as D^1, D^2, and D^3 operating on δR or δw.

Dirchlet boundary conditions are imposed by replacing the rows corresponding to the boundary nodes (0-th, (N-1)-th, N-th and $(2N-1)$-th rows) in R and w in δF

with an array of zeros and then placing a 1 in the following (row, column) of δF: (0,0), ($N-1$, $N-1$), (N, N), and ($2N-1$, $2N-1$). The 0-th, N-1-th, N-th and $(2N-1)$-th elements in F must be replaced with zeros.

Neumann boundary conditions for R are applied by replacing the rows corresponding to the boundary nodes (0-th, (N-1)-th rows) in δF with an array of zeros. Then, the first row of the Chebyshev differentiation matrices D^1 is placed in the 0-th row (and 0 - $N-1$ columns) of δF. Similarly, the last row of D^1 is placed in the $(N-1)$-th row (and 0 - $N-1$ columns) of δF. The 0-th and N-1-th elements in F must also be replaced with zeros.

After applying the boundary conditions, the system $\delta F = -F$ is solved iteratively until $|\delta x|$ is less than some convergence criteria, typically 10^{-6}.

BIBLIOGRAPHY

BIBLIOGRAPHY

2011 Blow the Best Bubbles.

Agee, S. 2014 Bubble-ology.

Akkas, E. A., Yucel, B., Kilickap, S. & Altuntas, E. E. 2013 Evaluation of Quality of Life in Turkish Patients with Head and Neck Cancer. *Asian Pacific Journal of Cancer Prevention* **14** (8), 4805–4809.

Ambravaneswaran, B. & Basaran, O. A. 1999 Effects of insoluble surfactants on the nonlinear deformation and breakup of stretching liquid bridges. *Physics of Fluids* **11** (5), 997.

Anna, S. L. & McKinley, G. H. 2001 Elasto-capillary thinning and breakup of model elastic liquids. *Journal of Rheology* **45** (1), 115–138.

Ardekani, A. M., Sharma, V. & McKinley, G. H. 2010 Dynamics of bead formation, filament thinning and breakup in weakly viscoelastic jets. *Journal of Fluid Mechanics* **665**, 46–56.

Bazilevsky, A. V., Entov, V. M. & Rozhkov, A. N. 1990 Liquid filament microrheometer and some of its applications. In *Third European Rheology Conference and Golden Jubilee Meeting of the British Society of Rheology*, pp. 41–43. Netherlands: Springer.

Bazilevsky, A. V., Entov, V. M. & Rozhkov, A. N. 2011 Breakup of a liquid bridge as a method of rheological testing of biological fluids. *Fluid Dynamics* **46** (4), 613–622.

Bechtel, S. E., Forest, M. G., Holm, D. D. & Lin, K. J. 1988 One-dimensional closure models for three-dimensional incompressible viscoelastic free jets: von Kármán flow geometry and elliptical cross-section. *Journal of Fluid Mechanics* **196** (-1), 241.

Bejenariu, A. G., Rasmussen, H. K., Skov, A. L., Hassager, O. & Frankaer, S. M. 2010 Large amplitude oscillatory extension of soft polymeric networks. *Rheologica Acta* **49** (8), 807–814.

Bhat, P. P., Appathurai, S., Harris, M. T., Pasquali, M., McKinley, G. H. & Basaran, O. A. 2010 Formation of beads-on-a-string structures during break-up of viscoelastic filaments. *Nature Physics* **6** (8), 625–631.

Bird, R., Armstrong, R. & Hassager, O. 1987*a* *Dynamics of Polymeric Liquids, Volume 1: Fluid Mechanics*. New York: Wiley.

Bird, R., Armstrong, R. & Hassager, O. 1987*b* *Dynamics of Polymeric Liquids, Volume 2: Kinetic Theory*. New York: Wiley.

Bongaerts, J. H. H., Rossetti, D. & Stokes, J. R. 2007 The Lubricating Properties of Human Whole Saliva. *Tribology Letters* **27** (3), 277–287.

Bousfield, D., Keunings, R., Marrucci, G. & Denn, M. 1986 Nonlinear analysis of the surface tension driven breakup of viscoelastic filaments. *Journal of Non-Newtonian Fluid Mechanics* **21** (1), 79–97.

Boyd, J. 2001 *Chebyshev and Fourier spectral methods*, 2nd edn. New York: Dover Publications.

Brasseur, J. G. 1987 A fluid mechanical perspective on esophageal bolus transport. *Dysphagia* **2** (1), 32–39.

Brenner, M. P., Lister, J. R. & Stone, H. A. 1996 Pinching threads, singularities and the number 0.0304... *Physics of Fluids* **8** (11), 2827–2836.

de Bruijne, D., Hendrickx, H., Anderliesten, L. & de Looff, J. 1993 Mouthfeel of foods. In *Food colloids Society, polymers: stability and mechanical properties* (ed. E Dickinson & P Walstra), pp. 204–13. Sawston: Woodhead Publishing Limited.

Canny, J. 1986 A computational approach to edge detection. *IEEE Transactions on Pattern Analysis and Machine Intelligence* **PAMI-8** (6), 679–698.

Carpenter, G. 2012 Role of Saliva in the Oral Processing of Food. In *Food Oral Processing: Fundamentals of Eating and Sensory Perception* (ed. Jianshe Chen & Lina Engelen), pp. 45–60. Oxford, UK: Wiley-Blackwell.

Carpenter, G. H. 2013 The Secretion, Components, and Properties of Saliva. *Annual Review of Food Science and Technology* **4** (1), 267–276.

Chandrasekhar, S. 1961 *Hydrodynamic And Hydromagnetic Stability*. Oxford: Clarendon Press.

Christersson, C. E., Lindh, L. & Arnebrant, T. 2000 Film-forming properties and viscosities of saliva substitutes and human whole saliva. *European Journal of Oral Sciences* **108** (5), 418–425.

Clasen, C., Eggers, J., Fontelos, M. A., Li, J. & McKinley, G. H. 2006*a* The beads-on-string structure of viscoelastic threads. *Journal of Fluid Mechanics* **556**, 283, arXiv: 0307611.

Clasen, C., Plog, J. P., Kulicke, W.-M., Owens, M., Macosko, C., Scriven, L. E., Verani, M. & McKinley, G. H. 2006*b* How dilute are dilute solutions in extensional flows? *Journal of Rheology* **50** (6), 849.

Craster, R. V., Matar, O. K. & Papageorgiou, D. T. 2002 Pinchoff and satellite formation in surfactant covered viscous threads. *Physics of Fluids* **14** (4), 1364.

Donea, J., Giuliani, S. & Halleux, J. 1982 An arbitrary lagrangian-eulerian finite element method for transient dynamic fluid-structure interactions. *Computer Methods in Applied Mechanics and Engineering* **33** (1-3), 689–723.

Eggers, J. 1993 Universal pinching of 3D axisymmetric free-surface flow. *Physical review letters* **71** (21), 3458–3460.

Eggers, J. 1997 Nonlinear dynamics and breakup of free-surface flows. *Reviews of Modern Physics* **69** (3), 865–930.

Eggers, J. & Dupont, T. F. 1994 Drop formation in a one-dimensional approximation of the NavierStokes equation. *Journal of Fluid Mechanics* **262** (-1), 205.

Entov, V. & Hinch, E. 1997 Effect of a spectrum of relaxation times on the capillary thinning of a filament of elastic liquid. *Journal of Non-Newtonian Fluid Mechanics* **72** (1), 31–53.

Foglio-Bonda, A., Pattarino, F. & Foglio-Bonda, P. L. 2014 Kinematic viscosity of unstimulated whole saliva in healthy young adults. *European Review for Medical and Pharmacological Sciences* **18** (20), 2988–2994.

Fontelos, M. A. & Li, J. 2004 On the evolution and rupture of filaments in Giesekus and FENE models. *Journal of Non-Newtonian Fluid Mechanics* **118** (1), 1–16.

Galindo-Rosales, F. J., Alves, M. A. & Oliveira, M. S. N. 2013 Microdevices for extensional rheometry of low viscosity elastic liquids: a review. *Microfluidics and Nanofluidics* **14** (1-2), 1–19.

Garcia, C. J., Castro-Combs, J., Dias, A., Alfaro, R., Vasallo, J., Majewski, M., Jaworski, T., Wallner, G. & Sarosiek, J. 2013 Impairment of salivary mucin production resulting in declined salivary viscosity during naproxen administration as a potential link to upper alimentary tract mucosal injury. *Clinical and translational gastroenterology* **4**, e40.

Gennes, P. & Brochard-Wyart, F. 2004 *Capillarity and Wetting Phenomena: Drops, Bubbles, Pearls, Waves*. New York: Springer.

Haward, S. J., Odell, J. a., Berry, M. & Hall, T. 2011 Extensional rheology of human saliva. *Rheologica Acta* **50** (11-12), 869–879.

Herrchen, M. & Öttinger, H. C. 1997 A detailed comparison of various FENE dumbbell models. *Journal of Non-Newtonian Fluid Mechanics* **68** (1), 17–42.

Humphrey, S. P. & Williamson, R. T. 2001 A review of saliva: normal composition, flow, and function. *The Journal of prosthetic dentistry* **85** (2), 162–9.

Isenberg, C. 1978 *The Science of Soap Films and Soap Bubbles*. Clevedon: Tieto Ltd.

Kaplan, M. D. & Baum, B. J. 1993 The functions of saliva. *Dysphagia* **8** (3), 225–229.

Kazakov, V. N., Udod, A. A., Zinkovych, I. I., Fainerman, V. B. & Miller, R. 2009 Dynamic surface tension of saliva: general relationships and application in medical diagnostics. *Colloids and surfaces. B, Biointerfaces* **74** (2), 457–61.

Keunings, R. 1997 On the Peterlin approximation for finitely extensible dumbbells. *Journal of Non-Newtonian Fluid Mechanics* **68** (1), 85–100.

Kolte, M. I. & Szabo, P. 1999 Capillary thinning of polymeric filaments. *Journal of Rheology (1978-present)* **43** (3), 609–625.

Langmore, S. E., Terpenning, M. S., Schork, A., Chen, Y., Murray, J. T., Lopatin, D. & Loesche, W. J. 1998 Predictors of Aspiration Pneumonia: How Important Is Dysphagia? *Dysphagia* **13** (2), 69–81.

Larson, R. 1988 *Constitutive Equations for Polymer Melts and Solutions*. Boston: Butterworth-Heinemann.

Levine, M. J., Aguirre, A., Hatton, M. N. & Tabak, L. A. 1987 Artificial salivas: present and future. *Journal of dental research* **66 Spec No**, 693–8.

Liang, R. & Mackley, M. 1994 Rheological characterization of the time and strain dependence for polyisobutylene solutions. *Journal of Non-Newtonian Fluid Mechanics* **52** (3), 387–405.

Liao, Y.-C., Franses, E. I. & Basaran, O. A. 2006 Deformation and breakup of a stretching liquid bridge covered with an insoluble surfactant monolayer. *Physics of Fluids* **18** (2), 022101.

Lima, D. P., Diniz, D. G., Moimaz, S. A. S., Sumida, D. H. & Okamoto, A. C. 2010 Saliva: reflection of the body. *International Journal of Infectious Diseases* **14** (3), 184–188.

Liu, J. & Duan, Y. 2012 Saliva: A potential media for disease diagnostics and monitoring. *Oral Oncology* **48** (7), 569–577.

Matta, J. & Tytus, R. 1990 Liquid stretching using a falling cylinder. *Journal of Non-Newtonian Fluid Mechanics* **35** (2-3), 215–229.

McCarroll, L. L., Solomon, M. J. & Schultz, W. W. 2016 Differential analysis of capillary breakup rheometry for Newtonian liquids. *Journal of Fluid Mechanics* **804**, 116–129.

McKinley, G. H. 2005 Visco-Elasto-Capillary Thinning and Break-Up of Complex Fluids. In *Annual Rheology Reviews* (ed. DM Binding & K Walter), pp. 1–48. Aberystwyth: British Society of Rheology.

McKinley, G. H. & Sridhar, T. 2002 Filament stretching rheometry of complex fluids. *Annual Review of Fluid Mechanics* **34** (1), 375–415.

McKinley, G. H. & Tripathi, A. 2000 How to extract the Newtonian viscosity from capillary breakup measurements in a filament rheometer. *Journal of Rheology (1978-present)* **44** (3), 653–670.

Mittal, B. B., Wang, E., Sejpal, S., Agulnik, M., Mittal, A. & Harris, K. 2013 Effect of recombinant human deoxyribonuclease on oropharyngeal secretions in patients with head-and-neck cancers treated with radiochemotherapy. *International journal of radiation oncology, biology, physics* **87** (2), 282–9.

Ogama, N. & Ogama, N. 2013 Development of an oral assessment tool to evaluate appetite in patients with head and neck cancer receiving radiotherapy. *European journal of oncology nursing : the official journal of European Oncology Nursing Society* **17** (4), 474–81.

Oliveira, M. S., Yeh, R. & McKinley, G. H. 2006 Iterated stretching, extensional rheology and formation of beads-on-a-string structures in polymer solutions. *Journal of Non-Newtonian Fluid Mechanics* **137** (1-3), 137–148.

Oliveira, M. S. N. & McKinley, G. H. 2005 Iterated stretching and multiple beads-on-a-string phenomena in dilute solutions of highly extensible flexible polymers. *Physics of Fluids* **17** (7), 071704.

Oliveira, P. 2009 Alternative derivation of differential constitutive equations of the Oldroyd-B type. *Journal of Non-Newtonian Fluid Mechanics* **160** (1), 40–46.

Padday, J. F., Pitt, A. R. & Pashley, R. M. 1975 Menisci at a free liquid surface: surface tension from the maximum pull on a rod. *Journal of the Chemical Society, Faraday Transactions 1: Physical Chemistry in Condensed Phases* **71**, 1919–1931.

Papageorgiou, D. T. 1995 On the breakup of viscous liquid threads. *Physics of Fluids* **7** (7), 1529–1544.

Petrie, C. 1979 *Elongational Flows: Aspects of the Behaviour of Model Elastoviscous Fluids (Research notes in mathematics)*. London: Pitman.

Plateau, J. 1863 Experimental and Theoretical Researches on the Figures of Equilibrium of a Liquid Mass Withdrawn from the Action of Gravity. *Annual Report Smithsonian Institution Smithsonian Institution* pp. 207–285.

Preetha, A. & Banerjee, R. 2005 Comparison of artificial saliva substitutes. *Trends in Biomaterials and Artificial Organs* **18** (2), 178–186.

Proctor, G. B., Hamdan, S., Carpenter, G. H. & Wilde, P. 2005 A statherin and calcium enriched layer at the air interface of human parotid saliva. *Biochemical Journal* **389** (1), 111–116.

Rayleigh, L. 1879 On the Capillary Phenomena of Jets. *Proceedings of the Royal Society of London* **29** (196-199), 71–97.

van der Reijden, W. A., Veerman, E. C. & Amerongen, A. V. 1993 Shear rate dependent viscoelastic behavior of human glandular salivas. *Biorheology* **30** (2), 141–52.

Renardy, M. 1994 Some comments on the surface-tension driven break-up (or the lack of it) of viscoelastic jets. *Journal of Non-Newtonian Fluid Mechanics* **51** (1), 97–107.

Rodd, L., Scott, T., Cooper-White, J. & McKinley, G. 2005 Capillary break-up rheometry of low-viscosity elastic fluids. *Applied Rheology* **15** (1), 12–27.

Rosen, M. & Kunjappu, J. 2012 *Surfactants and Interfacial Phenomena*, 4th edn. Hoboken: John Wiley & Sons.

Sarkar, A., Goh, K. K. & Singh, H. 2009 Colloidal stability and interactions of milk-protein-stabilized emulsions in an artificial saliva. *Food Hydrocolloids* **23** (5), 1270–1278.

Schipper, R. G., Silletti, E. & Vingerhoeds, M. H. 2007 Saliva as research material: biochemical, physicochemical and practical aspects. *Archives of oral biology* **52** (12), 1114–35.

Schultz, W. W. 1987 Slender Viscoelastic Fiber Flow. *Journal of Rheology* **31** (8), 733.

Schultz, W. W. & Davis, S. 1982 One-Dimensional Liquid Fibers. *Journal of Rheology* **26** (4), 331–345.

Schwarz, W. H. 1987 The rheology of saliva. *J Dent Res* **66 Spec No**, 660–666.

Shen, J., Tang, T. & Wang, L.-L. 2011 *Spectral Methods*, *Springer Series in Computational Mathematics*, vol. 41. Berlin, Heidelberg: Springer Berlin Heidelberg.

Smith, C. H., Boland, B., Daureeawoo, Y., Donaldson, E., Small, K. & Tuomainen, J. 2013 Effect of aging on stimulated salivary flow in adults. *Journal of the American Geriatrics Society* **61** (5), 805–8.

Spiegelberg, S. H., Ables, D. C. & McKinley, G. H. 1996 The role of end-effects on measurements of extensional viscosity in filament stretching rheometers. *Journal of Non-Newtonian Fluid Mechanics* **64** (2-3), 229–267.

Stelter, M., Brenn, G., Yarin, A. L., Singh, R. P. & Durst, F. 2000 Validation and application of a novel elongational device for polymer solutions. *Journal of Rheology* **44** (3), 595.

Stokes, J. R. & Davies, G. A. 2007 Viscoelasticity of human whole saliva collected after acid and mechanical stimulation. *Biorheology* **44** (3), 141–60.

Tembely, M., Vadillo, D., Mackley, M. R. & Soucemarianadin, A. 2012 The matching of a one-dimensional numerical simulation and experiment results for low viscosity Newtonian and non-Newtonian fluids during fast filament stretching and subsequent break-up. *Journal of Rheology* **56** (1), 159.

Terpenning, M. S., Taylor, G. W., Lopatin, D. E., Kerr, C. K., Dominguez, B. L. & Loesche, W. J. 2001 Aspiration Pneumonia: Dental and Oral Risk Factors in an Older Veteran Population. *Journal of the American Geriatrics Society* **49** (5), 557–563.

Timmermans, M.-L. E. & Lister, J. R. 2002 The effect of surfactant on the stability of a liquid thread. *Journal of Fluid Mechanics* **459**, 289–306.

Tirtaatmadja, V. & Sridhar, T. 1993 A filament stretching device for measurement of extensional viscosity. *Journal of Rheology (1978-present)* **37** (6), 1081–1102.

Trefethen, L. N. 2000 *Spectral Methods in MATLAB*. Philadelphia: Society for Industrial and Applied Mathematics.

Turcanu, M., Tascon, L. F., Balan, C. & Gallegos, C. 2015 Capillary breakup extensional properties of whole human saliva. In *2015 9th International Symposium on Advanced Topics in Electrical Engineering (ATEE)*, pp. 269–274. IEEE.

Vadillo, D. C., Tembely, M., Morrison, N. F., Harlen, O. G., Mackley, M. R. & Soucemarianadin, A. 2012 The matching of polymer solution fast filament stretching, relaxation, and break up experimental results with 1D and 2D numerical viscoelastic simulation. *Journal of Rheology* **56** (6), 1491–1516.

Van Tornout, M., Dadamio, J., Coucke, W. & Quirynen, M. 2013 Tongue coating: related factors. *Journal of clinical periodontology* **40** (2), 180–5.

Wagner, C., Amarouchene, Y., Bonn, D. & Eggers, J. 2005 Droplet Detachment and Satellite Bead Formation in Viscoelastic Fluids. *Physical Review Letters* **95** (16), 164504.

Wagner, C., Bourouiba, L. & McKinley, G. H. 2015 An analytic solution for capillary thinning and breakup of FENE-P fluids. *Journal of Non-Newtonian Fluid Mechanics* **218**, 53–61.

Wagner, C. C. E. 2015 An experimental and theoretical investigation of the rheological properties and degradation of mucin solutions: (or why saliva becomes watery when removed from your mouth). PhD thesis, MIT.

Yao, M. & McKinley, G. H. 1998 Numerical simulation of extensional deformations of viscoelastic liquid bridges in filament stretching devices. *Journal of Non-Newtonian Fluid Mechanics* **74** (1-3), 47–88.

Yao, M., McKinley, G. H. & Debbaut, B. 1998 Extensional deformation, stress relaxation and necking failure of viscoelastic filaments. *Journal of Non-Newtonian Fluid Mechanics* **79** (2-3), 469–501.

Yildirim, O. E. & Basaran, O. A. 2001 Deformation and breakup of stretching bridges of Newtonian and shear-thinning liquids: Comparison of one- and two-dimensional models. *Chemical Engineering Science* **56** (1), 211–233.

Zhou, Y. & Schroeder, C. M. 2016 Single polymer dynamics under large amplitude oscillatory extension. *Physical Review Fluids* **1** (5), 053301.

Zussman, E., Yarin, A. & Nagler, R. 2007 Age- and flow-dependency of salivary viscoelasticity. *Journal of Dental Research* **86** (3), 281–285.